LA-8648-T

Thesis

Small Angle Proton-Proton and Proton-Deuteron Elastic Scattering at 800 MeV

University of California

DISTRIBUTION OF THIS DOCUMENT IS UNLIMITED

LOS ALAMOS SCIENTIFIC LABORATORY
Post Office Box 1663 Los Alamos, New Mexico 87545

This thesis was accepted by the University of California, Los Angeles, in partial fulfillment of the requirements for the degree of Doctor of Philosophy in Physics. It is the independent work of the author and has not been edited by the Technical Information staff.

This work was supported by the US Department of Energy, Division of Intermediate Energy Nuclear Physics, Contract No. DE-AM03-76SF 00010, Project Agreement 24.

UNITED STATES
DEPARTMENT OF ENERGY
CONTRACT W-7405-ENG. 36

Printed in the United States of America
Available from
National Technical Information Service
US Department of Commerce
5285 Port Royal Road
Springfield, VA 22161

Microfiche $3.50 (A01)

Page Range	Domestic Price	NTIS Price Code	Page Range	Domestic Price	NTIS Price Code	Page Range	Domestic Price	NTIS Price Code	Page Range	Domestic Price	NTIS Price Code
001-025	$ 5.00	A02	151-175	$11.00	A08	301-325	$17.00	A14	451-475	$23.00	A20
026-050	6.00	A03	176-200	12.00	A09	326-350	18.00	A15	476-500	24.00	A21
051-075	7.00	A04	201-225	13.00	A10	351-375	19.00	A16	501-525	25.00	A22
076-100	8.00	A05	226-250	14.00	A11	376-400	20.00	A17	526-550	26.00	A23
101-125	9.00	A06	251-275	15.00	A12	401-425	21.00	A18	551-575	27.00	A24
126-150	10.00	A07	276-300	16.00	A13	426-450	22.00	A19	576-600	28.00	A25
									601-up	†	A99

†Add $1.00 for each additional 25-page increment or portion thereof from 601 pages up.

LA-8648-T
Thesis

UC-34c
Issued: January 1981

Small Angle Proton-Proton and Proton-Deuteron Elastic Scattering at 800 MeV

Farokh Irom*

*University of California, Physics Department, Los Angeles, CA 90024.

TABLE OF CONTENTS

LIST OF TABLES

LIST OF FIGURES

Small Angle Proton-Proton and Proton-Deuteron Elastic Scattering at 800 Mev

by

Farokh Irom

ABSTRACT

By measuring the energy of recoil particles, the following data have been obtained at 800 MeV incident proton energy; (1) the differential cross section for elastic proton-proton scattering at laboratory angles ranging between 1.34° and 6.45°, (2) the analyzing power for elastic proton-proton scattering at laboratory angles ranging between 2.8° and 6.45°, and (3) the differential cross sections and analyzing powers for elastic proton-deuteron scattering at laboratory angles ranging between 3.97° and 13.1°. The data were analyzed to obtain information about the hadronic parts of the proton-proton and proton-neutron forward scattering amplitudes. The ratio ρ of the real to the imaginary parts of the forward p-p spin-independent amplitude was found to be 0.005 ± 0.04. The ratio R of the summed moduli squared of the forward p-p double-spin-flip scattering amplitude to the modulus squared of the forward p-p spin-independent amplitude was found to be 0.16 ± 0.03. The real and the imaginary parts of the p-p spin-orbit scattering amplitude divided by $\sin\theta$ were found to be 0.79 ± 0.05 fm and 0.18 ± 0.11 fm, respectively. Finally, the real and the imaginary parts of the p-n spin-orbit scattering amplitude divided by $\sin\theta$ were found to be 0.79 ± 0.09 fm and -1.6 ± 0.03 fm, respectively. These values were compared with the results of recent phase shift analyses and forward dispersion relation calculation.

INTRODUCTION

It has been clear experimentally that the forward angle differential cross section in proton-proton elastic scattering at energies in the GeV region is substantially larger than the theoretical minimum $(\frac{k}{4\pi}\sigma_{ToT})^2$ allowed by the optical theorem, where k is the center-of-mass wave number and σ_{ToT} is the total cross section. The optical theorem for proton-proton scattering may be written (Appendix A)

$$\frac{k}{4\pi}\sigma_{ToT} = \mathrm{Im}\alpha_N(0)$$

where $\alpha_N(0)$ denotes the spin-independent amplitude (complex). An excess of the forward differential cross section above the optical limit may arise because of the existence of a real part of the spin-independent amplitude or from spin dependent terms which are non-zero in the forward direction. In experiments at very small momentum transfer $10^{-3} < |t| < 10^{-2}$ (Gev/c)^2 the Coulomb scattering amplitude as well as its interference with nuclear scattering amplitude can be observed. In principle, by parameterizing the amplitudes appropriately, such measurements allow us to determine the magnitude and sign of the ratio, ρ, between the real and imaginary parts of the forward spin-independent nuclear amplitude as well as the magnitude of the contributions from spin-dependent amplitudes. Also, analyzing power measurements in the Coulomb-nuclear interference region can be used to determine additional information about the general nucleon-nucleon amplitude, in particular, information about the single-spin-flip or spin-orbit amplitude. In fact, at intermediate energies at the Coulomb-nuclear interference region very few analyzing power measurements are available. The predictions for analyzing power parameters at these small angles are essentially extrapolations from measurements at larger angles by means of phase shift analyses (Arndt 74), (Bystricky 75) and have never been adequately tested. Thus small angle measurements of differential cross sections and analyzing powers can be used to obtain direct information on the nuclear interaction by taking advantage of the electromagnetic-nuclear interference.

The experiments described in this dissertation were performed at LAMPF, during the Summer of 1979 using the External Proton Beam (EPB) Line. Recoil particles were observed after their scattering from a target gas (hydrogen or deuterium) in a scattering chamber by using solid state detector telescopes. In this work, data on the differential cross sections, $d\sigma/dt$, for elastic proton-proton scattering in the range of the four momentum transfer squared $0.001 < |t| < 0.03$ $(\mathrm{GeV/c})^2$, and on the analyzing powers, $A_y(\theta)$, for elastic proton-proton scattering in the range $0.005 < |t| < 0.03$ $(\mathrm{GeV/c})^2$ were collected. Also, with the same experimental apparatus differential cross sections and analyzing powers were measured for elastic proton-deuteron scattering in the range $0.01 < |t| < 0.11$ $(\mathrm{GeV/c})^2$.

By parameterization of the p-d differential cross section and analyzing power data, we can extract information on the proton-neutron amplitude as well as on the proton-proton amplitude.

The experiment described in this work provided high quality data on forward angle proton-proton and proton-deuteron elastic scattering at 800 MeV. In summary, from the analysis of the p-p data we determined:

1. The sign and magnitude for the ratio, ρ, between the real and the imaginary parts of nuclear spin-independent amplitude in the forward direction.
2. The ratio between the summed moduli squared of double-spin-flip amplitudes at zero degrees and the modulus squared of the spin-independent amplitude at zero degrees.
3. The real and the imaginary parts of the proton-proton nuclear spin-orbit amplitude.

From the analysis of the proton-deuteron data we extracted the real and imaginary parts of the p-n nuclear spin-orbit amplitude; and the effects of the spin-dependent nucleon-nucleon amplitudes and of the double scattering terms on the proton-deuteron cross sections and analyzing powers were also checked.

Theoretical concepts underlying the proton-proton and proton-deuteron analyses are discussed in Chapters I and II, respectively. Chapters III describes the experimental setup. In Chapter IV the experimental techniques are explained. The data reduction is discussed in Chapter V. In Chapter VI and Chapter VII we discuss the theoretical analyses for the proton-proton and proton-deuteron data, respectively.

CHAPTER I

THEORETICAL ASPECTS FOR PROTON-PROTON DATA

In this chapter a detailed exposition of the proton-proton elastic scattering is presented, reviewing known results. We will discuss the nucleon-nucleon scattering matrix, M, and parameterize the proton-proton elastic differential cross section, $d\sigma/dt$, and analyzing power, $A_y(\theta)$.

A. Nucleon-Nucleon Scattering Matrix

A complete description for the scattering of two spin 1/2 particles is given by a 4 x 4 matrix:

$$M(\vec{\sigma}_1, \vec{\sigma}_2, \vec{K}_i, \vec{K}_f) \tag{1-1}$$

where $\vec{K}_i$ and $\vec{K}_f$ are the momenta of the incident and scattered particles in center-of-mass and $\vec{\sigma}_1$ and $\vec{\sigma}_2$ are the Pauli spin operators acting on the first and second nucleon wave functions, respectively (i.e., $\vec{\sigma}_1$ for the incident and scattered nucleon and $\vec{\sigma}_2$ for target and recoil nucleon). The most general form of this matrix may be found by following a procedure similar to that used to find the most general form of the interaction Hamiltonian for two particles of spin 1/2 (Eisenbud 41). Conditions placed on the matrix M are invariance under space rotations and reflections and time reversal.

Taking into account these conditions, the nucleon-nucleon elastic scattering matrix has the following general form (Goldberger 64)

$$M = \alpha + i\gamma(\vec{\sigma}_1 + \vec{\sigma}_2) \cdot \hat{n} + \beta(\vec{\sigma}_1 \cdot \hat{n})(\vec{\sigma}_2 \cdot \hat{n}) + \delta(\vec{\sigma}_1 \cdot \hat{m})(\vec{\sigma}_2 \cdot \hat{m})$$
$$+ \varepsilon(\vec{\sigma}_1 \cdot \hat{\ell})\,(\vec{\sigma}_2 \cdot \hat{\ell}) + i\eta(\vec{\sigma}_1 \cdot \hat{n} - \vec{\sigma}_2 \cdot \hat{n}) \quad . \qquad (1\text{-}2)$$

Here the amplitudes α, β, γ, δ, ε, and η are complex functions of two variables the center-of-mass energy $\sqrt{s}$ and the scattering angle θ, or equivalently the momentum transfer $q^2\left(q^2 = 2p_{cm}^2(1-\cos\theta_{cm})\right)$. α is the spin-independent (central) amplitude; γ and η are the spin-orbit amplitudes; and β, δ, and ε are the double spin flip amplitudes. The center-of-mass system unit vectors are:

$$\hat{\ell} = \frac{\vec{k}_i + \vec{K}_f}{|\vec{K}_i + \vec{K}_f|} \; ,$$

$$\hat{m} = \frac{\vec{K}_f - \vec{K}_i}{|\vec{K}_f - \vec{K}_i|} \; , \qquad (1\text{-}3)$$

$$\hat{n} = \frac{\vec{K}_i \times \vec{K}_f}{|\vec{K}_i \times \vec{K}_f|} \; ,$$

which form an orthogonal Cartesian co-ordinate system. In non relativistic kinematics, they have a very convenient meaning in the laboratory system, since $\hat{\ell}$ represents the direction of motion of the scattered nucleon, $\hat{n}$ is the direction perpendicular to the scattering plane, and (minus)$\hat{m}$ is the direction of motion of the recoil nucleon.

For proton-proton and neutron-neutron scattering in which the two particles are identical the sixth term in scattering matrix, η, is zero; and this is also true for neutron-proton scattering if charge independence is assumed.

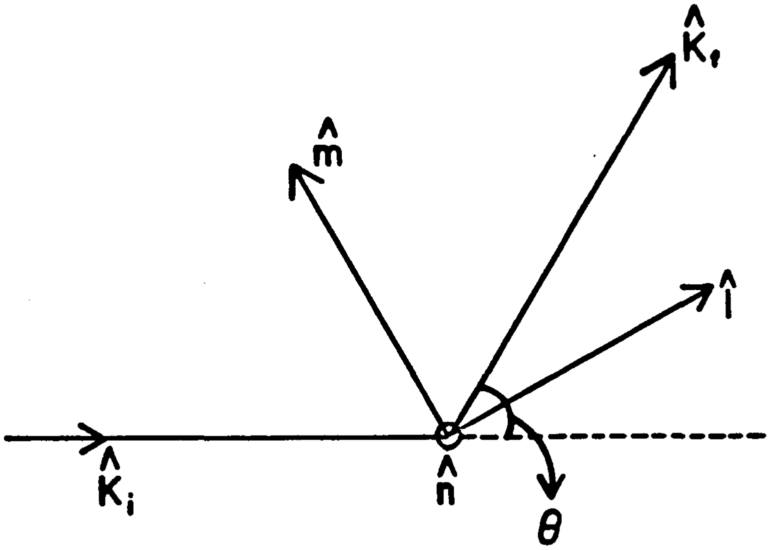

Fig. (1-1): The orthogonal unit vectors $\hat{\ell}$, $\hat{m}$, $\hat{n}$ in c.m.f.
$\hat{n}$ is an arrow out of the page.

B. The Density Matrix Formalism

In a scattering experiment one prepares the two particles in certain states prior to scattering and subsequently measures the state of the particles after scattering. These processes can be conveniently formulated in terms of the density matrix rather than wave functions. An arbitrary spin state $|\chi_n\rangle$ in a system of two particles with spin s_1 and s_2 is a linear combination of the $(2s_1 + 1)(2s_2 + 1)$ basic states of the composite system and may be represented by a vector with $(2s_1 + 1)(2s_2 + 1)$ components. For example, if $s_1 = s_2 = 1/2$, the four basic states could be the three triplet and one singlet states. For a given pure spin state $|\chi_n\rangle$, the density matrix is defined as:

$$\rho = |\chi_n\rangle\langle\chi_n| \tag{1-4}$$

which is clearly a projection operator. In practice we deal with an incoherent mixture of pure spin states, as in the case of a nucleon beam from an accelerator. The density matrix is then defined as

$$\rho = \sum_n |\chi_n\rangle P_n \langle\chi_n| \tag{1-5}$$

where P_n is the relative probability of finding the system in state χ_n. For a beam of particles, the sum may be considered as a sum over the states of the individual particles in the beam.

Any observable is represented by some Hermitian operator Q. The expectation value of Q in the mixed state is given by

$$\begin{aligned} \langle Q\rangle &= \sum_{n} P_n \langle \chi_n | Q | \chi_n\rangle \\ &= \sum_{n,m} P_n \langle \chi_n | Q | m\rangle\langle m | \chi_n\rangle \\ &= \sum_{m} \langle m | Q\rho | m\rangle \end{aligned}$$

or

$$\langle Q\rangle = \mathrm{Tr}(Q\rho) \quad . \tag{1-6}$$

The density matrix defined above characterizes a system at a given time. As time proceeds the density matrix changes. In particular, the initial spin state of the system χ_n is associated with a definite scattering state, which, in terms of the scattering state wave functions has the asymptotic form

$$\psi \sim e^{i\vec{q}\cdot\vec{r}} \, |\chi_n\rangle + \sum_{m} F_{mn}(\theta,\phi) \frac{e^{iqr}}{r} |\chi_m\rangle \quad . \tag{1-7}$$

In other words, the initial spin state $|\chi_n\rangle$ is transformed into a certain final state

$$\sum_{m} F_{mn}(\Theta,\phi)|\chi_m\rangle \equiv M|\chi_n\rangle \tag{1-8}$$

where M is the spin-scattering matrix. For nucleon-nucleon system it is defined in Eq. (1-1). Thus we can construct the final density matrix

$$\rho_f = \sum_n M|\chi_n\rangle P_n\langle\chi_n|M^\dagger$$

$$= M\rho_i M^\dagger$$

or, in the normalized form ($\mathrm{Tr}\rho = 1$)

$$\rho_f = \frac{(M\rho_i M^\dagger)}{\mathrm{Tr}(M\rho_i M^\dagger)} \quad . \qquad (1\text{-}9)$$

The density ρ is Hermitian and for the nucleon-nucleon system it can be expanded in terms of 16 independent matrices $\sigma_\mu^{(1)}\ \sigma_\nu^{(2)}$ which satisfy the following orthogonality relations

$$\mathrm{Tr}\left(\sigma_\mu^{(1)}\ \sigma_\nu^{(2)}\ \sigma_\lambda^{(1)}\ \sigma_p^{(2)}\right) = 4\delta_{\mu\nu}\delta_{\nu p} \ . \qquad (1\text{-}10)$$

Thus, we may write

$$\rho = \sum_{\mu,\nu}^{3} a_{\mu,\nu}\ \sigma_\mu^{(1)}\sigma_\nu^{(2)} \quad . \qquad (1\text{-}11)$$

Here, σ_o, σ_1, σ_2 and σ_3 are the unit matrix and Pauli spin matrices. We may write

$$\mathrm{Tr}\left(\sigma_{\mu'}^{(1)}\ \sigma_{\nu'}^{(2)}\ \ \rho\right) = \sum_{\mu,\nu} a_{\mu,\nu}\mathrm{Tr}\left(\sigma_{\mu'}^{(1)}\ \sigma_{\nu'}^{(2)}\ \sigma_\mu^{(1)}\ \sigma_\nu^{(2)}\right) \quad ,$$

using the orthogonality relations [Eq. (1-6) and Eq. (1-10)] one obtains

$$\langle\sigma_\mu^{(1)}\ \sigma_\nu^{(2)}\rangle = 4a_{\mu,\nu}\quad , \tag{1-12}$$

or

$$\rho = \frac{1}{4}\sum_{\mu,\nu} \langle\sigma_\mu^{(1)}\ \sigma_\nu^{(2)}\rangle\ \sigma_\mu^{(1)}\ \sigma_\nu^{(2)}\quad . \tag{1-13}$$

In this form the spin density matrix is expressed directly in terms of the 16 expectation values $\langle\sigma_\mu^{(1)}\ \sigma_\nu^{(2)}\rangle$. Six of these, the quantities

$$\langle\sigma_i^{(1)}\sigma_o^{(2)}\rangle \equiv \langle\sigma_i^{(1)}\rangle \text{ and } \langle\sigma_o^{(1)}\sigma_j^{(2)}\rangle \equiv \langle\sigma_j^{(2)}\rangle$$

are the components of the polarization vectors for the first and second particles, respectively; and the expectation values $\langle\sigma_i^{(1)}\sigma_j^{(2)}\rangle = C_{ij}$ are nine parameters related to a correlation between spin expectation in two particles.

Let us now proceed to calculate the differential cross section I_o for scattering of the incident particles described by the density matrix ρ_o, where the definition of this cross section involves a sum over the spin states of the final particles.

The differential cross section for scattering from any of the pure states χ_n is given by

$$I = \sum_m |M_{mn}|^2$$

$$= \sum_m M^\dagger_{nm} M_{mn}$$

$$= \langle \chi_n | M^\dagger M | \chi_n \rangle \qquad (1\text{-}14)$$

which is indeed the expectation value of the operator $M^\dagger M$ in the state χ_n. Thus, by Eq. (1-6) for a incoherent mixture of pure states with a density matrix ρ_i, the differential cross section may be written as:

$$I = \langle M^\dagger M \rangle = \mathrm{Tr}(M^\dagger M \rho_i) = \mathrm{Tr}(M \rho_i M^\dagger) \quad . \qquad (1\text{-}15)$$

The initial polarization state is completely specified by the expectation value $\langle \sigma_\mu^{(1)} \sigma_\nu^{(2)} \rangle_i$. By substituting Eq. (1-9) into Eq. (1-6), we get a basic relation between incident and final polarization states (MacGregor 60).

$$\langle \sigma_\mu^{(1)} \sigma_\nu^{(2)} \rangle_f = \mathrm{Tr}\left(\rho_f \sigma_\mu^{(1)} \sigma_\nu^{(2)}\right)$$

$$= \frac{\mathrm{Tr}\left(M \rho_i M^\dagger \sigma_\mu^{(1)} \sigma_\nu^{(2)}\right)}{\mathrm{Tr}(M \rho_i M^\dagger)}$$

substituting for ρ_i from Eq. (1-13) and using Eq. (1-15) one then obtains

$$I\langle\sigma^{(1)}_{\mu}\ \sigma^{(2)}_{\nu}\ \rangle_f =$$

$$\frac{1}{4}\ \sum_{\mu',\nu'}\ \langle\sigma^{(1)}_{\mu'}\sigma^{(2)}_{\nu'}\ \rangle_i\ \mathrm{Tr}\left(M\sigma^{(1)}_{\mu'}\sigma^{(2)}_{\nu'}\ M\ \sigma^{(1)}_{\mu}\sigma^{(2)}_{\nu}\right)\ . \qquad (1\text{-}16)$$

Let us now consider the scattering of an unpolarized beam on an unpolarized target. Then all the $\langle\sigma^{(1)}_{\mu}\ \sigma^{(2)}_{\nu}\rangle_i$'s are equal to zero in Eq. (1-13) except for $\langle\sigma^{(1)}_{o}\sigma^{(2)}_{o}\rangle_i = 1$, and hence the differential cross section for the scattering of a unpolarized beam on a unpolarized target is given by

$$I_o = \frac{1}{4}\left(MM^{\dagger}\right)\ . \qquad (1\text{-}17)$$

The polarization vector of the scattered particle (1) is obtained by using (1-16)

$$I_o\langle\sigma^{(1)}_{\mu}\sigma^{(2)}_{o}\rangle_f = I_o\langle\sigma^{(1)}_{\mu}\rangle_f$$

$$= \frac{1}{4}\ \mathrm{Tr}\left(MM^{\dagger}\sigma^{(1)}_{\mu}\sigma^{(2)}_{o}\right) \qquad (1\text{-}18)$$

where $\langle\sigma^{(1)}_{\mu}\rangle_f$ is the polarization of the particles (1) produced in the scattering of an unpolarized beam on an unpolarized target. Its direction is along the normal to the scattering plane (Hoshizaki 68).

$$\langle\vec{\sigma}^{(1)}\rangle_f = P\hat{n}$$

and

$$I_o P = \frac{1}{4} \mathrm{Tr}\left(MM^\dagger \sigma_n^{(1)} \sigma_o^{(2)}\right) \qquad (1\text{-}19)$$

where $\sigma_n^{(1)}$ is the normal component of $\sigma^{(1)}$.

Let us now consider the scattering of a polarized beam on a unpolarized target. Using Eq. (1-13) one obtains

$$\rho_i = \frac{1}{4} \hat{1} + \frac{1}{4} \sum_{\mu=1}^{3} \langle\sigma_\mu^{(1)}\rangle_i \, \sigma_\mu^{(1)} \sigma_o^{(2)}. \qquad (1\text{-}20)$$

We can define the polarization of the beam as $\vec{P}_B = P_{B\mu} \hat{\mu} = \sum_{\mu=1}^{3} \langle\sigma_\mu^{(1)}\rangle_i \hat{\mu}$; and then the differential cross section I for this case given by:

$$I = \frac{1}{4} \mathrm{Tr}(MM^\dagger) + \frac{1}{4} \sum_{\mu=1}^{3} P_{B\mu} \mathrm{Tr}\left(M\sigma_\mu^{(1)} \sigma_o^{(2)} M^\dagger\right) \quad . \qquad (1\text{-}21)$$

The first term on the right-hand side is the differential cross section I_o for unpolarized beam-unpolarized target scattering, and the second is the contribution due to the initial polarization $\vec{P}_B$. On the basis of invariance under time reversal we have the relation (Hoshizaki 68), (Wolfenstein 52)

$$\mathrm{Tr}(M\sigma^{(1)} M^\dagger) = \mathrm{Tr}\,(MM^\dagger \sigma^{(1)}) \quad ; \qquad (1\text{-}22)$$

therefore Eq. (1-21) may be written in the form of

$$I = \frac{1}{4} \mathrm{Tr}\left[(1 + \vec{P}_B \cdot \vec{\sigma}^{(1)})MM^{\dagger}\right] \qquad (1\text{-}23)$$

using Eq. (1-19) one then obtains

$$I = I_o \, (1 + \vec{P}_B \cdot \hat{n}P) \quad . \qquad (1\text{-}24)$$

The quantitv $\varepsilon = \vec{P}_B \cdot \hat{n}P = P_B P\cos\phi$ (where ϕ is the angle between the initial polarization vector, $\vec{P}_B$, and the unit vector, $\hat{n}$, normal to scattering plane) is called the asymmetry of the scattering. Its magnitude varies with both P (the magnitude of the polarization induced in the scattering) and P_B (the magnitude of the incident polarization). If, in a scattering experiment with known P_B, the asymmetry amplitude

$$\varepsilon = PP_B \cos\phi$$

is determined then the analyzing power A of the scattering is defined to be

$$A = \frac{\varepsilon(\phi = 0)}{P_B} \quad .$$

For elastic scattering in the nucleon-nucleon system this reduces to

$$A = P \quad .$$

In order to measure the analyzing power A, we take the co-ordinate axes so that the initial polarization P_B is parallel to the z axis, and assume that the scattering plane is set in the x-y plane Fig. (1-2). If the incident particles are scattered left (right) with respect to their initial direction, the angle ϕ between P_B and $\hat{n}$ is $\phi = 0$ (π), and Eq. (1-24) becomes

$$Y_L \equiv I(\theta,0) = I_o(\theta)(1 + P_B P)$$

$$\qquad\qquad (1\text{-}25)$$

$$Y_R \equiv I(\theta,\pi) = I_o(\theta)(1 - P_B P)$$

or, one obtains

$$\frac{Y_L - Y_R}{Y_L + Y_R} = P_B P \quad .$$

Hence, the analyzing power A can be measured from the left-right asymmetry in the scattering process:

$$A = \frac{1}{P_B}\left[\frac{Y_L - Y_R}{Y_L + Y_R}\right] \quad . \qquad (1\text{-}26)$$

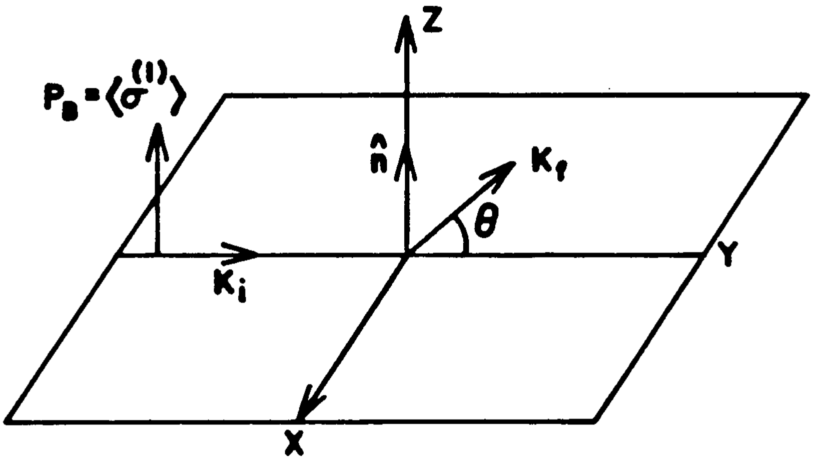

Scattering to the left

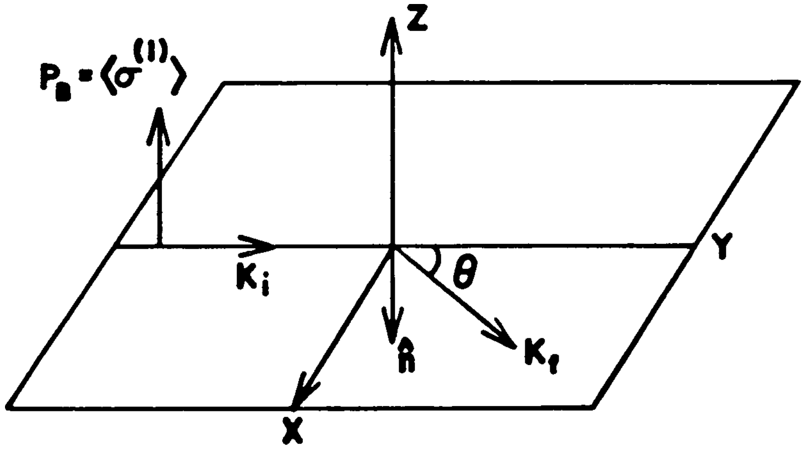

Scattering to the right

Fig. (1-2): The scattering of polarized nucleons with their spin along the z-axis.

C. Proton-Proton Elastic Scattering

In order to calculate the differential cross section for unpolarized beam-unpolarized target scattering in terms of the scattering amplitudes, α, β, γ, δ, and ε, we substitute for M from Eq. (1-2) into Eq. (1-17) obtaining:

$$I_o = |\alpha|^2 + |\beta|^2 + 2|\gamma|^2 + |\delta|^2 + |\varepsilon|^2 \quad . \tag{1-27}$$

In the case of polarized beam-unpolarized target scattering, using Eq. (1-21) one obtains:

$$I = I_o + 2\vec{P}_B \cdot \hat{n} \ \mathrm{Re}\left\{(\alpha + \beta)^* \ (i\gamma)\right\}$$

or

$$I = I_o \left(1 + \frac{2\vec{P}_B \cdot \hat{n} \ \mathrm{Re}\left\{(\alpha + \beta)^*(i\gamma)\right\}}{I_o}\right) \quad ; \tag{1-28}$$

by comparison with Eq. (1-24) one gets

$$A(\theta) = P(\theta) = \frac{2\mathrm{Re}\left\{(\alpha + \beta)^*(i\gamma)\right\}}{I_o} \quad . \tag{1-29}$$

This formula can also be obtained directly by substituting for M in Eq. (1-19).

D. Small Angle Approximation

We are interested in the small angle region where the contributions of the electromagnetic interaction due to Coulomb repulsion and nucleon magnetic moments cannot be neglected. Each scattering amplitude is expressed as a sum of a nuclear term and an electromagnetic term, i.e., $\alpha = \alpha_N + \alpha_E$. Considering the electromagnetic contributions and forming the bilinear combinations of the amplitudes, Eqs. (1-27) and (1-29) can be grouped into three different terms corresponding to the pure nuclear term, the pure electromagnetic term and an interference term corresponding to the interference between nuclear and electromagnetic terms.

$$I_o = I_{oN} + I_{oE} + I_{oI}$$

where

$$\begin{aligned} I_{oN} &= |\alpha_N|^2 + 2|\gamma_N|^2 + |\beta_n|^2 + |\delta_N|^2 + |\epsilon_N|^2 \\ I_{oE} &= |\alpha_E|^2 + 2|\gamma_E|^2 + |\beta_E|^2 + |\delta_E|^2 + |\epsilon_E|^2 \\ I_{oI} &= 2\mathrm{Re}(\alpha_N^*\alpha_E) + 4\mathrm{Re}(\gamma_N^*\gamma_E) + 2\mathrm{Re}(\beta_N^*\beta_E) \\ &\quad + 2\mathrm{Re}(\delta_N^*\delta_E) + 2\mathrm{Re}(\epsilon_N^*\epsilon_E) . \end{aligned} \tag{1-30}$$

For the analyzing power we obtain

$$I_oA(\theta) = (I_oA)_N + (I_oA)_E + (I_oA)_I$$

where

$$(I_oA)_N = 2\mathrm{Re}\{(\alpha_N + \beta_N)^*(i\gamma_N)\}$$

$$(I_oA)_E = 2\mathrm{Re}\{(\alpha_E + \beta_E)^*(i\gamma_E)\} \tag{1-31}$$

$$(I_oA)_I = 2\mathrm{Re}\{(\alpha_N + \beta_N)^*(i\gamma_E)\} + 2\mathrm{Re}\{(\alpha_E + \beta_E)^*(i\gamma_N)\}$$

where the subscripts N, E, and I represent the pure nuclear, the pure electromagnetic and the interference term, respectively.

The small angle behaviour of the amplitudes at 800 MeV which were obtained from the Arndt phase shifts analysis (Arndt 80) are shown in Fig. (1-3) and Fig.(1-4). One observes that except for the real part of the electromagnetic spin flip amplitude, $\mathrm{Re}\gamma_E$, the real and imaginary parts of the electromagnetic spin-double-flip and spin-orbit amplitudes (β_E, δ_E, ε_E, γ_E) are negligible compared with those from the spin-independent Coulomb amplitude (α_E). Using an approximation where these terms are neglected Eqs. (1-30) and (1-31) can be written in the form of

$$I_{oN} = |\alpha_N|^2 + 2|\gamma_N|^2 + |\beta_N|^2 + |\delta_N|^2 + |\varepsilon_N|^2$$

$$I_{oE} \cong |\alpha_E|^2 \tag{1-32}$$

$$I_{oI} \cong 2\mathrm{Re}(\alpha_N^*\alpha_E)$$

and

$$(I_oA)_N = 2\mathrm{Im}\alpha_N\mathrm{Re}\gamma_N + 2\mathrm{Im}\beta_N\mathrm{Re}\gamma_N - 2\mathrm{Re}\alpha_N\mathrm{Im}\gamma_N - 2\mathrm{Re}\beta_N\mathrm{Im}\gamma_N$$

$$(I_oA)_E \cong 2\mathrm{Im}\alpha_E\,\mathrm{Re}\gamma_E - 2\mathrm{Re}\alpha_E\mathrm{Im}\gamma_E \qquad (1\text{-}33)$$

$$(I_oA)_I \cong 2\mathrm{Im}\alpha_E\,\mathrm{Re}\gamma_N - 2\mathrm{Re}\alpha_E\,\mathrm{Im}\gamma_N + 2\mathrm{Re}\gamma_E\,\mathrm{Im}\alpha_N\ .$$

A further approximation can be made in $(I_oA)_N$ by neglecting contributions from $\mathrm{Re}\alpha_N\mathrm{Im}\gamma_N$ and $\mathrm{Re}\beta_N\mathrm{Im}\gamma_N$ [see Fig. (1-3)] . Tables (1-1), (1-2) and (1-3) show the Arndt predictions (Arndt 80) for each of the remaining terms in $(I_oA)_N$, $(I_oA)_E$ and $(I_oA)_I$ for the angular range observed in this experiment. These tables make it clear that with a very good accuracy contributions from $\mathrm{Im}\beta_N\ \mathrm{Re}\gamma_N$ in $(I_oA)_N$, $\mathrm{Im}\alpha_E\ \mathrm{Re}\gamma_N$ in $(I_oA)_I$ and the pure electromagnetic term $(I_oA)_E$ can be neglected.

$$(I_oA)_N \cong 2\mathrm{Im}\alpha_N\,\mathrm{Re}\gamma_N$$

$$(I_oA)_I \cong 2\mathrm{Re}\gamma_E\,\mathrm{Im}\alpha_N - 2\mathrm{Re}\alpha_E\,\mathrm{Im}\gamma_N \qquad (1\text{-}34)$$

or

$$I_oA \cong 2\mathrm{Im}\alpha_N(\mathrm{Re}\gamma_N + \mathrm{Re}\gamma_E) - 2\mathrm{Re}\alpha_E\,\mathrm{Im}\gamma_N\ .$$

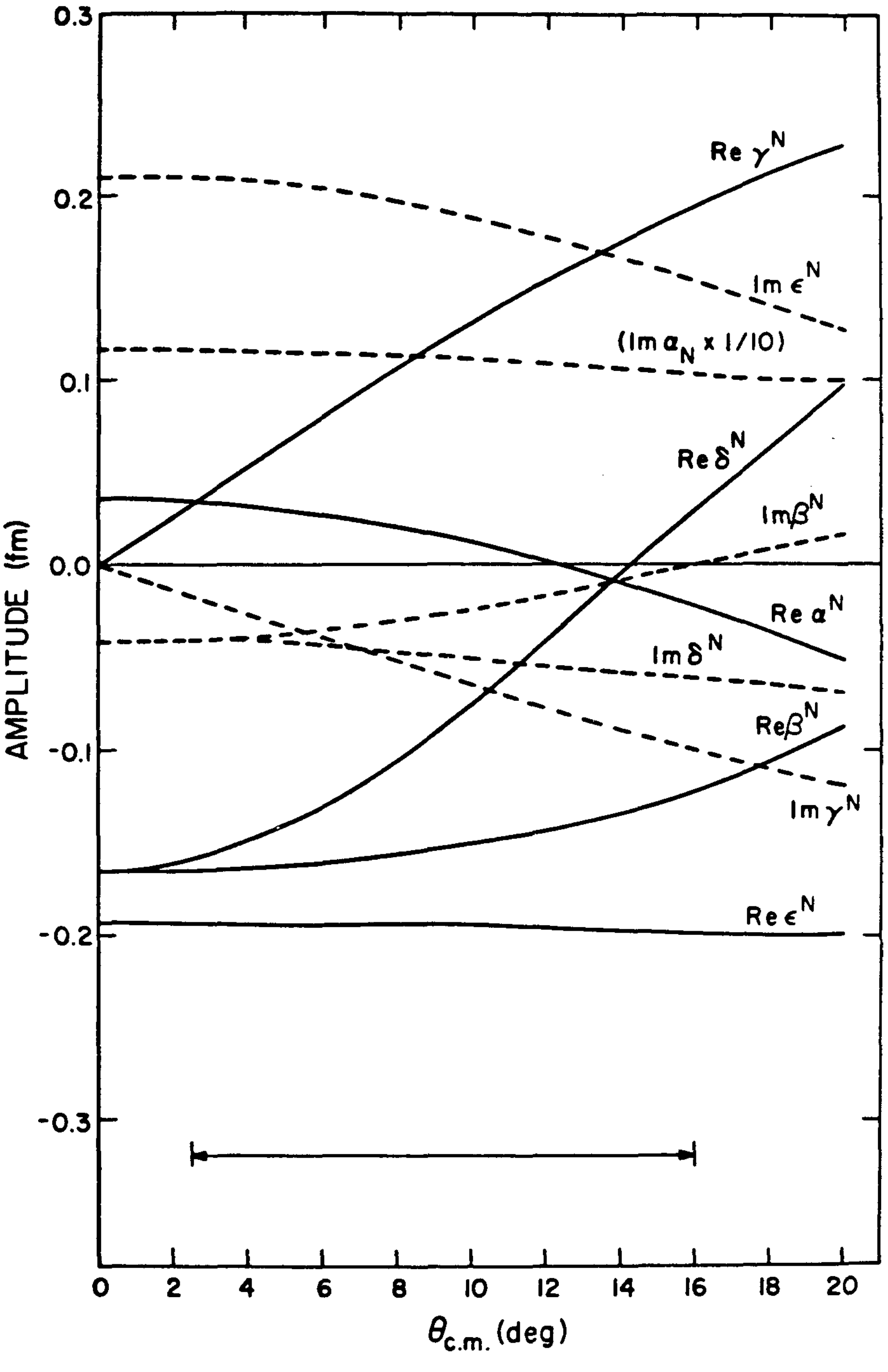

Fig. (1-3): The Arndt's phase shifts prediction for p-p hadronic scattering amplitudes at 800 MeV.

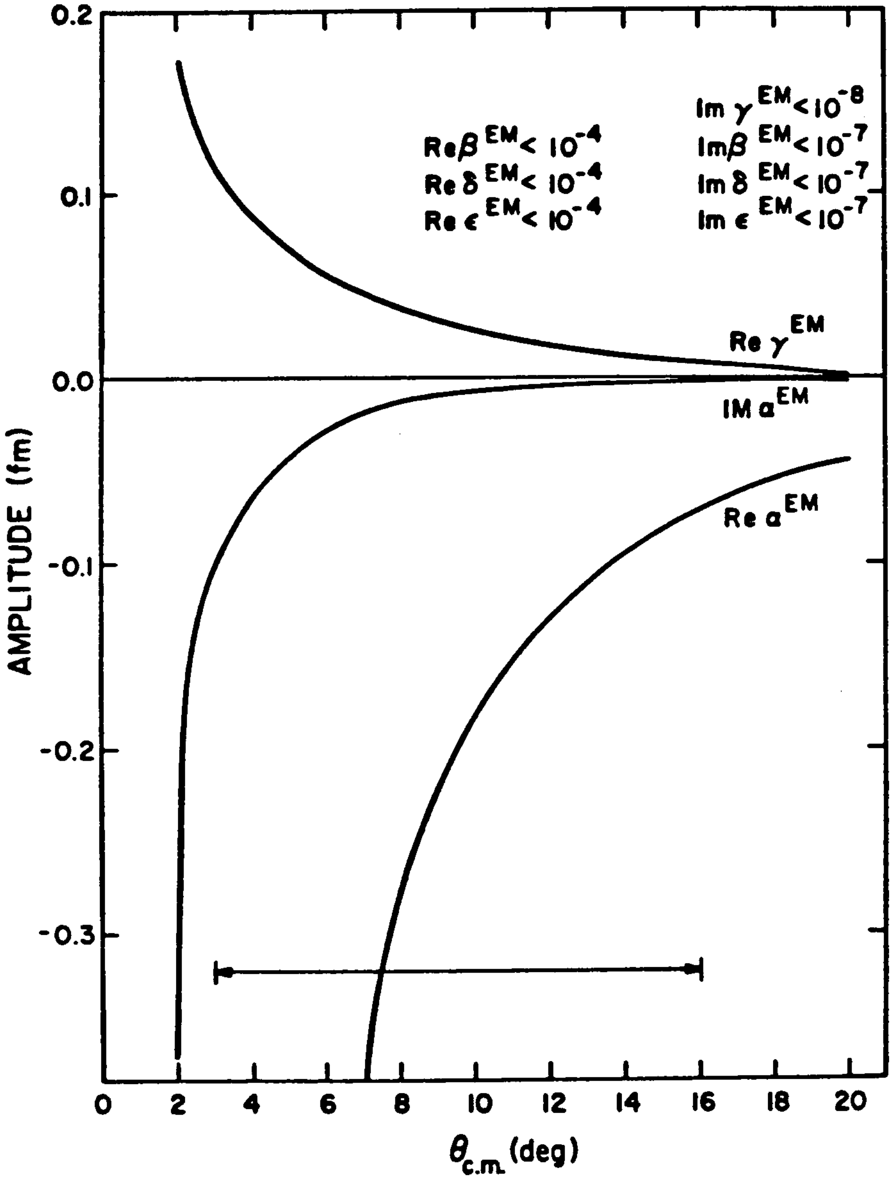

Fig. (1-4): Electromagnetic scattering amplitudes for p-p at 800 MeV obtained from the Arndt phase shifts.

θ^o_{cm}	$\mathrm{Im}\alpha_N\ \mathrm{Re}\gamma_N$	$\mathrm{Im}\beta_N\ \mathrm{Re}\gamma_N$
6	0.0920	-0.0028
8	0.1187	-0.0033
10	0.1443	-0.0033
12	0.1652	-0.0028
14	0.1855	-0.0018
16	0.1979	-0.0004

Table (1-1) - The Arndt phase shifts prediction for pure nuclear terms in (I_oA).

θ^o_{cm}	$\mathrm{Im}\alpha_E\ \mathrm{Re}\gamma_E$	$\mathrm{Re}\alpha_E\ \mathrm{Im}\gamma_E$
6	-0.0013	$<10^{-8}$
8	-0.0005	$<10^{-9}$
10	-0.0002	$<10^{-9}$
12	-0.0001	$<10^{-9}$
14	0.0	$<10^{-9}$
16	0.0	$<10^{-9}$

Table (1-2) - The Arndt phase shifts prediction for pure electromagnetic terms in (I_oA).

θ^o_{cm}	$\mathrm{Re}\gamma_E\ \mathrm{Im}\alpha_N$	$\mathrm{Re}\alpha_E\ \mathrm{Im}\gamma_N$	$\mathrm{Im}\alpha_E\ \mathrm{Re}\gamma_N$
6	0.0587	0.0204	0.0021
8	0.0396	0.0148	0.0014
10	0.0266	0.0120	0.0010
12	0.0184	0.0101	0.0008
14	0.0127	0.0084	0.0005
16	0.0074	0.0072	0.0004

Table (1-3) - The Arndt phase shifts prediction for interference terms in (I_oA).

E. Parameterization

The differential cross section Eq. (1-32) and analyzing power Eq. (1-34) formulae can be written as a function of t, the four-momentum transfer squared $\left(-t = q^2 = 2P_{cm}^2(1-\cos\theta_{cm})\right)$, and a set of parameters which have to be determined.

1. Cross Section

For the pure nuclear term in Eq. (1-32) we may use the following conventional parameterization known as the classical parameterization (Aebischer 77).

$$|\alpha_N|^2 = |\alpha_N(0)|^2 e^{b_1 t} \tag{1-35}$$

$$|\beta_N|^2 + |\delta_N|^2 + |\varepsilon_N|^2 = \left(|\beta_N(0)|^2 + |\delta_N(0)|^2 + |\varepsilon_N(0)|^2\right)e^{b_2 t} \quad , \tag{1-36}$$

where we make the traditional assumption that the slopes of the real and imaginary parts of the nuclear amplitudes are the same. It has been shown (Appendix B) that at t = 0

$$\beta(0) = \delta(0) \quad . \tag{1-37}$$

Define ρ as the ratio of the real part of spin-independent amplitude at zero degrees to imaginary part of spin-independent amplitude at zero degrees and define R as the ratio between the summed moduli squared of the double-spin-flip amplitudes at zero degrees and the modulus squared of the spin-independent amplitude at zero degrees.

$$\rho = \frac{\mathrm{Re}\,\alpha_N(0)}{\mathrm{Im}\,\alpha_N(0)} \tag{1-38}$$

$$R = \frac{2|\beta_N(0)|^2 + |\varepsilon_N(0)|^2}{|\alpha_N(0)|^2}. \tag{1-39}$$

Substituting Eq. (1-35) and Eq. (1-36) into Eq. (1-32) and using Eq. (1-39) we may write:

$$\left.\frac{d\sigma}{dt}\right|_N = \frac{\pi}{p^2}\left[|\alpha_N(0)|^2\left(e^{b_1 t} + Re^{b_2 t}\right) + 2|\gamma_N|^2\right] \tag{1-40}$$

where $d\sigma/dt = \pi/p^2\ d\sigma/d\Omega$ and p is the center-of-mass momentum. But

$$\begin{aligned} |\alpha_N(0)|^2 &= \left(\mathrm{Im}\,\alpha_N(0)\right)^2 + \left(\mathrm{Re}\,\alpha_N(0)\right)^2 \\ &= \left(1 + \rho^2\right)\left(\mathrm{Im}\,\alpha_N(0)\right)^2 \ . \end{aligned} \tag{1-41}$$

Now the optical theorem gives a relation between σ_{ToT} , the total reaction cross section and $\mathrm{Im}\,\alpha_N(0)$ (Appendix A):

$$\mathrm{Im}\,\alpha_N(0) = \frac{k}{4\pi}\,\sigma_{ToT}$$

Thus we may write:

$$\frac{d\sigma}{dt}\Big|_N = \frac{\pi}{p^2}\left[\frac{k^2}{16\pi^2}\sigma^2_{ToT}\left(1+\rho^2\right)\left(e^{b_1 t} + Re^{b_2 t}\right) + 2|\gamma_N|^2\right] \quad . \tag{1-42}$$

It has been shown (Appendix B) that the scattering amplitudes can be decomposed into partial waves; for example, we may write:

$$\gamma = \sum_{\ell\,\mathrm{odd}} \gamma_\ell P^1_\ell(\theta) \quad . \tag{1-43}$$

Here γ_ℓ is a coefficient which depends on the energy. This expansion is particularly useful when the number of partial waves is limited to some finite value ℓ_{max}, which is usually the case for the nuclear amplitudes. In Appendix B it has been shown that at small angles Eq. (1-43) can be reduced to the simple form

$$\gamma = \gamma_0 \sin\theta \quad . \tag{1-44}$$

Figure (1-3) shows Arndt prediction for the small angle dependence of the scattering amplitudes at 800 MeV. One observes that real and imaginary parts of the spin-orbit term show a sinusodal form that clarifies Eq. (1-44). Therefore we may parameterize the real and imaginary parts of γ_N in the following form,

$$\mathrm{Re}\gamma_N = \gamma_1 \sin\theta$$

$$\mathrm{Im}\gamma_N = \gamma_2 \sin\theta \quad .$$

After substitution into Eq. (1-42) one obtains

$$\frac{d\sigma}{dt}\Big|_N = \frac{\pi}{p^2}\left[\frac{k^2}{16\pi^2}\sigma^2_{ToT}\left(1+\rho^2\right)\left(e^{b_1 t} + Re^{b_2 t}\right) + 2\left(\gamma_1{}^2 + \gamma_2{}^2\right)\sin^2\theta\right]. \quad (1\text{-}45)$$

The spin-independent electromagnetic amplitude which corresponds to the one-photon exchange has been given by Bethe (Bethe 58):

$$\alpha_E = -\frac{2\hbar P}{137\beta_L t}\, e^{i\delta_c}\, G_p^2(t) \qquad (1\text{-}46)$$

where P is the momentum of the incident particle in the center-of-mass system, β_L is the velocity of the projectile in the laboratory frame (in units of c) and $G_p(t)$ is the electromagnetic form factor for proton-proton scattering. $G_p(t)$ has the following empirical form

$$G_p(t) = \frac{1}{\left(1 + |t|/c\right)^2} \qquad (1\text{-}47)$$

where c has been found from a dipole fit (Coward 68)

$$c = 0.71\ (\mathrm{GeV}/c)^2 \ .$$

δ_c is the Coulomb angle, which is a modification to the nuclear phase shift due to the presence of the Coulomb potential. It has been calculated non-relativistically by Bethe (Bethe 58) as

$$\delta_c = \frac{2}{137\beta_L} \mathrm{Ln}\left(\frac{0.209}{a\sqrt{|t|}}\right) \tag{1-48}$$

where a is the radius of interaction region (1 fm). A relativistic expression has been given by Locher (Locher 67),

$$\delta_c = \frac{2}{137\beta_L} \left[\mathrm{Ln}\frac{2}{\theta} - \mathrm{Ln}\left(\frac{2}{3}\right)^{1/2} RP - \frac{\gamma}{2}\right] \tag{1-49}$$

which yields a similar value of δ_c . Here R ~1.5-fm is the effective strong interaction radius. $\gamma = 0.577$ is the Euler constant, and θ and P are the center-of-mass scattering angle and momentum, respectively.

From the above considerations the electromagnetic contribution to the cross section is

$$\frac{d\sigma}{dt}\Big|_E = \frac{4\pi\hbar^2}{(137)^2\ \beta_L^2 t^2}\, G_p^4(t) \quad . \tag{1-50}$$

The contribution to the cross section due to the interference term in Eq. (1-32) may be written in the form of

$$\frac{d\sigma}{dt}\Big|_I = \frac{\pi}{p^2}\left[2\mathrm{Re}(\alpha_N^*\alpha_E)\right]$$

$$= \frac{2\pi}{p^2}\left(\mathrm{Re}\alpha_N \mathrm{Re}\alpha_E + \mathrm{Im}\alpha_N \mathrm{Im}\alpha_E\right) \quad .$$

Using Eq. (1-38) and the parameterization given by Eq. (1-35) for the t dependence of $|\alpha_N(t)|^2$ we can write:

$$\frac{d\sigma}{dt}\Big|_I = \frac{2\pi}{p^2}\,\mathrm{Im}\alpha_N(o)e^{b_1 t/2}\left(\rho\mathrm{Re}\alpha_E + \mathrm{Im}\alpha_E\right)$$

$$= \frac{k}{2p^2}\,\sigma_{ToT}e^{b_1 t/2}\left(\rho\mathrm{Re}\alpha_E + \mathrm{Im}\alpha_E\right) \tag{1-51}$$

where in the last step we have used the optical theorem.

Substituting the real and imaginary parts of α_E from Eq. (1-46) into Eq. (1-51) one obtains

$$\left.\frac{d\sigma}{dt}\right|_I = -\frac{\sigma_{ToT}G_p^2(t)}{137\beta_L t}\left(\rho\cos\delta_c + \sin\delta_c\right)e^{b_1 t/2} \quad . \tag{1-52}$$

Now for an 800 MeV proton beam the value of δ_c in the range of four-momentum transfer squared, t, covered in this experiment is very small. We will therefore write

$$\left.\frac{d\sigma}{dt}\right|_I = -\frac{\sigma_{ToT}G_p^2(t)}{137\beta_L t}\left(\rho + \delta_c\right)e^{b_1 t/2} \tag{1-53}$$

where the approximations $\cos\delta_c \simeq 1$ and $\sin\delta_c \simeq \delta_L$ have been used.

Combining Eqs. (1-45), (1-50), and (1-53), we obtain the elastic cross section for small angle proton-proton scattering in terms of ρ, R, σ_{ToT}, b_1, b_2, γ_1, and γ_2 as:

$$\frac{d\sigma}{dt} = \frac{\sigma^2_{ToT}}{16\pi\hbar^2}(1 + \rho^2)\left(e^{b_1 t} + Re^{b_2 t}\right)$$

$$- \frac{\sigma_{ToT}G^2_p(t)}{137\beta_L t}(\rho + \delta_c)e^{b_1 t/2}$$

$$+ \frac{4\pi\hbar^2}{(137)^2\beta^2_L t^2}G^4_p(t) + \frac{2\pi}{p^2}\left({\gamma^2}_1 + {\gamma^2}_2\right)\sin^2\theta \quad . \qquad (1\text{-}54)$$

2. Analyzing Power

Here again we may use the same functional form for $Im\alpha_N$ and γ_N defined in Eq. (1-35) and Eq. (1-44) respectively

$$Im\alpha_N = Im\alpha_N(o)e^{b_1 t/2}$$

$$Re\gamma_N = \gamma_1\sin\theta$$

$$Im\gamma_N = \gamma_2\sin\theta \quad .$$

The pure nuclear term in Eq. (1-34) can therefore be written in the form:

$$(I_oA)_N = 2\gamma_1 Im\alpha_N(o)e^{b_1 t/2}\sin\theta$$

and by using the optical theorem, we obtain

$$(I_oA)_N = \frac{k\gamma_1}{2\pi}\,\sigma_{ToT}e^{b_1t/2}\sin\theta \quad . \tag{1-55}$$

From Eq. (1-46) the real part of spin-independent electromagnetic amplitude has the form:

$$\mathrm{Re}\,\alpha_E = -\frac{2\hbar P}{137\beta_L t}\,G_p^2(t) \quad . \tag{1-56}$$

The spin-orbit electromagnetic amplitude correspond to the one photon exchange is (Bourrely 74)

$$\begin{aligned}\mathrm{Re}\,\gamma_E = {} & \frac{\sqrt{\omega^2 - m^2 + 1/4t}}{2 \times 137\omega(\omega + m)\sqrt{|t|}}\,G_p^2(t)\Big\{\Big[2\omega + m + \frac{t}{4(\omega + m)} \\ & + \frac{(\mu - 1)}{m}\,\big[3\omega(\omega + m) + t\big] \\ & + \frac{(\mu - 1)^2}{4m^2(\omega + m)}\,t\big[2\omega^2 + 3\omega m + m^2 + \tfrac{1}{4}\,t\big]\Big]\Big\}\end{aligned} \tag{1-57}$$

where $\omega = 1/2\,\sqrt{s}$, μ and m are the respective magnetic moment and mass of the proton and G_p (t) is proton form factor defined in Eq. (1-47).

Substituting for $\mathrm{Im}\alpha_N$, $\mathrm{Im}\gamma_N$, and $\mathrm{Re}\alpha_E$ in the interference term represented by Eq. (1-34), we obtain:

$$(I_oA)_I = \frac{k}{2\pi}\sigma_{ToT}\,e^{b_1t/2}\,\mathrm{Re}\gamma_E + \frac{4\hbar P\gamma_2}{137\beta_L t}G_p^2(t)\sin\theta \tag{1-58}$$

where $\mathrm{Re}\gamma_E$ is given by (1-57) .

Combining Eqs. (1-55) and (1-58), we obtain the expression for (I_oA) in terms of σ_{ToT}, b_1, γ_1, and γ_2 as:

$$\begin{aligned}(I_oA) &\cong (I_oA)_I + (I_oA)_N\\ &\cong \frac{k}{2\pi}\sigma_{ToT}\,e^{b_1t/2}\,\mathrm{Re}\gamma_E + \frac{4\hbar P\gamma_2}{137\beta_L t}G_p^2(t)\sin\theta\\ &\quad + \frac{k\gamma_1}{2\pi}\sigma_{ToT}\,e^{b_1t/2}\sin\theta \quad .\end{aligned} \tag{1-59}$$

CHAPTER II

THEORETICAL ASPECTS FOR PROTON-DEUTERON DATA

In this chapter a brief exposition of the theory of hadron-deuteron scattering developed by Alberi et al. (Alberi 79) is presented. We will discuss the essential aspects of this theory which was used in the analysis of the p-d data obtained in this work. We also parametrize the p-d elastic analyzing power, $A_y(\theta)$, in terms of nucleon-nucleon amplitudes.

A. The Breit Frame (Hagedorn 73)

Most of the calculation for the proton-deuteron problem is performed in the Breit frame. Consider an elastic scattering event and define the momenta before and after scattering, as shown in Fig. (2-1).

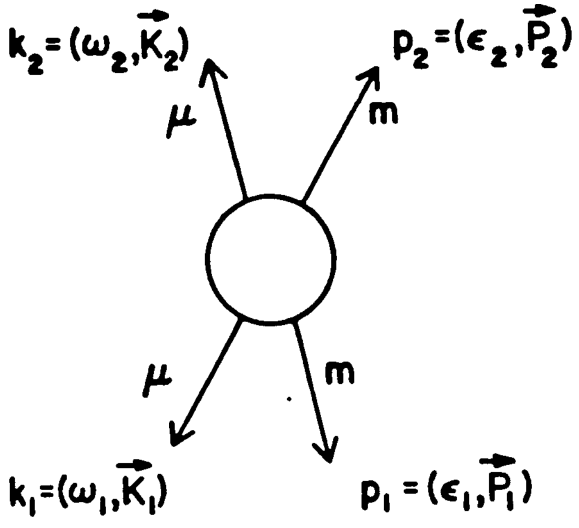

Fig. (2-1): Two Body Scattering Schemes.

We apply a Lorentz transformation such that $\vec{K}_1 + \vec{K}_2 = 0$. Therefore k_1 and k_2 will have the form

$$k_1 = (\omega, \vec{K}) \tag{2-1}$$

$$k_2 = (\omega, -\vec{K}) \quad .$$

From energy conservation it follows that the energies of the particle with mass m before and after the collision, ε_1 and ε_2 must be equal, $\varepsilon_1 = \varepsilon_2 = \varepsilon$; hence $|\vec{P}_1| = |\vec{P}_2|$ and

$$P_1 = (\varepsilon, \vec{P}_1)$$

$$P_2 = (\varepsilon, \vec{P}_2) \tag{2-2}$$

with

$$|\vec{P}_1| = |\vec{P}_2| = \sqrt{\varepsilon^2 - m^2} \quad .$$

From $k_1 - k_2 = P_2 - P_1$ follows

$$k_1 - k_2 = (0, 2\vec{K}) = P_2 - P_1 = (0, \vec{P}_2 - \vec{P}_1) \quad . \tag{2-3}$$

$2\vec{K}$ is the "three-momentum transfer".

Equations (2-1), (2-2) and (2-3) yield the following picture. All particles seem to be reflected on a hard wall; the particle with mass μ perpendicularly [see Fig. (2-2)].

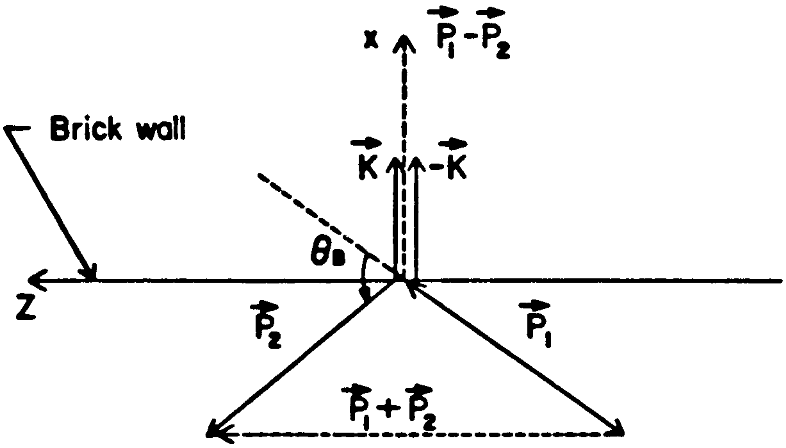

Fig. (2-2): The Breit System.

The advantage gained by working in the Briet frame is; first, the use of a non-relativistic deuteron wave function is better justified, and second, the proton scattering angle is smaller in the Breit frame than in center-of-mass frame. Therefore, the Glauber theory is more valid.

B. Nucleon-Nucleon Amplitudes in Breit Frame

In the deuteron Breit frame the nucleon-nucleon amplitudes have the following general form:

$$f^{(j)} = f_1^{(j)} + if_6^{(j)} \; \hat{n}_j \cdot \vec{\sigma}_1 + f_2^{(j)} \hat{n}_j \cdot \vec{\sigma}_2 + f_3^{(j)} (\hat{n}_j \cdot \vec{\sigma}_1)(\hat{n}_j \cdot \vec{\sigma}_2)$$
$$+ f_4^{(j)}(\hat{d}_j \cdot \vec{\sigma}_1)(\hat{d}_j \cdot \vec{\sigma}_2) + f_5^{(j)} (\hat{m}_j \cdot \vec{\sigma}_1)(\hat{m}_j \cdot \vec{\sigma}_2) \; . \qquad (2\text{-}4)$$

Here, the Pauli matrices σ_1 and σ_2 refer to the projectile and target, respectively. The unit vectors m_j, d_j and n_j are taken along the average projectile momenta, $1/2(\vec{P}_1 + \vec{P}_2)$, the momentum transfer, $\vec{P}_1 - \vec{P}_2$, and perpendicular to the scattering plane, $\vec{P}_1 \times \vec{P}_2$, respectively. The superscript j is introduced to indicate that the amplitudes are evaluated in different configurations. $j = 0$ refers to the single scattering, $j = 1$ to the first scattering in the double scattering amplitude and $j = 2$ to the second one. The amplitudes of $f_1^{(j)}$---$f_6^{(j)}$ are functions of energies and momentum transfers in the p-d scattering process (this is because in the single scattering process the nucleon which interacts with the projectile recoils with the same momentum transfer as the whole deuteron system does) which is different for $j = 0$ and $j = 1,2$. The Breit amplitudes can be related directly to the nucleon-nucleon amplitudes in the center-of-mass (α, γ, β, δ, ϵ) defined in Chapter I, through a Wigner rotation (Gasiorowicz 66).

C. Proton-Deuteron Scattering Formalism

The p-d matrix is, in general composed of 12 independent complex amplitudes, as follows from time reversal and parity invariance symmetries. A convenient decomposition of the p-d collision matrix $\hat{F}$ in the deuteron Breit frame (deuteron reverses its three-momentum in the scattering) in terms of the spin-1/2 operators (proton) $\hat{\sigma}_0$, $\hat{\sigma}_x$, $\hat{\sigma}_y$ and $\hat{\sigma}_z$, the spin-1 operators (deuteron) $\hat{\sigma}_0$, $\hat{j}_x$, $\hat{j}_y$, $\hat{j}_z$, and the quadrupole operators $\hat{Q}_{ik} = 1/2(\hat{j}_i\hat{j}_k + \hat{j}_k\hat{j}_i) - 2/3\delta_{ik}\hat{\sigma}_o$ $i,k = x,y,z$ has the form of (Alberi 79):

$$\hat{F} = \hat{F}^o\hat{\sigma}_o + \hat{F}^x\hat{\sigma}_x + \hat{F}^y\hat{\sigma}_y + \hat{F}^y\hat{\sigma}_z \ ,$$

where

$$\begin{aligned}
\hat{F}^o &= F^o_o\hat{\sigma}_o + F^o_y\hat{j}_y + F^o_{xx}\,\hat{Q}_{xx} + F^o_{yy}\hat{Q}_{yy} \ , \\
\hat{F}^x &= F^x_x\hat{j}_x + F^x_{xy}\hat{Q}_{xy} \\
\hat{F}^y &= F^y_o\hat{\sigma}_o + F^y_y\hat{j}_y + F^y_{xx}\hat{Q}_{xx} + F^y_{yy}\hat{Q}_{yy} \\
\hat{F}^z &= F^z_z\hat{j}_z + F^z_{yz}\hat{Q}_{yz} \ .
\end{aligned} \tag{2-5}$$

Here, x is along the momentum transfer, z is along the average of the initial and the final momenta of the projectile and y is orthogonal to the scattering plane [see Fig. (2-2)]. Alberi et al. (Alberi 80) have calculated all 12 amplitudes within the multiple scattering formalism based on invariant Feynman diagrams. They calculate the proton-deuteron scattering amplitude in the deuteron Breit frame, where the use of non-relativistic wave function for the deuteron is best justified. These calculations are rather lengthy and not transparent, and we will outline briefly their method of calculation.

In their approach, which is similar to that used in the Glauber model, only the single (F_s amplitude) and the double scattering (F_D amplitude) terms are included. F_s and F_D, when written out in terms of the proton-proton amplitude, f, the proton-neuteron amplitude, g, and the deuteron wave function, $\psi(\vec{r})$, have the form of

$$\hat{F}_s(\vec{q}) = \int d^3r \; e^{-i\vec{Q}\cdot\vec{r}/2} \; \psi^{\dagger}(\vec{r})[f^{o}(\vec{Q}) + g^{o}(\vec{Q})]\psi(\vec{r}) \tag{2-6}$$

and

$$\hat{F}_D(\vec{Q}) = -\frac{1}{m}(2\pi)^{-3} \int d^3q \; G_o \int d^3r \; e^{-i\vec{q}\cdot\vec{r}} \; \psi^{\dagger}(\vec{r})[g^{(2)}\,(\vec{Q}/2)f^{(1)}(Q/2)$$

$$+ f^2(Q/2)g^{(1)}(Q/2)]\psi(\vec{r}). \tag{2-7}$$

G_o, which appears in the double scattering term, is the exact free wave propagator. The amplitudes f and g depend only on the three momentum transfer $\vec{Q}$, ($\vec{Q}$ is momentum transfer of p-d scattering process). The momentum dependence, q, of them is neglected compared to that coming from the wave functions of deuteron. After substitution for f and g from Eq. (2-4) and performing the algebra on the Pauli matrices, the integral over $\vec{r}$ is evaluated and expressed in terms of form factors. In the double scattering term the q integral, involving a form factor and the propagator is performed analytically by parametrizing form factor as a sum of Gaussians. After some algebra and symmetrization, the scattering matrix can be expressed in terms of the spin-1 operators $\hat{j}$, $\hat{Q}_{ik}$. The nucleon-nucleon amplitudes defined in (2-4), can be obtained from the nucleon-nucleon amplitudes in the center-of-mass (α, γ, β, ε and δ) through a Wigner rotation.

For p-d scattering, the density matrix is 6 x 6. In analogy with Eq. (1-20), the density matrix for the scattering of a polarized proton beam on an unpolarized deuteron target has the form of:

$$\rho = 1/6\ \hat{\sigma}_o + 1/6 \sum_{\mu=1}^{3} \langle\sigma_\mu^{(1)}\rangle\ \sigma_\mu^{(1)}\sigma_o^{(2)} \qquad (2\text{-}8)$$

where $\vec{P}_B = \sum_{\mu=1}^{3} \langle\sigma_\mu^{(1)}\rangle\hat{\mu}$ is the beam polarization vector and, superscript 1 and 2 stands for projectile and target. As shown in Chapter I, the differential cross section is given by

$$I = \mathrm{Tr}(F\rho F^\dagger)\ . \qquad (2\text{-}9)$$

After substitution for ρ in Eq. (2-9) from Eq. (2-8), one obtains:

$$I = 1/6\ (FF^\dagger) + 1/6 \sum_{\mu=1}^{3} \vec{P}_B \cdot \hat{\mu}\mathrm{Tr}\big(F\sigma_\mu^{(1)}\ \sigma_o^{(2)}\ F^\dagger\big)\ . \qquad (2\text{-}10)$$

The first term on the right-hand side is the differential cross section, I_o, for scattering of unpolarized proton beam on an unpolarized deuteron, and the second term is the contribution due to the initial polarization $\vec{P}_B$. After substitution of the collision matrix, $\hat{F}$, one gets:

$$I = I_o + 2\vec{P}_B \cdot \hat{n}\mathrm{Re}\big(\mathrm{Tr}(F^{o\dagger}F^y)\big)\ , \qquad (2\text{-}11)$$

where

$$I_o = 1/6\ \mathrm{Tr}(F^\dagger F),$$

and $\hat{n}$ is normal to the scattering plane. In Chapter I it was shown that

$$I = I_o(1 + \vec{P}_B \cdot \hat{n}P) \ ,$$

where P is the analyzing power. By comparison of this formula with (2-11), one gets the following expression for the proton-deuteron elastic analyzing power

$$A_y(\theta) = P(\theta) = \frac{2\mathrm{Re}\left(\mathrm{Tr}(F^{o\dagger}F^y)\right)}{\mathrm{Tr}(F^\dagger F)} \ . \tag{2-12}$$

After expressing the amplitudes F^i in terms of p-p and p-n amplitude in I_o and $A_y(\theta)$, one gets a rather lengthy expression for differential cross section, I_o, and analyzing power, $A_y(\theta)$. Figures (2-3) and (2-4) display the prediction of this theory for the elastic differential cross section and the analyzing power in p-d scattering, using the Arndt phase shifts prediction for the nucleon-nucleon amplitudes (Arndt 80) as input (solid lines). The dot-dashed curves were calculated in the single scattering approximation. The dashed curves were calculated without considering contribution of the double-spin-flip nucleon-nucleon amplitudes.

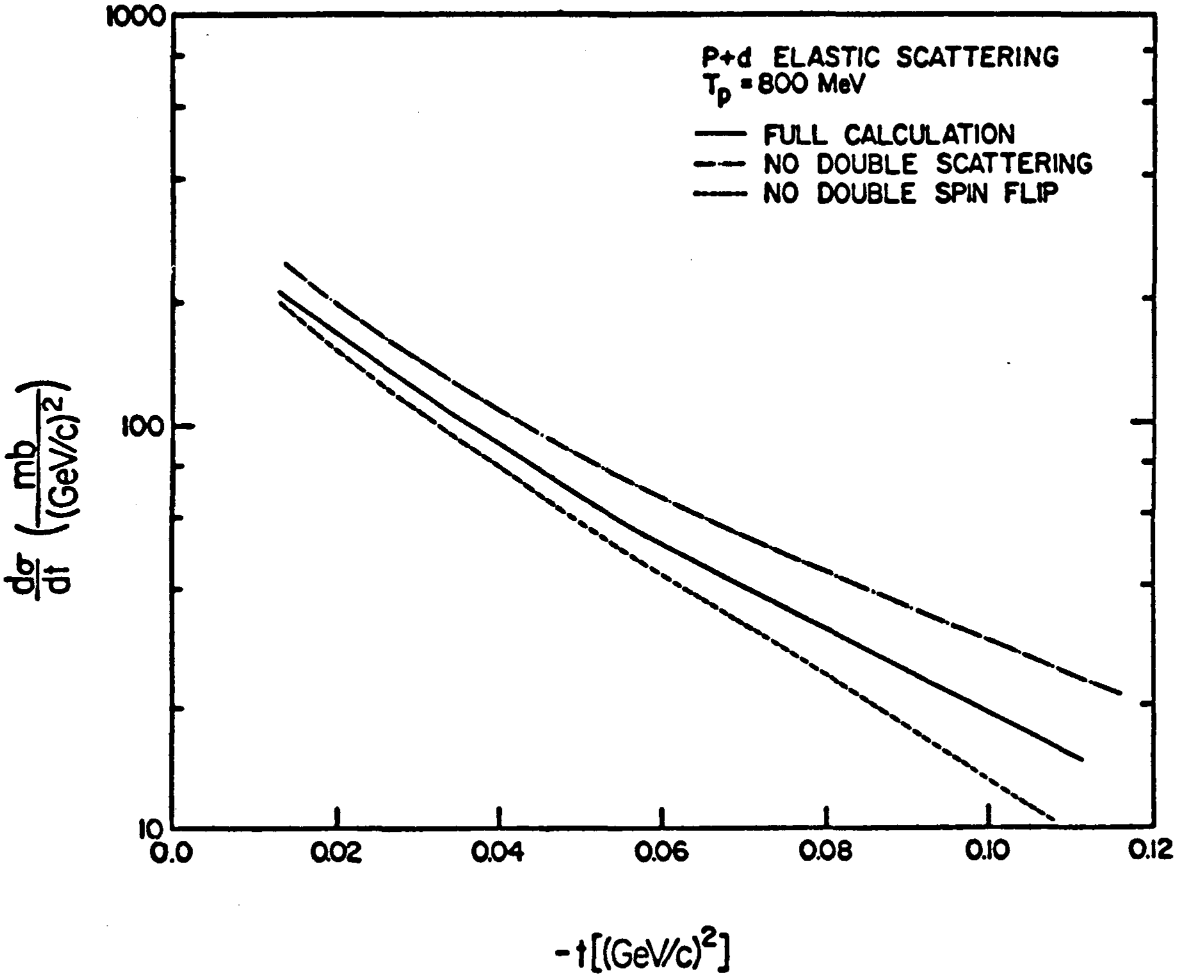

Fig. (2-3): Alberi et al. prediction for p-d elastic differential cross section using the Arndt phase shifts prediction for nucleon-nucleon amplitudes at 800 MeV as input.

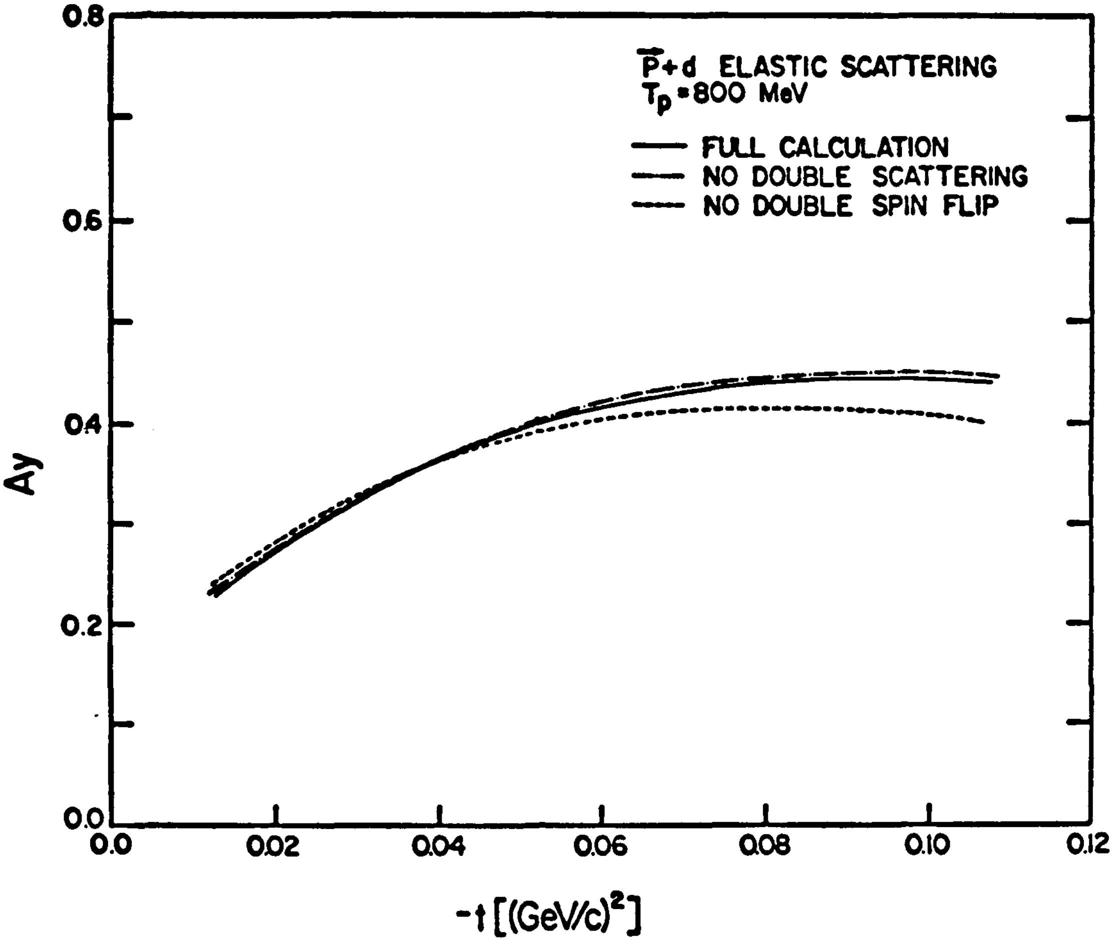

Fig. (2-4): Alberi et al. prediction for $\vec{p}$-d elastic analyzing power using the Arndt phase shifts prediction for nucleon-nucleon amplitudes at 800 MeV as input.

It is seen that, in contrast to the analyzing power where the double scattering term plays at most a ~5% role, at $|t| = 0.1$ (GeV/c)^2, the differential cross section is more strongly effected by the double scattering. The reason for this is that the analyzing power, $A_y(\theta)$, is given as a ratio of two expressions (2-12), and the double scattering process will contribute approximately equally to the denominator and numerator (Bleszynski 80). Also, at small angles the d-wave part of the deuteron wave function gives a rather small contribution. Thus the analyzing power in p-d elastic scattering at small angles appears to be a very simple tool for extracting the spin-orbit part of the p-n amplitude.

All of this leads to the following simple result for the analyzing power, $A_y(\theta)$ at small four-momentum transfer $|t| \lesssim 0.1$ (GeV/c)^2:

$$A_y(\theta) \cong 2\mathrm{Re}\left[(\bar{\alpha} + \bar{\beta})^*(i\bar{\gamma})\right]/\left[|\tilde{\alpha}|^2 + 2|\bar{\gamma}|^2 + |\bar{\beta}|^2 + |\bar{\varepsilon}|^2 + |\bar{\delta}|^2\right] , \tag{2-13}$$

where

$$\bar{\alpha} = \frac{1}{2}(\alpha_{pp} + \alpha_{pn}) ,$$

$$\bar{\gamma} = \frac{1}{2}(\gamma_{pp} + \gamma_{pn}) ,$$

$$\bar{\beta} = \frac{1}{2}(\beta_{pp} + \beta_{pn}) , \qquad (2\text{-}14)$$

$$\bar{\varepsilon} = \frac{1}{2}(\varepsilon_{pp} + \varepsilon_{pn}) ,$$

$$\bar{\delta} = \frac{1}{2}(\delta_{pp} + \delta_{pn}) ,$$

are the isospin averaged nucleon-nucleon amplitudes defined in Chapter I. A further approximation can be made by neglecting contribution from the double-spin flip amplitudes [see Fig. (2-4)]

$$A_y(\theta) \cong \frac{2\mathrm{Re}\left[(\bar{\alpha})^{*}(i\bar{\gamma})\right]}{|\bar{\alpha}|^2 + 2|\bar{\gamma}|^2} . \qquad (2\text{-}15)$$

We may introduce the same parameterization used in Chapter I [Eq. (1-35) and Eq. (1-44)] for spin-independent and spin-orbit nucleon-nucleon amplitudes

$$\begin{aligned} \alpha_{pp} &= \alpha_{pp}(0)e^{b_p t/2} , \\ \alpha_{pn} &= \alpha_{pn}(0)e^{b_n t/2} , \\ \gamma_{pp} &= (\gamma_{1p} + i\gamma_{2p})\sin\theta , \\ \gamma_{pn} &= (\gamma_{1n} + i\gamma_{2n})\sin\theta , \end{aligned} \qquad (2\text{-}16)$$

where θ is center-of-mass scattering angle, and, -t, is the four momentum transfer. We define ρ_{pp} (ρ_{pn}) as the ratio of the real part of the spin-independent pp(pn) amplitude to imaginary part of the spin-independent pp(pn) amplitude for t = 0. By making the traditional assumption that the slopes of the real and imaginary parts of the spin-independent nuclear amplitudes are the same and using the optical theorem ($\mathrm{Im}\alpha(0) = k/4\pi\ \sigma_{ToT}$), Eq. (2-16) can be written in the form of:

$$\mathrm{Re}\alpha_{pp} + i\mathrm{Im}\alpha_{pp} = \frac{k\sigma_p}{4\pi}(i + \rho_{pp})e^{b_p t/2} ,$$

and (2-17)

$$\mathrm{Re}\alpha_{pn} + i\mathrm{Im}\alpha_{pn} = \frac{k\sigma_n}{4\pi}(1 + \rho_{pn})e^{b_n t/2} ,$$

where k is the center-of-mass wave number for nucleon-nucleon scattering, and σ_p and σ_n are total reaction cross section for p-p and p-n scattering, respectively at 800 MeV.

After substitution for α_{pp}, α_{pn}, γ_{pp} and γ_{pn} in Eq. (2-15) one obtains the expression for the elastic proton-deuteron analyzing power in terms of ρ_{pp}, ρ_{pn}, σ_p, σ_n, b_p, b_n, γ_{1p}, γ_{2p}, γ_{1n}, and γ_{2n}:

$$A_y(\theta) = \frac{k[\sigma_p(A-\rho_{pp}B)e^{b_p t/2} + \sigma_n(A - \rho_{pn}B)e^{b_n t/2}]\sin\theta}{4\pi I_o} \qquad (2\text{-}18)$$

where

$$I_o = |\bar{\alpha}|^2 + 2|\bar{\gamma}|^2 = \frac{k^2}{64\pi^2}\left[\left(\sigma_p e^{b_p t/2} + \sigma_n e^{b_n t/2}\right)^2 + \left(\rho_{pp}\sigma_p e^{b_p t/2} + \rho_{pn}\sigma_n e^{b_n t/2}\right)^2\right] + 2(A^2 + B^2)\sin^2\theta$$

and

$$A = \frac{1}{2}(\gamma_{1p} + \gamma_{1n})$$

$$B = \frac{1}{2}(\gamma_{2p} + \gamma_{2n}) \; . \qquad (2\text{-}19)$$

CHAPTER III

EXPERIMENTAL SETUP

The experiment reported in this dissertation was performed on the External Proton Beam (EPB) facility at the Clinton P. Anderson Meson Physics Facility (LAMPF).

A beam of protons with an energy of 800 MeV traversed a volume of gas in the scattering chamber and the scattered recoil particles traversed a system of apertures before entering the detector telescope.

A. The Proton Beam

The LAMPF facility is an 800 MeV linear proton accelerator capable of simultaneously accelerating protons (H^+) and negative hydrogen atoms (H^-) and supplying them to several experimental areas. A H^- polarized beam is also available. The macroscopic duty factor is 6%. This consists of a 500 μs macropulse at 120 cycles per second. Each macropulse has a microstructure consisting of 0.25 ns wide bursts every 5 ns. A chopped RF beam can run at 40 ns or 80 ns. "Experimental Area B", which contains several secondary beam lines, including EPB, is shown in Fig. (3-1). Line B brings an H^- beam from the LAMPF switchyard to EPB. Upstream from our scattering chamber the H^- beam was changed to an H^+ (proton) beam by passing it through a thin foil. This was necessary since otherwise the H^- beam would have dissociated into a proton and two ~400 keV electrons after entrance window of the scattering chamber, and the 400 keV electrons could cause unwanted noise in our detectors. The EPB has three quadrapole

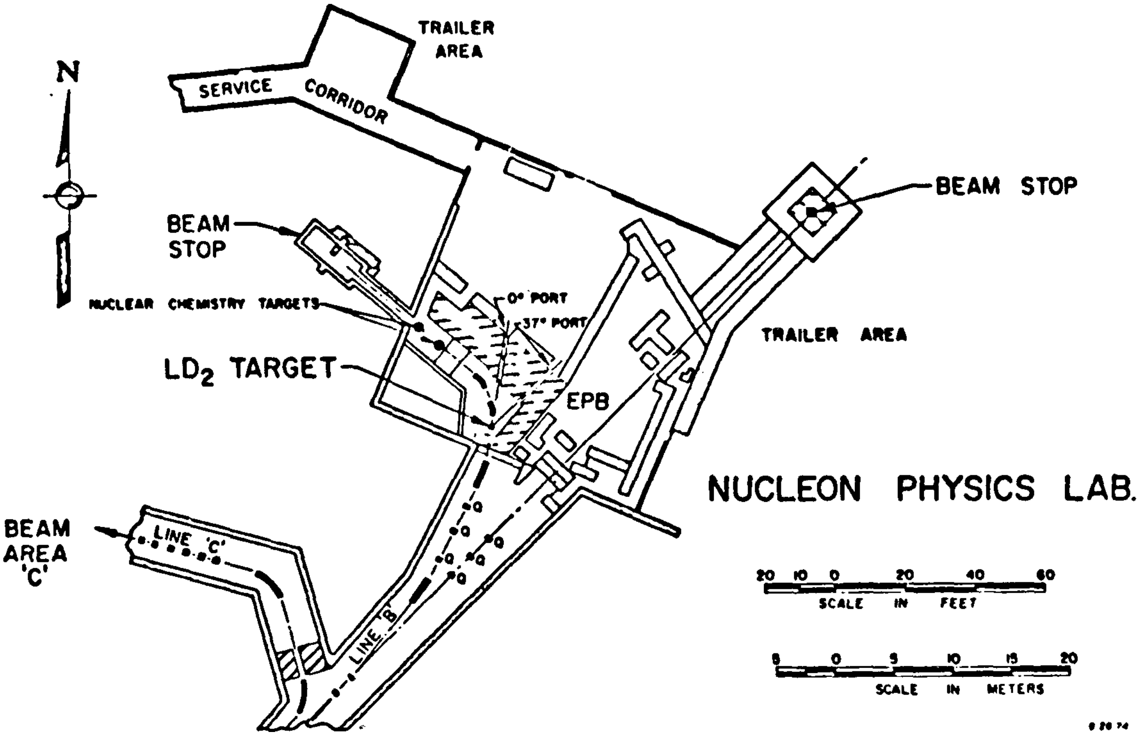

Fig. (3-1): Experimental Area B at LAMPF.

magnets which may be used to adjust the spot size of the beam at various locations in the line. Usually EPB provides a 3-mm diameter pencil beam with low intensity $\leq$ 10 nA. The energy of the LAMPF accelerator was estimated to be 796 ± 2 MeV. This value was obtained from the magnetic field setting of the LAMPF High Resolution Spectrometer (HRS) for elastically scattered protons. The energy obtained from the HRS was found to agree to better than 1 MeV with a simultaneous determination made by laser dissociation of H^- ions (Clark 79).

For the first part of this experiment a beam of unpolarized protons with an intensity of about 2 nA was used; and for the second part (time-of-flight) a chopped bursts 40 ns apart, unpolarized proton beam with an intensity of about 10 nA was used. In the third and fourth parts of this experiment a beam of polarized protons with an intensity of about 2 nA was used.

B. Scattering Chamber

A view of the scattering chamber is shown in Fig. (3-2). It is a box with dimensions 63 cm x 33 cm x 25 cm (width x length x height). The entrance and exit windows are 5 mil thick kapton. Two sets of solid state detector telescopes were mounted on movable arms. Directly in front of each detector telescope there is a circular slit of 6.3-mm thick brass with a radius of 3.96 mm. This radius is commensurate with the active areas of the solid state detectors placed behind it and the recoil particle trajectories through the collimation system. In the front, 5.08 cm from the beam line, there is an

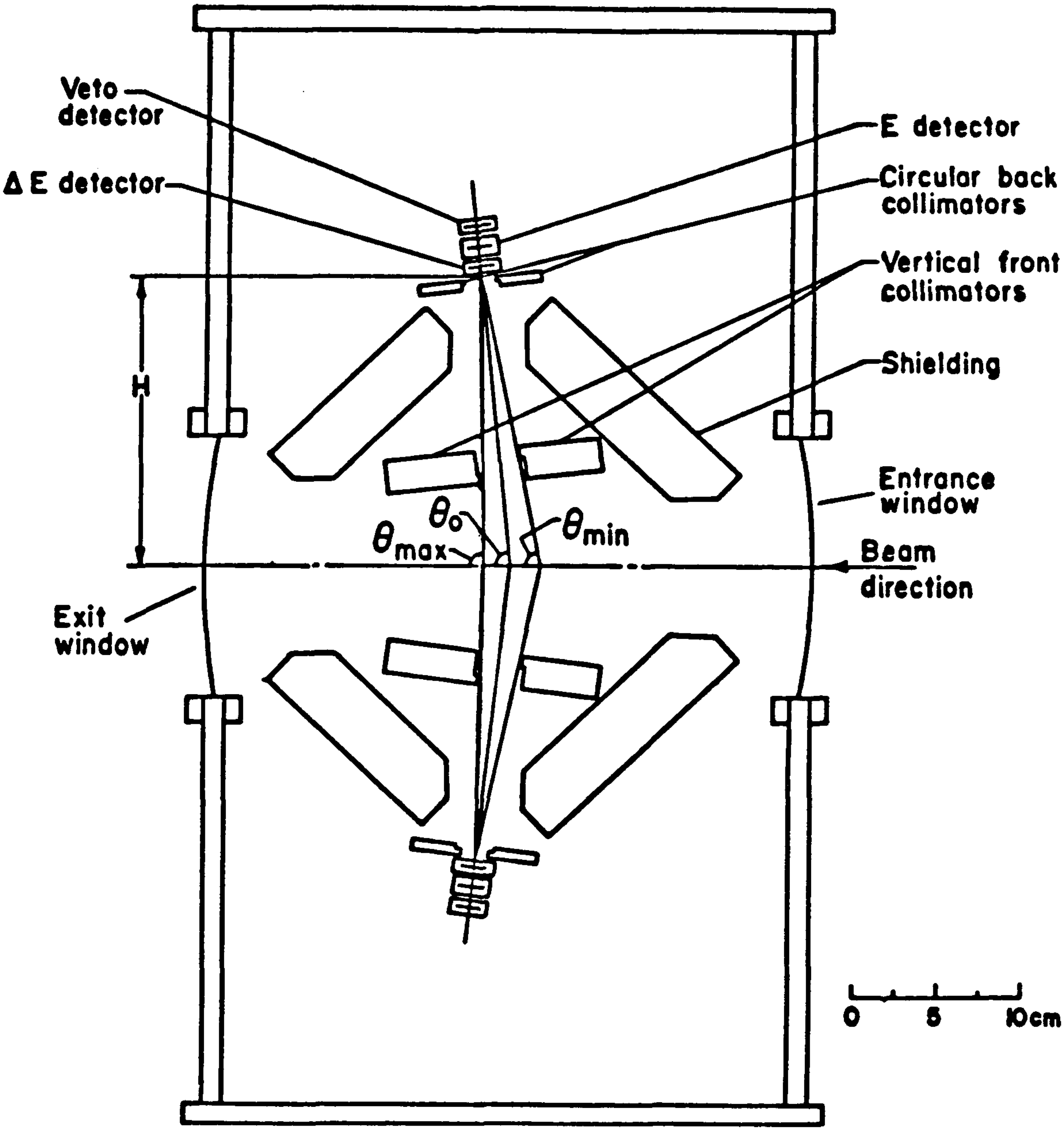

Fig. (3-2): The target chamber with collimation system and ΔE,E-VETO solid state detector telescope.

adjustable collimation system consisting of vertical brass slits 19 mm thick with a narrow 1 mm thick step to minimize slit scattering. These slits were fixed to allow recoil particles from the interaction region with scattering angles between θ_{min} and θ'_{max} through the circular back slit. The upstream front slit was adjusted so that θ_{min} was somewhat smaller than the angle at which the recoil particles from elastic scattering have sufficient energy to penetrate through the ΔE and E detectors of the detector telescope. The downstream front slit was adjusted so that θ_{max} was somewhat larger than the angle at which the recoil particles from elastic scattering have sufficient energy to penetrate through the ΔE detector and into the E detector. Note that the recoil energy decreases with increasing θ. In our discussion θ_o is defined as the angle between the center line of each telescope arm and the beam direction, and H is the perpendicular distance from the beam direction to a middle point in circular slit. Table (3-1) summarizes values of θ_o and H for the four different parts of this experiment.

As is shown in Fig. (3-2) four pieces of brass were placed in the scattering chamber to provide shielding for the solid state detectors from particles which were produced by interactions between the beam and the entrance and exit windows. Upstream of the chamber lead bricks of sufficient thickness to stop 800 MeV protons were placed around the beam pipe; and downstream some lead bricks were placed around the beam pipe.

In the second part of this experiment (time-of-flight) a system consisting of a thin brass tube which covered the path between the vertical front collimators and the circular back collimator along with two permanent magnets positioned at the left and right side of tube was added to the setup in order to reduce the background due to the fast electrons produced by beam gas target interactions.

Setup	θ_o^o	H cm
Time-of-flight	87.8	20.36
ΔE, E unpolarized	83.5	16.27
ΔE, E polarized	83.5	20.06
E, E polarized	79.00	19.82

Table (3-1) - Values of θ_o and H for different parts of experiment.

C. Solid State Detectors

A series of Ortec surface barrier detectors was used in this experiment. Under a special order these detectors were prepared by manufacturer for use in hydrogen atmospheres.

Tables (3-2) to (3-4) summarize the detector specifications in each arm for the different parts of the experiment.

Detector	Serial No.	Sensitive Depth μm
E_L	19-405E	49.9
$VETO_L$	17-503B	300
E_R	19-404A	95.8
$VETO_R$	17-503A	300

Table (3-2) - Detector specifications in each arm for time-of-flight setup.

Detector	Serial No.	Sensitive Depth μm
ΔE_L	19-405E	49.9
E_L	18-246D	1400
$VETO_L$	17-503B	300
ΔE_R	19-404A	95.8
E_R	18-246A	1400
$VETO_R$	17-503A	300

Table (3-3) - Detector specifications in each arm for ΔE,E setup.

Detector	Serial No.	Sensitive Depth μm
ΔE_L	18-246A	1400
E_L	18-246D	1400
$VETO_L$	17-503B	300

Table (3-4) - Detector specifications for E,E setup.

D. Gas Handling System

With the advise of Mr. J. Novak of the LAMPF Staff, a gas handling system was designed and built for this experiment which satisfied the stringent LAMPF safety requirements for hydrogen gas targets. Figure (3-3) shows this system. The vacuum integrity of the system permits pressures of less than 10^{-2} torr. Two Wallace and Tiernan pressure gauges with range of 0-800 mm Hg and 0-110 mm Hg were used in this system. They were calibrated against an MKS Baratron pressure transducer which had a system error of ±0.08%.

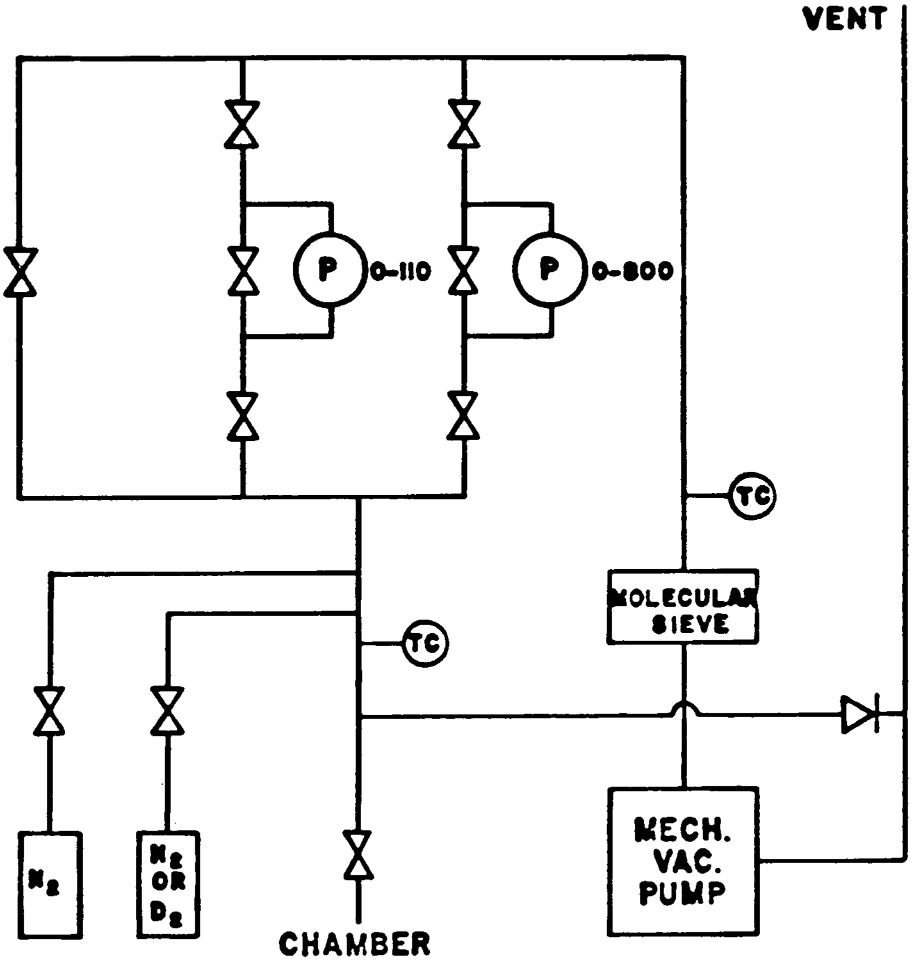

Fig. (3-3): Gas Handling System Schematic.

E. Electronics

Each of the Silicon detectors was biased (ΔE,E positive and VETO negative) with sufficient voltage to extend the depletion layer to the full thickness of the device. Thus the entire volume of the detector was sensitive to charged particles, providing an optimum detection efficiency. The signal from the detector was a current pulse with a total charge proportional to the energy deposited by the particle which had crossed the detector. Figure (3-4) shows a block diagram of electronics. A solid state preamplifier (Ortec 142) was located near the detector to minimize the capacitance of the connecting cable. The analog signals (energy and timing) from ΔE,E and VETO detector preamplifiers were fed directly to the counting house. The preamplifier energy signals corresponding to ΔE and E detectors were fed into an amplifying stage (Canberra 1413) and used for pulse-height measurements in a CAMAC ADC. The timing signal of each preamplifier (E, ΔE, VETO) was passed on for appropriate amplification (LRS 612). Amplifier outputs were passed through constant fraction discriminators (Ortec 934) and the resulting logic pulses for each arm were then fed into a coincidence unit (LRS 365AL) where the coincidence $\Delta E_L \cdot E_L \cdot \overline{\mathrm{VETO}_L}$ and $\Delta E_R \cdot E_R \ \overline{\mathrm{VETO}_R}$ (in the case of time-of-flight setup $E_L \cdot \overline{\mathrm{VETO}_L}$ and $E_R \cdot \overline{\mathrm{VETO}_R}$) were formed defining INTERRUPT signals for the right and left arm. As is shown in Fig. (4-3) when the INTERRUPT signal corresponding to either arm was in coincidence with the RUN signal provided by the computer (or in the case of the time-of-flight setup coincidence with the BEAM GATE signal) and in anti-coincidence with a computer busy signal, a STROBE signal was generated for that

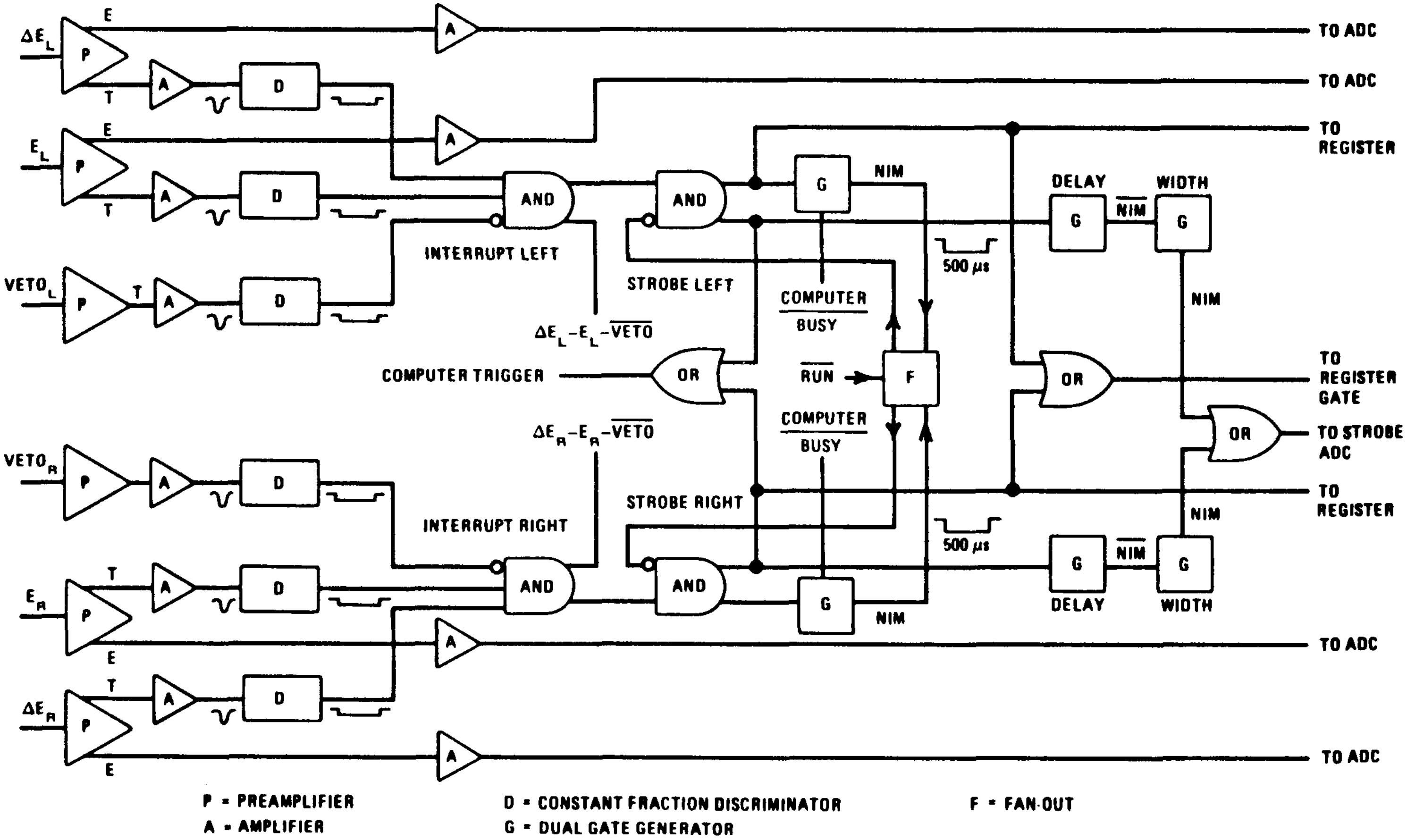

Fig. (3-4): Block Diagram of Electronics.

arm which was input to CAMAC register (LRS 2341). Left and right STROBE signals were fed into an inclusive OR gate and the output was used as a gate for the register and trigger for the computer. Also, after some pulse width and delay adjustment, the left and right STROBE signals were formed into gate signals for the ADC. The computer trigger allows the detector pulse height and time-of-flight information to be read into the computer for further processing. The CAMAC scalers, and various detectors and monitors were gated in several different ways. The following scaler gate/inhibit signals were generated:

RUN * BEAM * $\overline{\text{COMPUTER BUSY}}$ (for normal and reverse beam spin)

RUN * BEAM (for normal and reverse beam spin)

RUN (for normal and reverse beam spin).

These were made using the LAMPF Gate Generator which has the following facilities:

1. RUN and $\overline{\text{RUN}}$ flip-flop with TTL output.
2. TTL BEAM GATE output.
3. TTL-NIM, NIM-TTL, TTL-$\overline{\text{TTL}}$ converters.
4. TTL coincidences.

The ratio of the INTERRUPT (gated by RUN * BEAM) to STROBE (gated by RUN * BEAM) is the computer live time, a measure of the event taking rate capabilities of the system.

F. Data Acquisition System

The CAMAC modules are linked to a PDP-11/45 computer through an MBD—micro programmed branch driver. The MBD controls the CAMAC branch and performs data transfer to the PDP11 memory by the LAMPF data acquisition program "Q". When a STROBE signal is sent to the MBD, approximately 40 data words associated with an event are read from the CAMAC into a 800 word software buffer. When this buffer is filled it is written out onto the 7-track, 800 bpi (byte per inch) magnetic type drive. When the computer is not busy with these transfers, some of the events are processed by a program called "the event processer" in conjunction with a "TEST FILE". For example, from the raw detector pulse height and time of flight data the "event processor" calculated the actual energy losses in MeV for the individual ΔE and E detectors, the total energy $\Delta E + E$ in MeV, the particle mass for a given $\Delta E \cdot E \cdot \overline{\text{VETO}}$ coincidence, and the actual time of flight in ns from the interaction volume to the detector.

The "TEST FILE" performs a set of logical tests on each event. These tests are of two types: "Micro-Tests" and "Macro-Tests." "Micro-Tests" are applied directly to raw or computed quantities. They can be cuts, boxes, or bit tests. "Macro-Tests" are logical "AND" or "OR" combinations of "Micro-Tests" or previous "Macro-Tests".

Raw or computed quantities from the processor may be displayed on line by a display package, either as a histogram or as a dot plot on the graphic display terminals.

G. EPB Polarimeter

In order to obtain the analyzing power, A_y, from the experimentally observed asymmetry, ε, it is necessary to know the beam polarization.

$$\varepsilon = AP_B \quad . \tag{3-1}$$

The EPB polarimeter is a secondary standard of known analyzing power. A typical experiment measures the asymmetry for the reaction of interest relative to the asymmetry of the polarimeter. The polarimeter setup is shown in Fig. (3-5). The reaction chosen for the EPB polarimeter is pp → pp elastic scattering. Primary and conjugate protons in coincidence elastically scattered from the hydrogen in a CH_2 target are detected near the laboratory angles of 17° and 66.4°, respectively, in each of four directions, left, right, up, and down, by four pairs of scintillation detectors. The left-right detectors measure the vertical (y) component of beam polarization, while the up and down detectors monitor the horizontal-transverse (x)component. Coincident events detected in this way are not only from the reaction pp → pp but also from C(p,2p) (quasi-free scattering) (McNaughton 80). Taking into consideration these quasi elastic coincidences the EPB polarimeter gives a calibrated total analyzing power $A_y = 0.481 \pm 0.002$ at 796 MeV (McNaughton 80). For accurate work with this polarimeter random coincidences are measured in each direction by 20 ns delayed coincidences. When the true real coincidences are calculated from

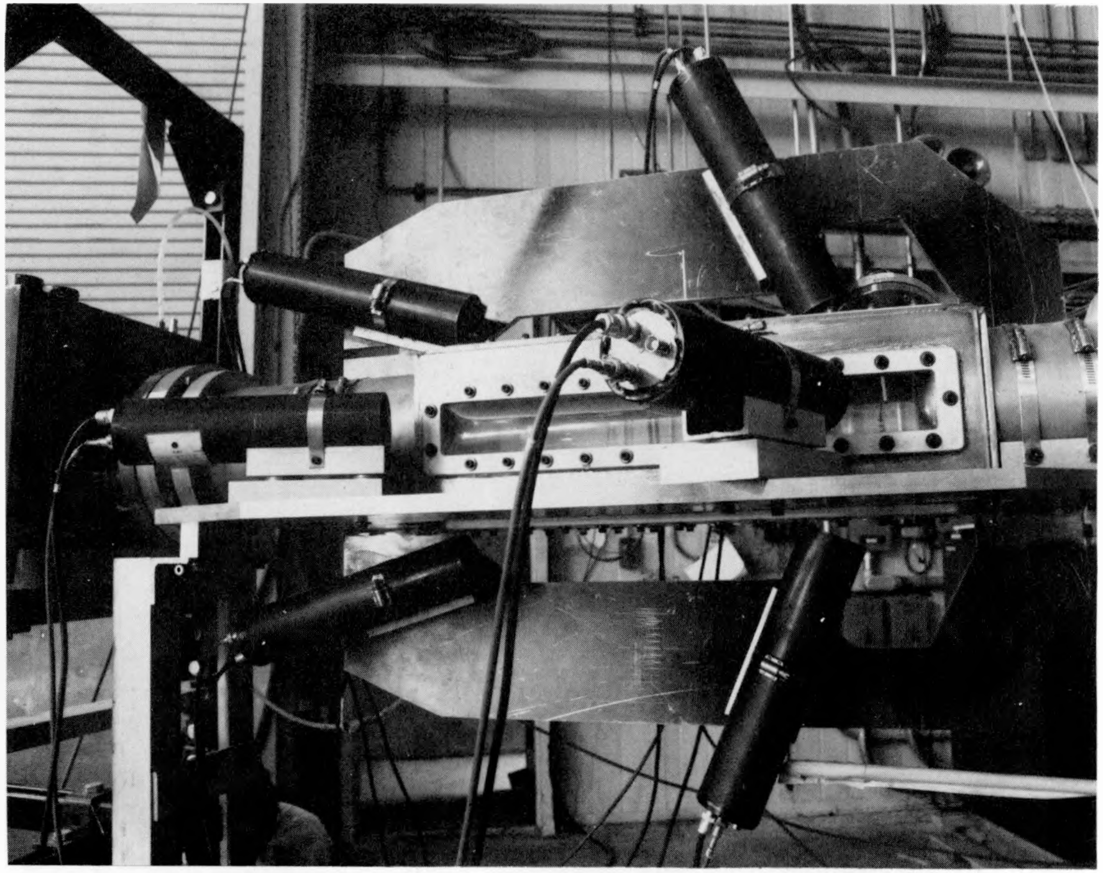

Fig. (3-5): EPB Polarimeter Setup.

subtraction of these random coincidences the EPB polarimeter readings are reproducible to better than 0.5%.

The electronics setup for the polarimeter consists of high voltage power supplies for the phototubes, discriminators for the anode signals, and fast coincidence units. Each coincidence (L, R, U, D) is scaled in two CAMAC scalers, one gated for "normal" beam spin (N), the other for "reverse" (R).

Using formula (3-1) and the known analyzing power for the polarimeter, A_y, the beam polarization, P_B may be determined by measuring the experimental left-right asymmetry ε which is defined as

$$\varepsilon = \frac{L - R}{L + R} \tag{3-2}$$

where L is the geometrical mean of events that scatter left (the coincidence of 17° left and 66.4° right is known by convention as "left") when the beam polarization is up, $L\uparrow$, and right when the beam polarization is down, $R\downarrow$, $L = \sqrt{L\uparrow R\downarrow}$; similarly $R = \sqrt{R\uparrow L\downarrow}$. It is well known that use of this technique cancels instrumental asymmetries to a high order (Ohlsen 73).

H. EPB Faraday Cup (Barrett 75)

Figure (3-6) shows the general design of the EPB Faraday Cup. The EPB beam which has low emittance (<1mr-cm) and energy spread (±3.5 MeV) is virtually free of contamination from other charged particles. This beam enters the main body of the Faraday Cup and is stopped by 45 cm of lead (the range of 800 MeV protons in lead is 39 cm). The

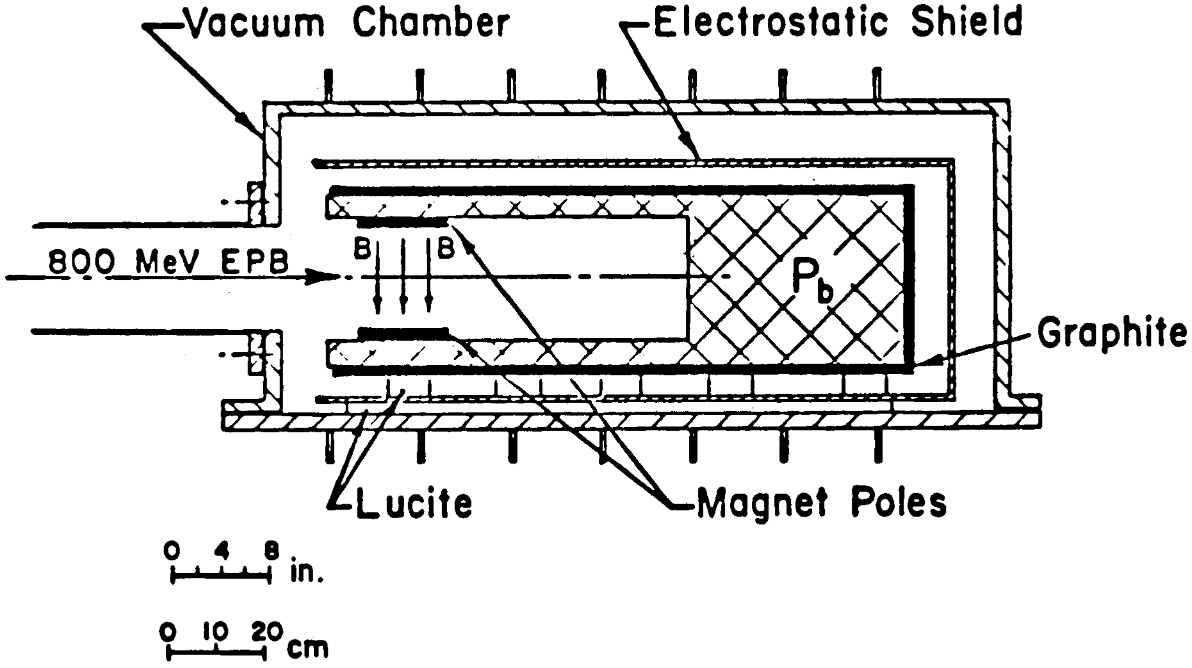

Fig. (3-6): Design of the EPB Faraday Cup.

re-entrant tube has an outside diameter of 35 cm, an inside diameter 25 cm, and a length of 75 cm. The total length of the Cup is 120 cm including the beam stop.

The probability for a 800 MeV proton stopping without undergoing an nuclear inelastic collision is only 11% (Janni 66) so that secondary protons must be considered, particularly those produced by (n,p) reactions near the surface of the lead and then lost from the Cup. A 1.25 cm thick graphite shell surrounds the lead to reduce this effect by virtue of the much smaller $^{12}C(n,p)$ cross section.

The 75 cm long re-entrant cavity was designed to capture secondary emission electrons produced when the beam strikes the inner surface of the lead cup. At 800 MeV the secondary emission efficiency is about 2.5%; thus, since the cavity is 85% enclosed, at most 0.4% of the proton beam current could be lost through secondary electron emission. In order to reduce this effect still further a small magnet produces a field of ~15 Gauss across the entrance port. Overall, the total electron loss is estimated to be less than 0.1%.

A 50 cm diameter, 0.32 thick stainless steel electrostatic shield surrounds the Cup, as shown in Fig. (3-6), with lucite standoff insulators isolating the Cup from the shield. The Cup and the shield have separate electrical output leads through the other vacuum vessel. The entire assembly was connected directly to the accelerator vacuum system, maintained at a pressure of the order of 10^{-6} torr. This vacuum level reduced the possibility of the positive ions being produced by radiation in the gas surrounding the Faraday Cup to essentially zero.

The charge collected by the Faraday Cup was fed through ~40 m long, coaxial cables to an Ortec 439 charge digitizer. Charge leakage due to insufficient impedance to ground may occur in either the Faraday Cup, the cables, or the associated electronics. Leakage current has been found to be less than 1 PA Dark current can also be induced through pickup from the RF fields associated with the accelerator. The ground shield and an RF filter at the input to the digitizer kept dark currents generally below 1 PA level

The EPB Faraday Cup has been calibrated and tested by different methods. These results indicate that the absolute calibration of the Faraday Cup has a maximum uncertainty of less than ±1%.

CHAPTER IV

EXPERIMENTAL METHOD

In this chapter we will discuss some theoretical consideratins underlying the experimental techniques used in this experiment.

A. Reaction Considerations

For small angle elastic scattering in a process like

$$P + X \rightarrow P + X \quad . \tag{4-1}$$

X has a laboratory angle near 90°; more exactly, θ_X approaches 90° as θ_p approaches zero degrees. If X has no excited states which are bound against particle emission, then in the inelastic scattering processes like $P + X \rightarrow P + X^*$, X^* will decay to $X^* \rightarrow A + B$ soon after its formation. Thus in inelastic scattering, in order to have X in final state we must produce another particle, y; $P + X \rightarrow P + Y + X$. However, from the kinematic relations for this type of reaction, there is a upper limit for the scattering angle, θ', for a particle of type X: $\theta'_{max} < 90^\circ$. Figures (4-1) and (4-2) make this discussion clear for the p + p and the p + d reactions respectively. Recoil particles with a scattering angle, θ, $\theta'_{max} < \theta < 90^\circ$, must come from an elastic event. The maximum angles, θ'_{max} for the recoil particles with inelastic particle production in the p-p and the p-d reactions at 800 MeV are 53.6° and 60.5° respectively. As was discussed in Chapter III, the interaction region in the scattering chamber is defined by a two slit collimation system. By adjusting the vertical front slits we can define an angular acceptance from θ_{min} to θ_{max} for recoil particle trajectories from the interaction region through the circular back slit [see Fig. (3-2)]. As discussed in Chapter III, the values of θ_{min}, θ_o and θ_{max} were chosen to match the characteristics of the particular particle telescope being used in a given part of the experiment.

B. Geometrical Considerations

With the experimental setup explained in Chapter III we are able to measure the yield per kinetic energy interval, dY/dT , for the recoil particles which stop in the solid state detector telescope. For the given geometry in this experiment Whitten (Whitten 75) has shown that the elastic differential cross section in the laboratory system, $d\sigma/d\Omega\ (\theta_x)$ for the process $P + X \rightarrow P + X$ is:

$$\frac{d\sigma}{d\Omega_x}(\theta_x) = \frac{(dY/dT_x)(dT_x/d\theta_x)}{nN\sin\theta_x A(\theta_x)} \qquad (4\text{-}2)$$

where T_x is the laboratory energy of the recoil particle. N is number of beam particles, and n is the number of target nuclei per unit volume in the target gas. The term $A(\theta_x)$ is a geometrical factor (dimension length) which depends on the geometrical specifications of the experiment.

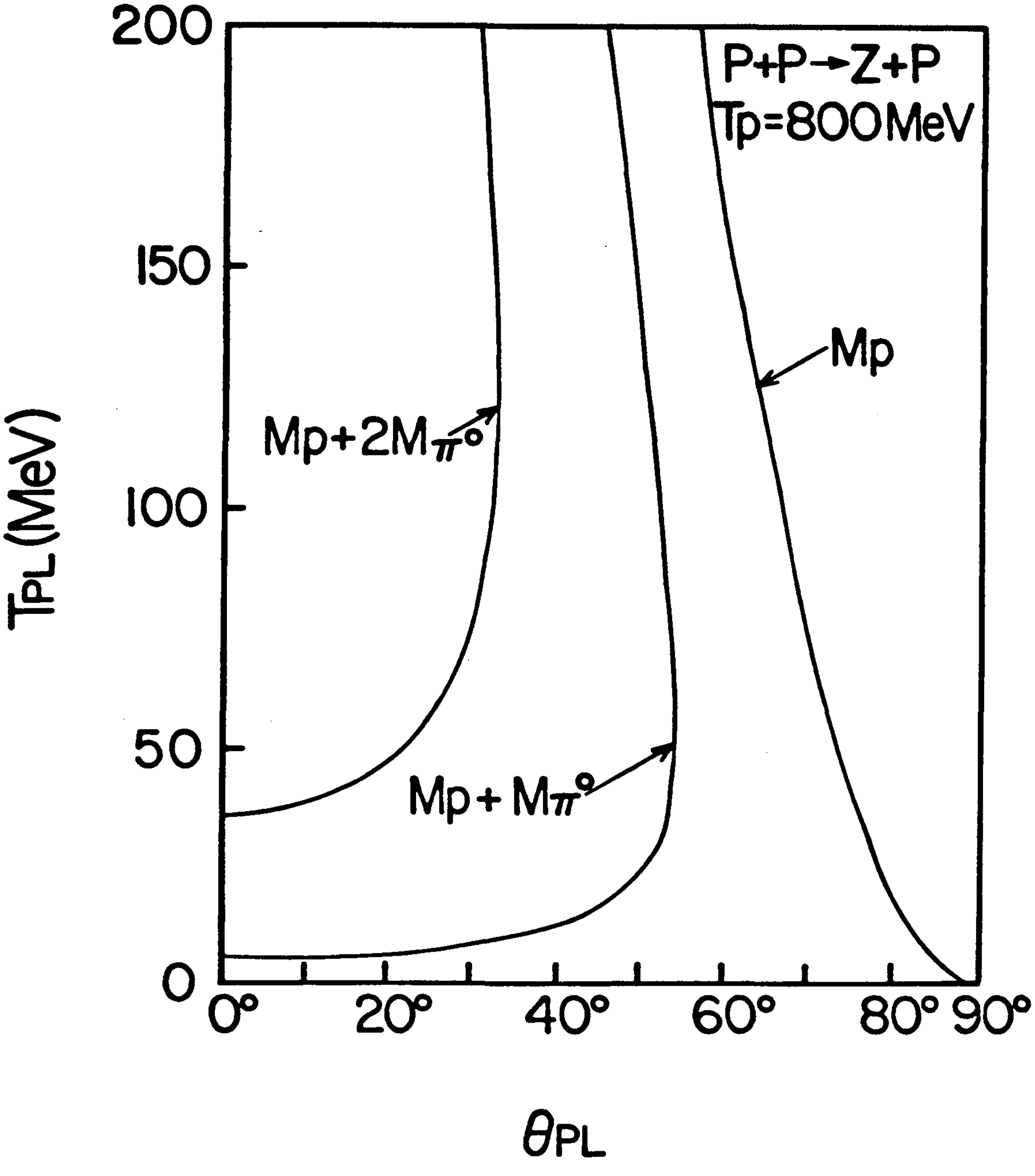

Fig. (4-1): Kinematic relation between T_{PL} and θ_{PL} for the reaction $p + p \rightarrow z + p$, where the incident protons have a kinetic energy of 800 MeV. The curves represent various choices for M_z, the invariant mass of z. For elastic events $M_z = M_p$ and for inelastic events $M_z > M_p + M_{\pi^0}$.

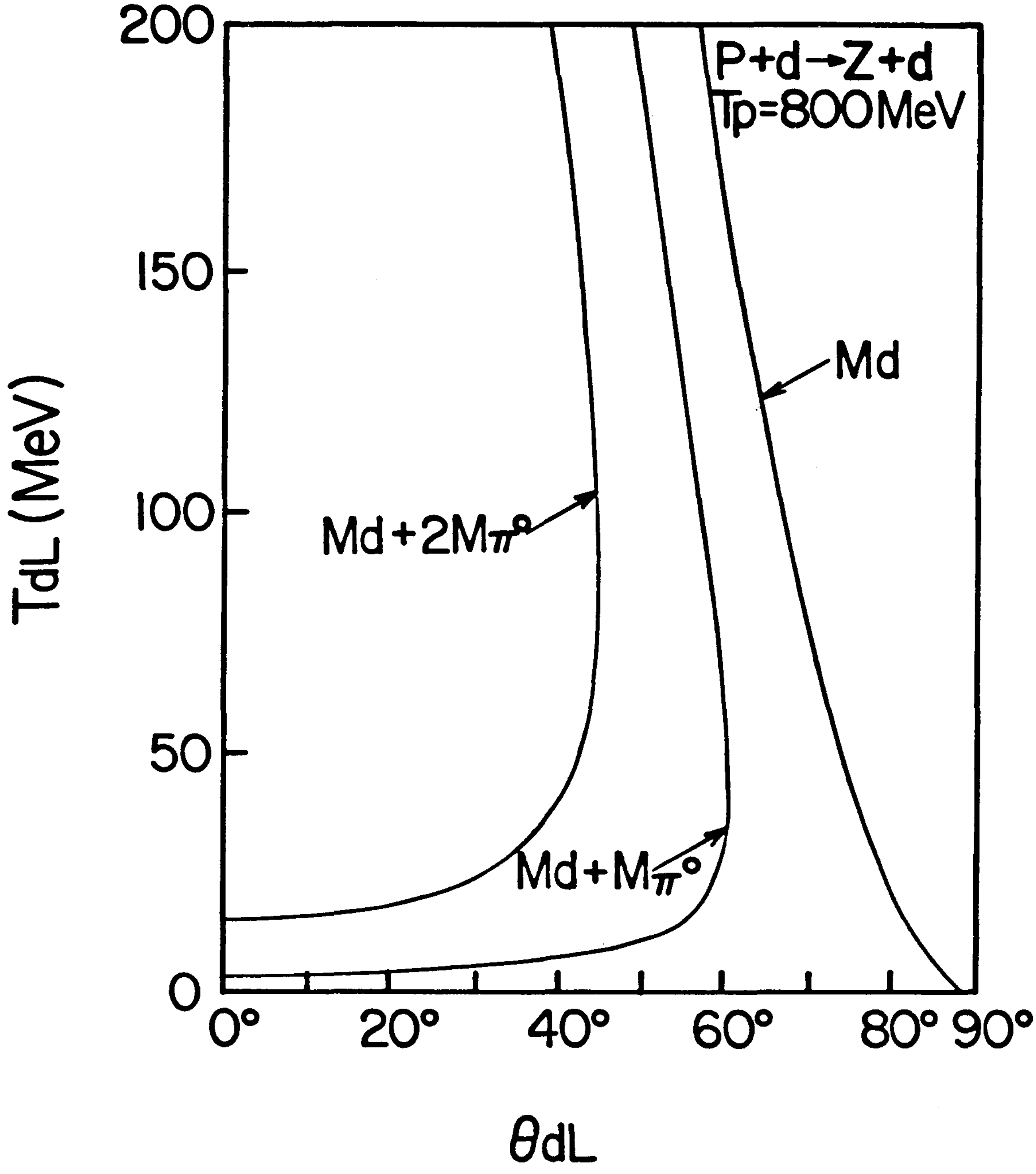

Fig. (4-2): Kinematic relation between T_{dL} and θ_{dL} for reaction $p + d \rightarrow z + p$, where the incident protons have a kinetic energy of 800 MeV. Here z represents everything in the exit channel other than the deuteron particle. Each curve represents a choice for M_z, the invariant mass of z. For elastic events $M_z = M_d$ and for inelastic events $M_z > M + M_{\pi^o}$.

For our geometry Whitten (Whitten 75) has shown that to very good accuracy

$$A(\theta_x) = \frac{A}{H} \left[\frac{\cos(\theta_x - \theta_o)}{\sin\theta_x}\right] \tag{4-3}$$

where H>> dimensions of beam and H>> dimensions of back collimator. Here A is the area of the circular back slit, and H and θ_o are defined in Chapter III [see Fig. (3-2)].

C. Kinematic Calculations

Equation (4-2) expresses the differential cross section for elastic scattering in terms of the laboratory angle of the recoil particle. In this section, following the discussion by Whitten (Whitten 75), we will transform Eq. (4-2) to express the differential cross section in terms of the four momentum transfer squared -t; that is;

$$\frac{d\sigma}{dt}(t) \quad .$$

We may write

$$-t = q^2 = 2MT_{lab} \tag{4-4}$$

$$\frac{d\sigma(t)}{dt} = \frac{d\sigma(\theta_x)}{d\Omega_{lab}} \frac{d\Omega_{lab}}{dt} \quad . \tag{4-5}$$

Using Eq. (4-2) in (4-5) gives

$$\frac{d\sigma(t)}{dt} = \frac{dY/dT_x}{nNs\text{in}\theta_{lab}A(\theta_{lab})} \frac{dT_x}{d\theta_{lab}} \frac{d\Omega_{lab}}{dt} \tag{4-6}$$

where all quantities correspond to the recoil particle. But:

$$\left(\frac{dT_x}{d\theta_{lab}}\right) \left(\frac{d\Omega_{lab}}{dt}\right) = 2\pi \sin\theta_{lab} \frac{dT_{x_{lab}}}{dt} \quad .$$

Using (4-4) we obtain:

$$\left(\frac{dT}{d\theta}\right)_{lab} \left(\frac{d\Omega}{dt}\right)_{lab} = \left(\frac{\pi}{M}\right) \sin\theta_{lab} \tag{4-7}$$

which substitution of (4-7) into (4-6) gives

$$\frac{d\sigma(t)}{dt} = \left(\frac{dY}{dT_x}\right) \left[\frac{\pi}{M}\right] \left[\frac{1}{nNA(\theta_{x_{lab}})}\right] \quad . \tag{4-8}$$

The value of $\theta_{x_{lab}}$ for the recoil particle can be obtained from the kinetic energy of the recoil particle, T_x, using the kinematic relation:

$$\cos\theta_{x_{lab}} = \frac{(E_o + P_o)T_x^{1/2}}{P_o(T_x + 2M)^{1/2}} \tag{4-9}$$

where E_o and P_o are the initial total energy and momentum of the incident projectile (in our case a proton) in the laboratory frame, and M is the rest mass for the recoil particle.

D. Method of Particle Identification

1. ΔE,E Setup

For the ΔE-E-VETO detector telescope which looked at events corresponding to $\Delta E \cdot E \cdot \overline{\text{VETO}}$ coincidences, we measured the energy losses in the ΔE and E detectors for particle stopping in the E detector. Figure (4-3) shows a two-dimensional raw dot plot of energy loss of particle in the passing detector (ΔE) vs. $E_T = E + \Delta E$ where E is the energy deposited in E detector. Thus we have an energy spectrum for each particle type (proton or deuteron) within some energy range. This method of particle identification has some problems, since it uses a very large two-dimensional space in the co-ordinates ΔE and E_T.

In order to be able to derive a particle identification which is independent of the kinetic energy of the particle, we use the fact that the range of a charged particle in the matter over a wide energy region has a relationship of the form:

$$R = aE^b + c \tag{4-10}$$

where a, b, and c are constants.

The exponent b is a constant and for a very large dynamic range in both energy and particle type it lies between the limits 1.65 and 1.74 (Skyrme 67). The constant a depends on the mass and charge of the particle and it is approximately inversely proportional to MZ^2. Now the passing detector (ΔE) has a thickness T, and this thickness is equal to the difference in the ranges of particles with energies E_T and E. This is summarized by the equation

$$T = R(E_T) - R(E) = a(E_T)^b - a(E)^b \quad . \tag{4-11}$$

When this relation is rearranged and the approximate dependence of a on MZ^2 is written into it, a particle identification function in terms of mass M and atomic number Z is obtained:

$$TMZ^2 \propto (E_T)^b - (E)^b$$

or

$$MZ^2 \propto (E + \Delta E)^b - (E)^b \quad . \tag{4-12}$$

This particle identification function was used with the on-line computer. Figure (4-4) shows a two dimensional raw dot plot of mass M vs. total energy, E_T, for $Z = 1$ particles in the detector telescope corresponding to the interaction of 800 MeV protons with the deuterium gas. Figure (4-5) shows a typical mass spectrum [projection of Fig. (4-4) onto the M axis] with peaks corresponding to proton and deuteron. Software gates could be put on the mass region of interest (proton or deuteron) and we could then look at the total energy spectrum, $E_T = \Delta E + E$, constrained by this mass cut.

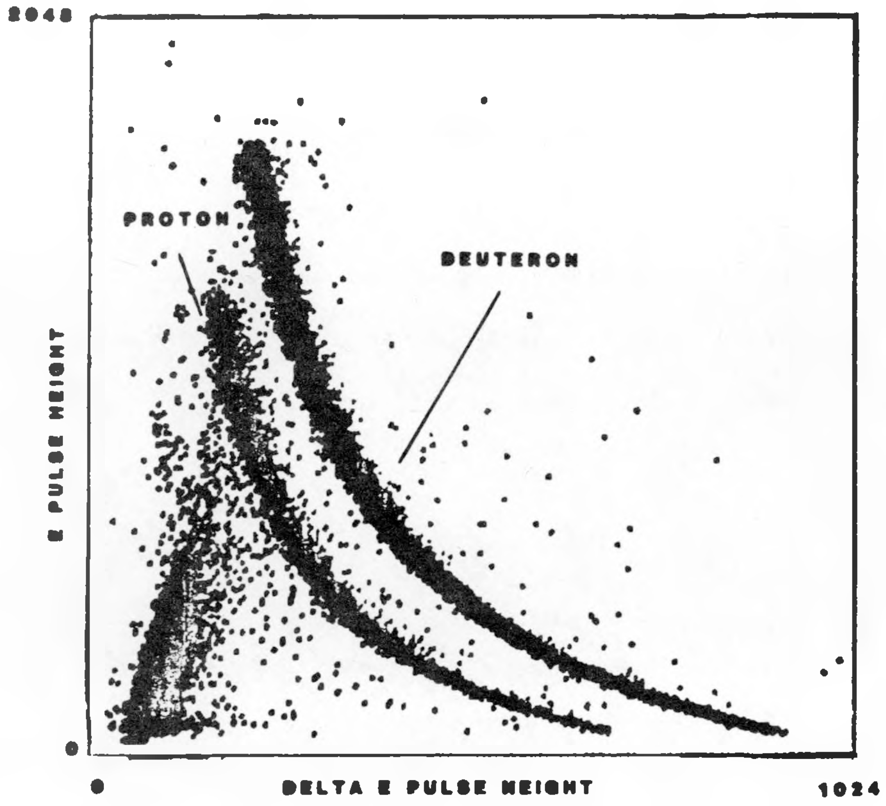

Fig. (4-3): A typical two-dimensional dot plot of energy loss of particle in ΔE detector vs the energy deposited in E detector for the interaction of 800 MeV protons with the deuterium gas in ΔE,E setup.

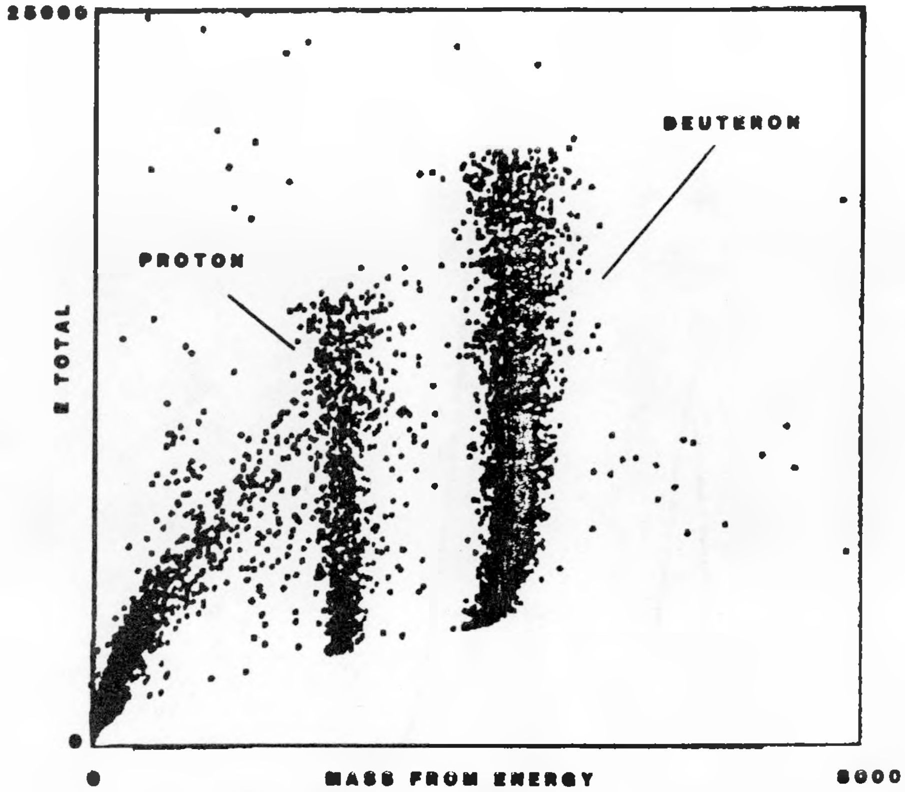

Fig. (4-4): A typical two-dimensional dot plot of mass M vs total energy deposited in detector telescope for the interaction of 800 MeV protons with the deuterium gas in ΔE,E setup.

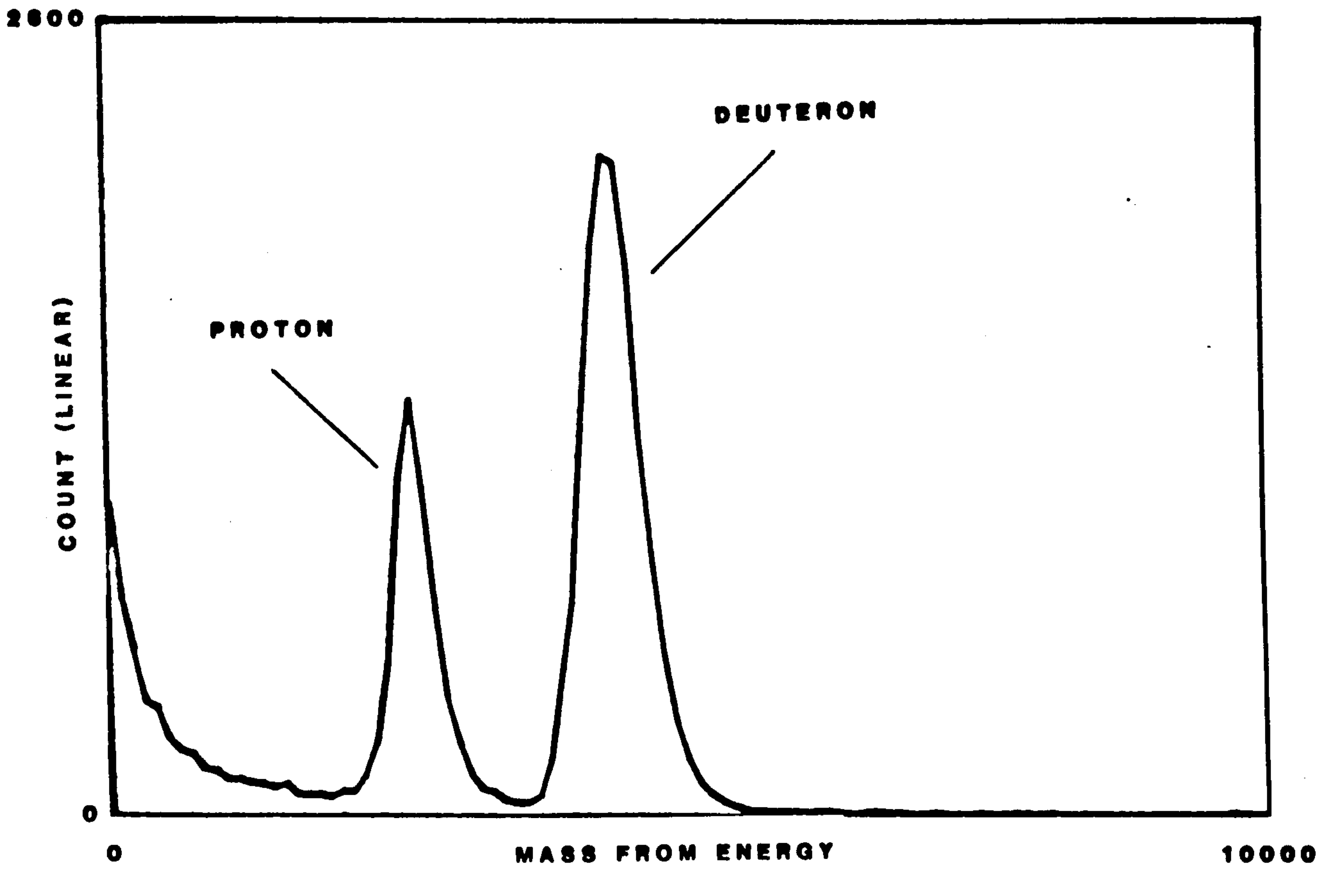

Fig. (4-5): A typical mass spectrum with peaks corresponding to proton and deuteron in ΔE,E setup.

2. Time-of-Flight Setup

In this arrangement an E-VETO detector telescope was used (actually the ΔE detectors from the previous ΔE-E telescope were used as the E detector here) and we looked at events which stopped in the E detector ($E \cdot \overline{VETO}$ coincidences). The energy of the stopped particle and its time of flight, assuming a trajectory from the interaction region to the E detector were measured. Now from the measurement of the energy in the E detector and from the time of flight measurement, a particle mass identification can be determined. It is clear that the time of flight, t, is proportional to v^{-1}, where v is the particle velocity. For non-relativistic velocities which we are dealing with, $E \lesssim 4$ MeV, the product Et^2 is independent of energy and dependent only on the mass of the particle, M, ($E = 1/2\ Mv^2$) and thus can be used as a particle identification function. The pulse in the E detector provided a start signal for the time of flight measurement while the stop signal was provided by a standard LAMPF unit which gave an output signal which was synchronized with the 40 ns chopped proton beam. Figure (4-6) shows a raw dot plot of time of flight vs. E. The line in this dot plot corresponds to protons. Figure (4-7) shows a mass, M, vs. energy, E, dot plot, while Fig. (4-8) shows a projection of Fig. (4-7) onto the mass M axis.

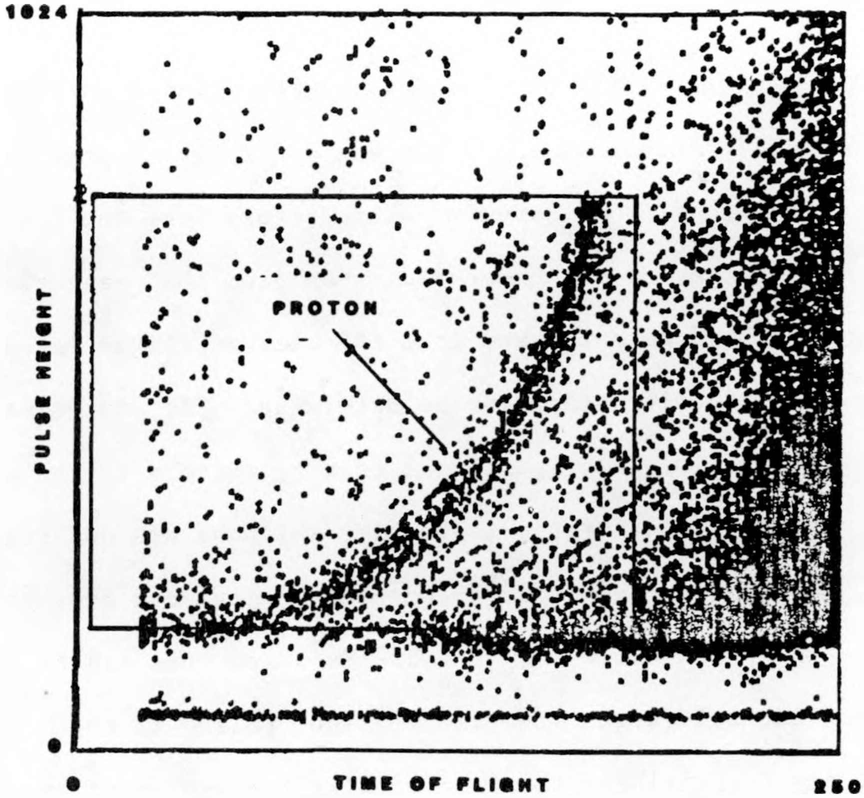

Fig. (4-6): A typical two-dimensional dot plot of time-of-flight vs energy deposited in E detector for the interaction of 800 MeV protons with the hydrogen gas in time-of-flight setup.

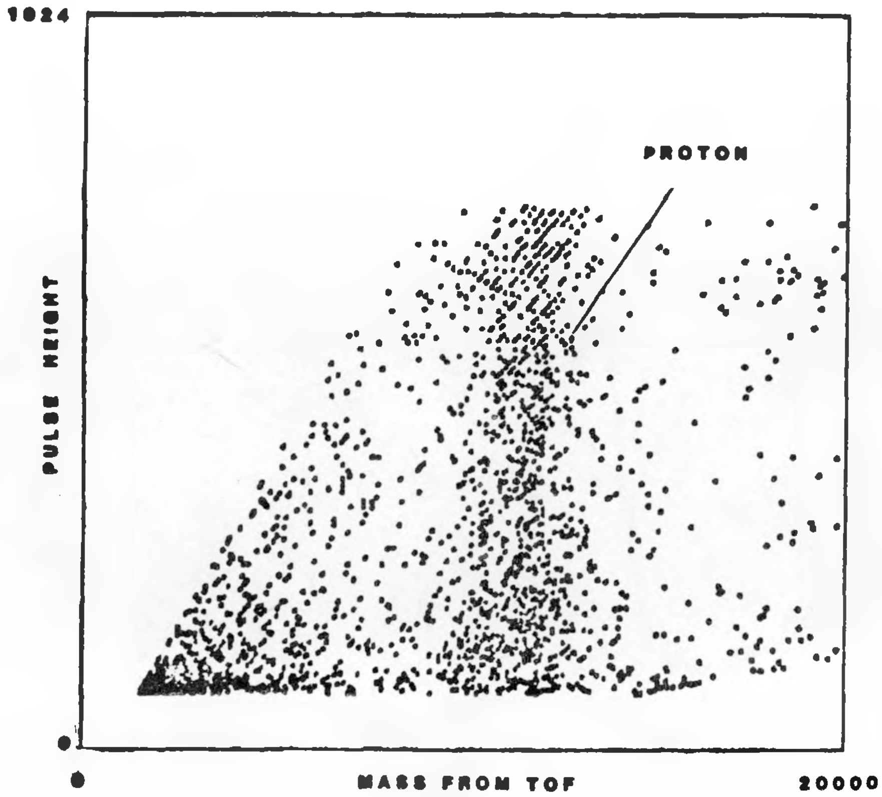

Fig. (4-7): A typical two-dimensional dot plot of mass M vs energy deposited in E detector for the interaction of 800 MeV protons with the hydrogen gas in time-of-flight setup.

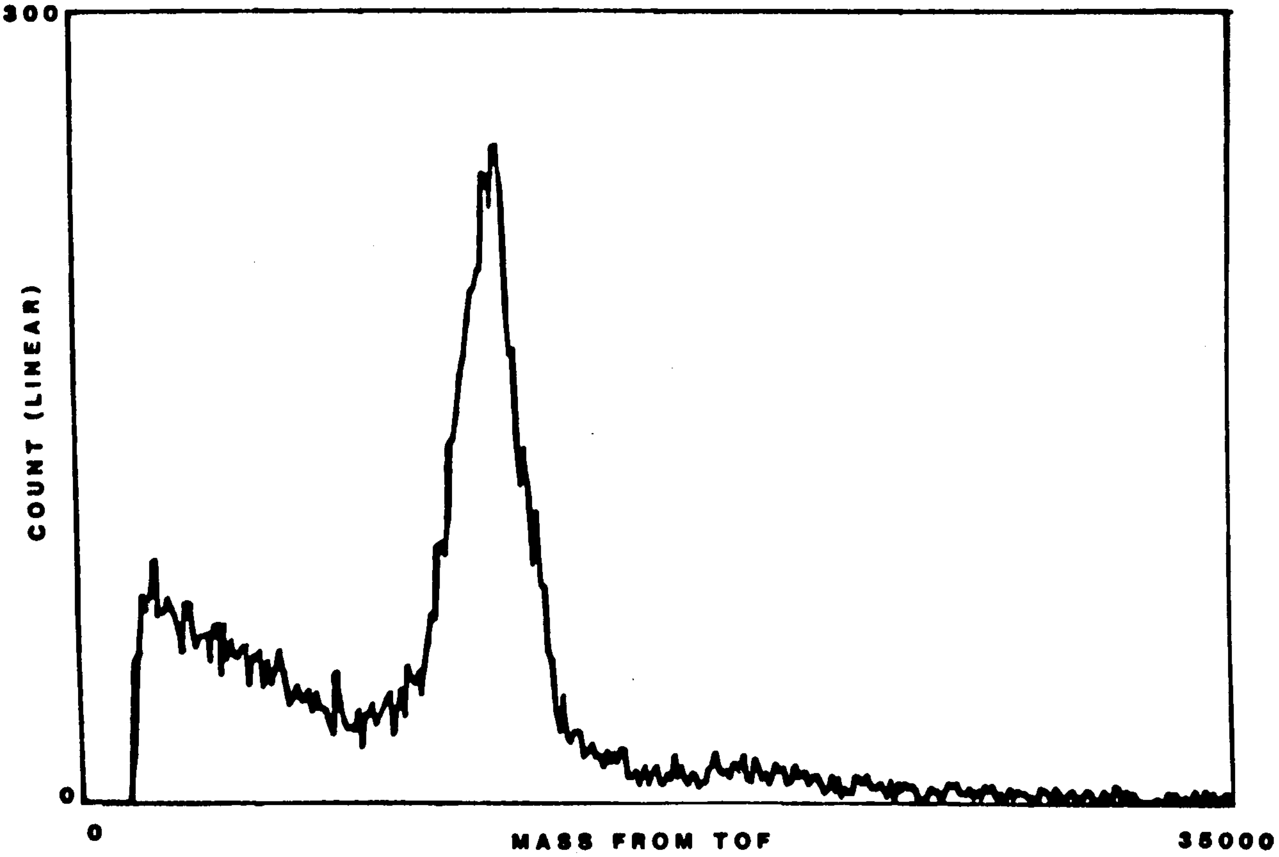

Fig. (4-8): A typical mass spectrum with peak corresponding to proton in time- of-flight setup.

CHAPTER V

DATA REDUCTION

In this chapter we will discuss the analysis of the raw data to obtain differential cross sections and analyzing powers for p-p and p-d elastic scattering at 800 MeV. After discussing the method of data reduction, we will present the resultant data.

A. Detector Calibration

The energy calibration of each solid state detector and its respective ADC was accomplished by the use of an alpha source. The alpha source was nominally ^{242}Cm, but it was found to contain alpha's from the decay of ^{242}Cm, ^{238}Pu, and ^{250}Cf. The relevant alpha decay schemes are presented in Fig. (5-1) while a typical alpha spectrum is presented in Fig. (5-2). As is shown in Fig. (5-2) the strong peaks in the alpha spectra are the 6113 and 5499 keV lines from the alpha decay of ^{242}Cm and ^{238}Pu respectively; and these two peaks were used to determine an energy scale for each ADC. A linear relation between ADC channel number and energy deposited in the detector, E_D, was assumed: $E_D = a \cdot C + b$; and the linearity of the ADC's was checked with the use of a calibrated pulser. A small correction to the alpha energy deposited in the sensitive region of the detector due to a thin dead layer, D, (20 μg/cm^2 Ni) on the front of the detector was made:

$$E_D = E_\alpha - D \frac{dE}{d\xi} \Big|_{E_\alpha} \quad . \tag{5-1}$$

This correction was 8 keV. Calibrations of each detector-ADC system were taken at various times during the total running period of this experiment. Comparisons of these calibration data would indicate that the ΔT bins are determined to an accuracy of ±0.5%. Also, for the detectors used in the time of flight measurement the absolute energy loss in the detector is determined to ±25 keV at 1 MeV and ±15 keV at 3 MeV.

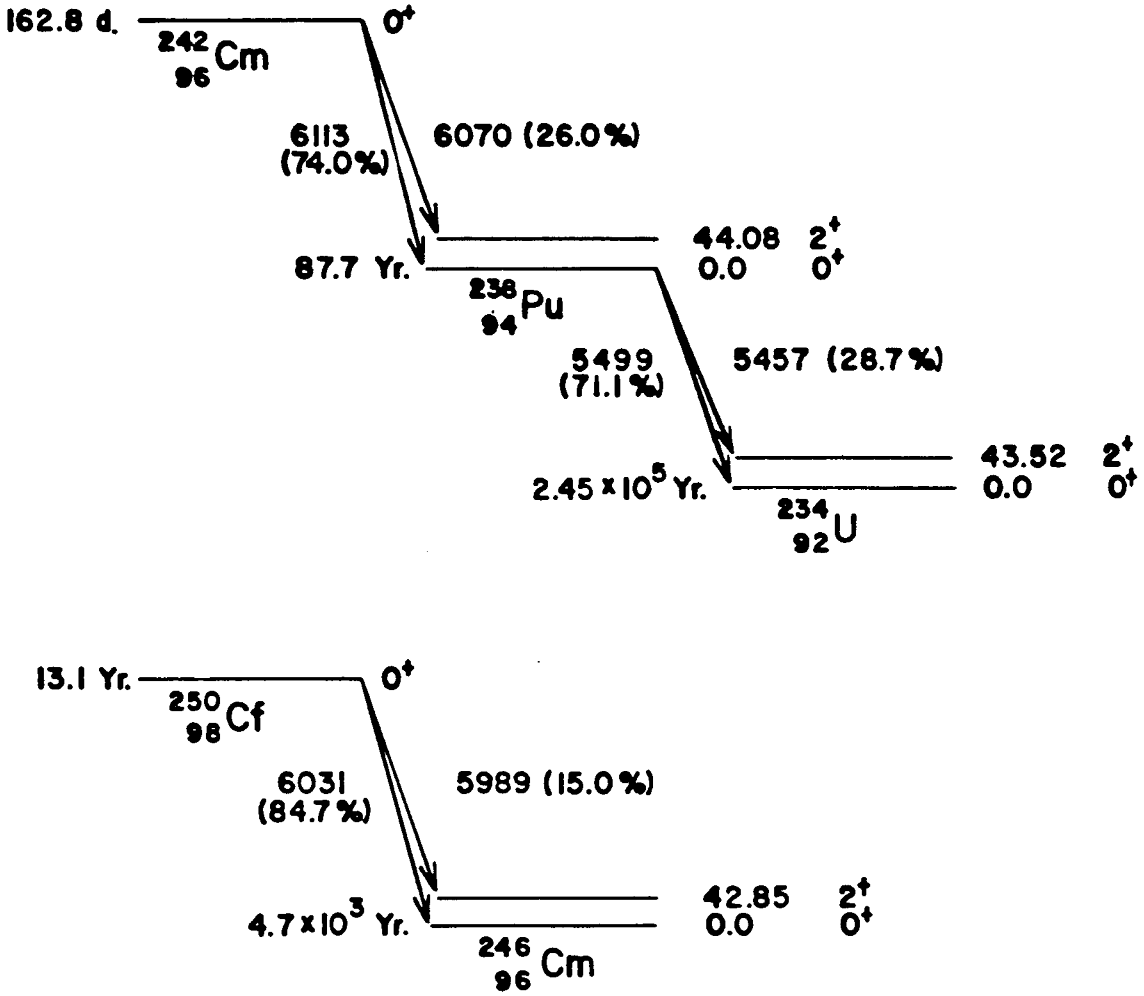

Fig. (5-1): Alpha Decay Schemes.

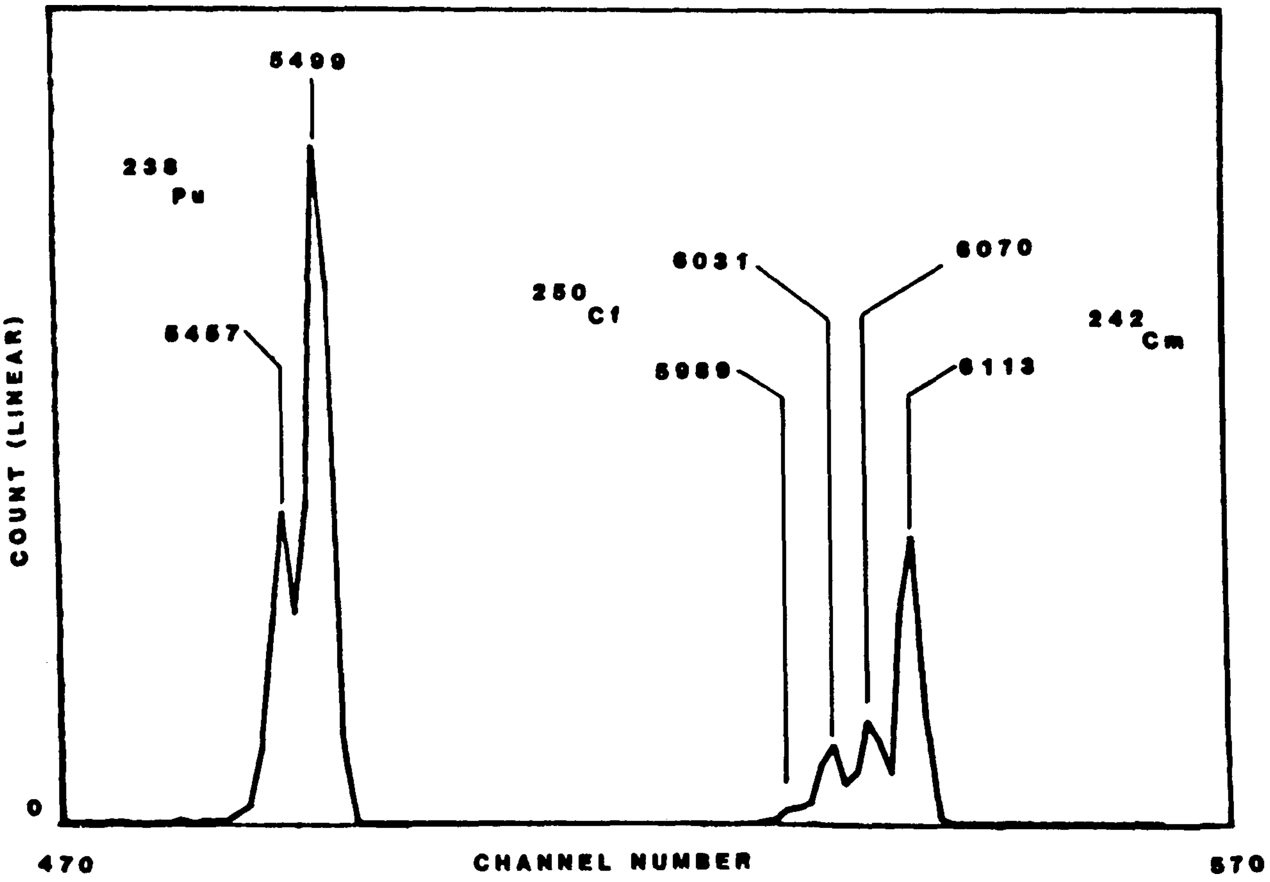

Fig. (5-2): A Typical Alpha Spectrum.

B. Replay

The first step in the data processing was to replay the data tapes imposing criteria for good events. Gates were set around the recoil particle of interest in the mass spectra corresponding to each arm. A typical mass spectra with gate on the proton peak is shown in (4-5). For the ΔE,E setup a good event for each arm is an event which satisfies the mass gate and electronic INTERRUPT corresponding to that arm. For the time of flight data a good event must also satisfy a box positioned around recoil protons in a two dimensional raw dot-plot of time of flight vs. E detector pulse height [Fig. (4-6)]. Figure (4-8) shows a mass spectrum for the time of flight data.

The energy resolution of the surface barrier detectors was about 50 keV, and we therefore binned the energy spectra in 100-keV bins. The recoil particle energy spectra resulting from replay were used for the extraction of cross sections and analyzing powers. Figures (5-3) and (5-4) show a typical recoil proton energy spectra and recoil deuteron energy spectra, respectively in the ΔE,E detector setup obtained from one data run. Figure (5-5) is a typical recoil proton energy spectra for the time of flight setup.

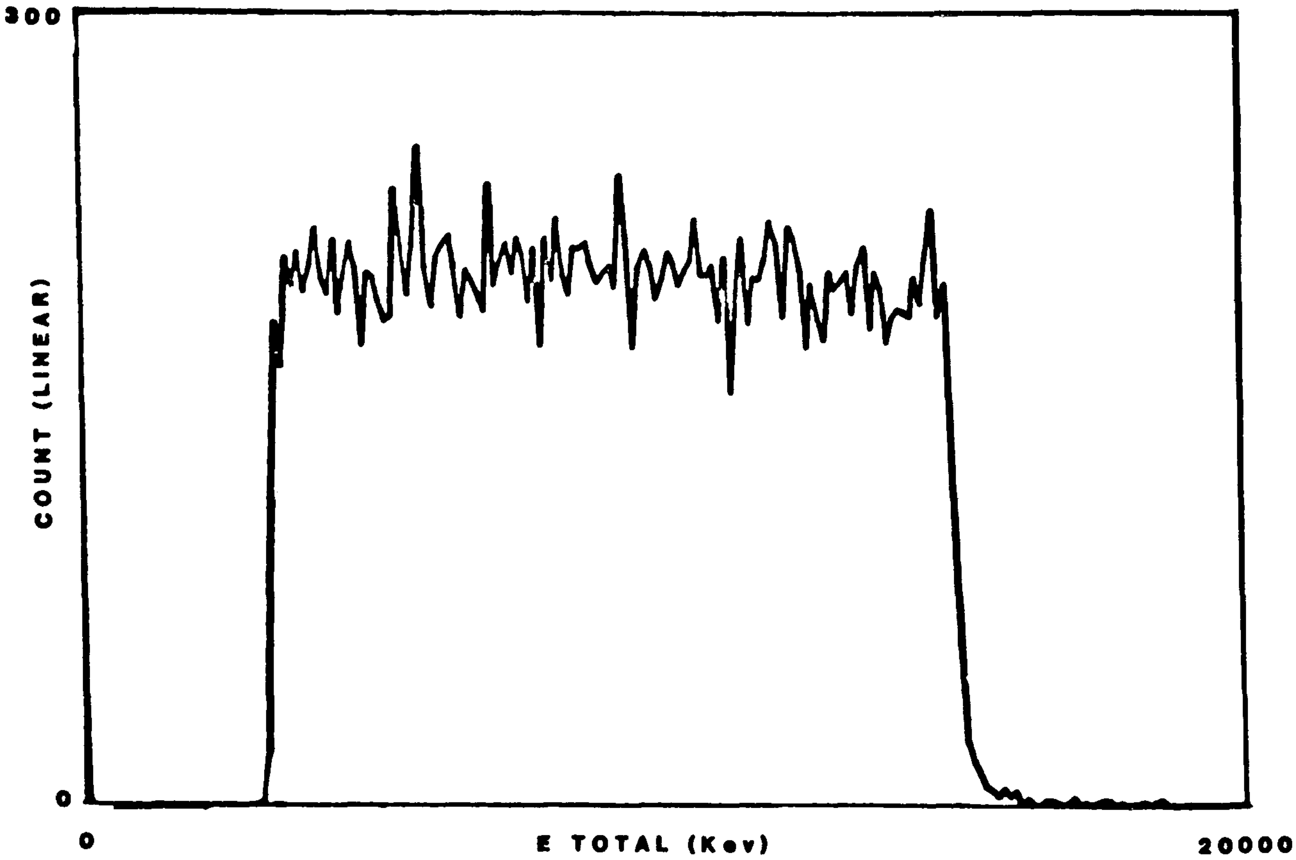

Fig. (5-3): A typical energy spectrum of recoil protons for interaction of 800 MeV protons with hydrogen gas in ΔE,E setup.

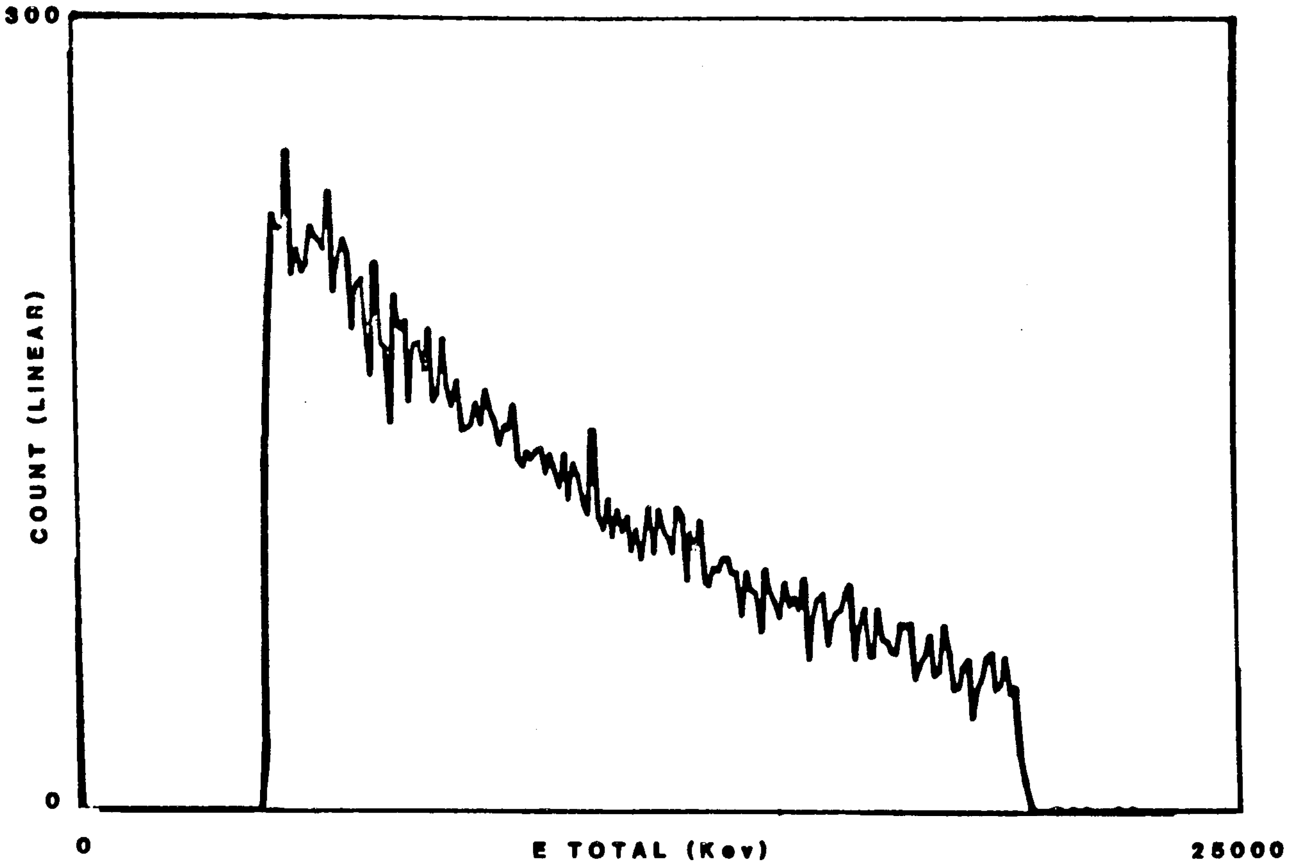

Fig. (5-4): A typical energy spectrum of recoil deuterons for interaction of 800 MeV protons with deuterium gas in ΔE,E setup.

Fig. (5-5): A typical energy spectrum of recoil protons for interactions of 800 MeV protons with hydrogen gas in time-of-flight setup.

C. Background

The accurate determination of the background is very important in this experiment. A background event is defined as an event whose characteristics (coincidence requirement, particle identification, and total energy signals) in the detector electronics system mimics the characteristics of the particle type of interest. One source of these background events could be reactions of the proton beam and its associated halo with the scattering chamber windows, walls, and any other material except the gas target. There could be two types of background events which are due to proton beam-target gas interactions outside of the interaction volume defined by the cross sectional area of the beam and the two slit collimation system. An interaction outside this volume can produce a high energy particle of the recoil type which passes through the collimator slit material and into the detector telescope or there can be some beam halo in the region between the front collimator and the detector telescope which scatters particles directly into the detector telescope. The first type of background which is not associated with target gas was measured by keeping all conditions the same as in the associated data run except that the scattering chamber was evacuated. This was called a target empty background run. The sum of all the background events produced by the interaction of the beam with the gas and with all other material was measured by keeping gas pressure in the scattering chamber and all other conditions the same as in the data run except that the movable slits of the front collimation were completely closed. Here, closing the slit only removed the recoil particles produced in the interaction volume. This was called a slit closed background run. In the case of p-p elastic scattering measurements (hydrogen gas target) a comparison of these two kinds of backgrounds with each other indicate that there is a contribution to the background from events associated with interactions in the hydrogen gas. This conclusion is based on the fact that the target empty background is consistently smaller (3 to 20%) than the slit closed target full background. For p-d elastic scattering measurements (deuterium gas target) the background runs are the same to within the statistical uncertainty of the data. As a result of above comparison for the ΔE-E setup it was decided to use the slit closed background runs for the p-p data and target empty background runs for the p-d data. For data taken with the time of flight setup only the target empty background was measured and therefore these data were used in the analyses. Comparisons of the background runs with the data runs showed that in the case of the p-d data background events were a small percentage of good events (less than 3%) and in the case of the p-p data between 10% and 15%.

D. Extrapolation Back to the Center of Interaction

The measured energy spectra were extrapolated back to the interaction region in a series of steps. This extrapolation takes into account the energy losses in the dead layers of each detector where relevant and in path length of gas between the interaction region and the detector telescope.

The stopping power function for each material that the recoil particle passed through in going from the interaction volume to the active region of the detectors is represented by a function:

$$\frac{dE}{d\xi} = AE^{-B} \qquad (\mathrm{MeV/g/cm^2}) \quad . \tag{5-2}$$

The parameters A and B were determined for each material by fitting Eq. (5-2) to the stopping power data of Williamson (Williamson 66). For the ΔE - E setup the energy of the particle E_i, incident on the ΔE detector is given in terms of the total energy, E_d, deposited in the detector telescope (both ΔE and E) by the formula: (APPENDIX C)

$$E_i = E_d + D_1 A E_d^{-B} + A\ (D_2 + D_3)\left[E_d^{B+1} - t_a A(B + 1)\right]^{-B/(B+1)} \tag{5-3}$$

where D_1, D_2, and D_3 are front and back dead layer of ΔE detector and front dead layer of E detector in g/cm^2 respectively, t_a is the thickness of ΔE detector in g/cm^2, and A and B are the parameters in Eq. (5-2) for the energy loss of the recoil particle of interest in the dead layer material.

The recoil particle energy at the interaction region E, was calculated by adding to E_i, the energy lost by recoil particle in passing through the target gas. (APPENDIX C)

$$E = \left\{E_i{}^{B+1} + \rho HA(B + 1)/\left[1 - \frac{(M + E_o)^2 E_i}{2MP_o{}^2(1 + E_i/2M)}\right]^{1/2}\right\}^{1/(B+1)} \tag{5-4}$$

where ρ is density of gas target in g/cm^2, H is shown in Fig. (3-2); E_0 and P_0 are the total energy and momentum of incident proton beam in the laboratory frame; A and B are the constants of Eq. (5-2) for the recoil particle of interest in the target gas; and M is the rest mass for the recoil particle.

Using Eqs. (5-3) and (5-4) the energies corresponding to the lower and upper limit of each energy bin for the energy deposited in the detector telescope were extrapolated back to the center of interaction. Tables (C-1), (C-2) and (C-3) show the energy loss correction for a p-p run with the ΔE-E setup and a target of 500 mm Hg hydrogen gas, for a p-p run with the time of flight setup and a target of 40 mm Hg hydrogen gas and for a p-d run with the ΔE-E setup and a target of 300 mm Hg deuterium gas, respectively.

E. Energy Binning in the Center of Interaction

Since the width of an energy bin at the center of interaction is changing from channel to channel; and for each particular channel it changes from run to run and from arm to arm, it was necessary to put the data into standard bins, in order to be able to sum up cross section and analyzing power data corresponding to a series of runs. The standard bin size was chosen to have a width of 100 keV, this corresponds to a width of 1.88×10^{-4} $(GeV/c)^2$ in four-momentum transfer squared, -t. The procedure for putting the data in standard bins is now described.

Suppose the lower and upper limits of a bin in the detector energy scale (Ed_i, Ed_{i+1}) extrapolate back to E' and E'', respectively at the center of interaction. If E' and E'' fall into standard bins with lower limits E_{i+1} and E'_{i+2} respectively, then the yield of particles in the standard bin at the interaction region with the lower limit E_{i+2} is:

$$Y_{i+2} = \frac{E'' - E_{i+2}}{E'' - E'} Yd_i + \frac{E_{i+3} - E''}{E''' - E''} Yd_{i+1}$$

where Yd_i and Yd_{i+1} are the yields of particle corresponding to the channel with lower limits Ed_i and Ed_{i+1}, respectively in the detector energy scale. Figure (5-6) illustrates this procedure graphically.

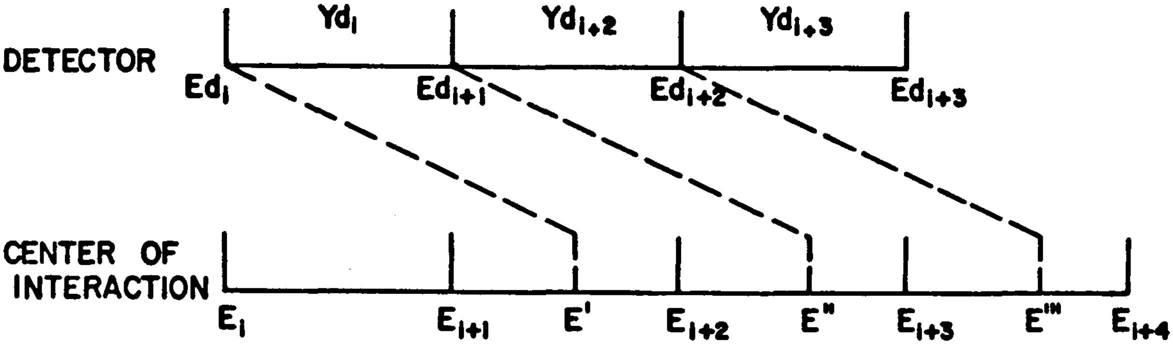

$$E_{i+2} > E' > E_{i+1}$$

$$E_{i+3} > E'' > E_{i+2}$$

Fig. (5-6): Graphical illustration of procedure used for energy binning in center of interaction.

If E'' and E''' fall within a standard bin with lower limit E_{i+2} in the center of interaction, then the yield of particle in this standard bin is:

$$Y_{i+2} = \frac{E'' - E_{i+2}}{E'' - E'} Yd_i + Yd_{i+2} + \frac{E_{i+3} - E'''}{E'''' - E'''} Yd_{i+3} \quad .$$

F. Experimental Uncertainties

The breakdown of instrumental uncertainties can be made into four separate categories: the error associated with the energy calibration of the detectors, with the absolute normalization of the Faraday Cup, with the measurement of the number of the nuclei per volume, and with the measurement of the geometrical factor defined in Chapter IV.

We estimate the ΔT bins (energy bins) are determined to an accuracy of ±0.5%, this has to do with how well we measure coefficient a in $E = a \cdot C + b$. Reproducibility of alpha data indicates that we can get to ±0.5%. From this, the uncertainty in dY/dT is about 0.6%, where the uncertainty in energy extrapolation is included.

The uncertainty in the measurement of the temperature and the pressure of the target gas is about 1%. Thus, the uncertainty in the number of target nuclei per volume is %1.5.

As was mentioned in Chapter III, the uncertainty in the Faraday Cup measurement is about 1%.

The uncertainty in the measurement of a, the area of the back collimator and H, the perpendicular distance from the beam direction to a middle point in circular collimator is 1%. Thus the error in the measurement of A, the geometrical factor is about %1.5.

Overall, including all errors mentioned, we estimate that the instrumental uncertainty in our measurements is about 3%. These error bars given in all data tabulations are statistical, but the uncertainty due to the background substraction is included.

G. Presentation

Figures (5-7) and (5-8) present the differential cross sections, $d\sigma/dt$, and analyzing powers, $A_y(\theta)$, respectively, for elastic proton-proton scattering at 800 MeV obtained in this work. Figures (5-9) and (5-10) present the differential cross sections and analyzing powers, respectively, for elastic proton-deuteron scattering at 800 MeV obtained in this work.

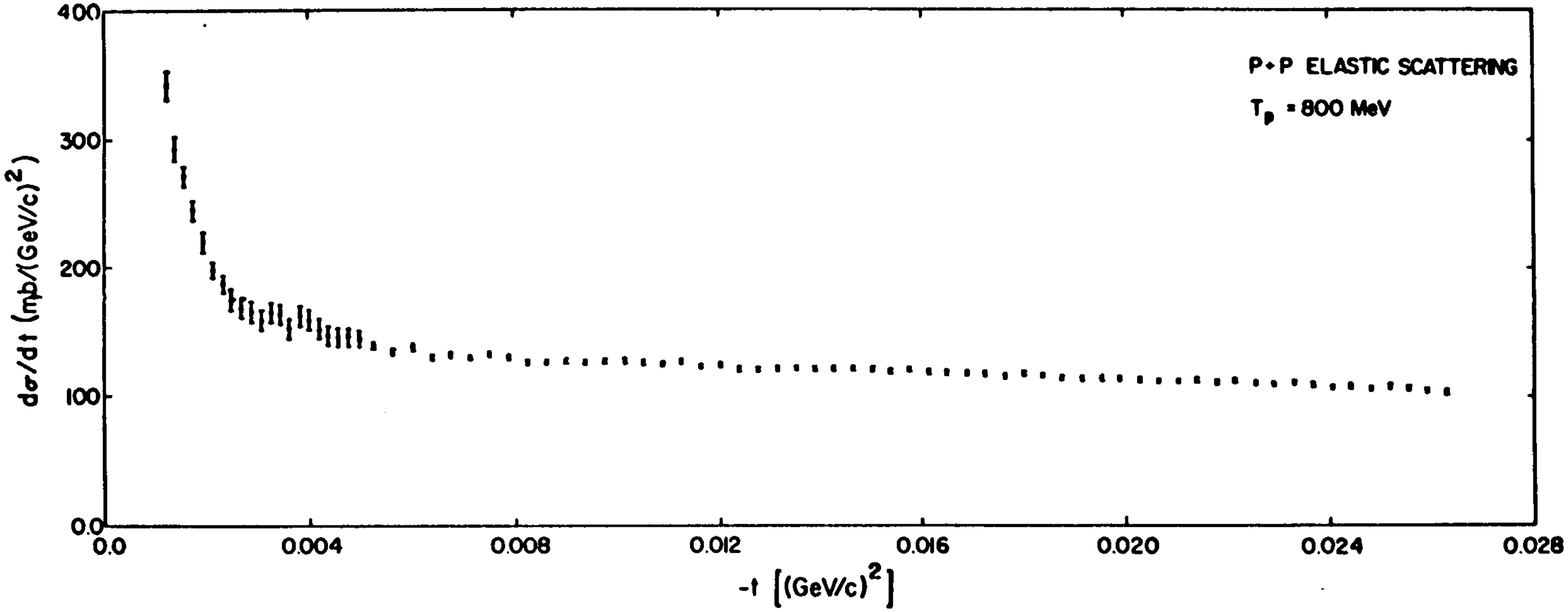

Fig. (5-7): The differential cross section for p-p elastic scattering at 800 MeV.

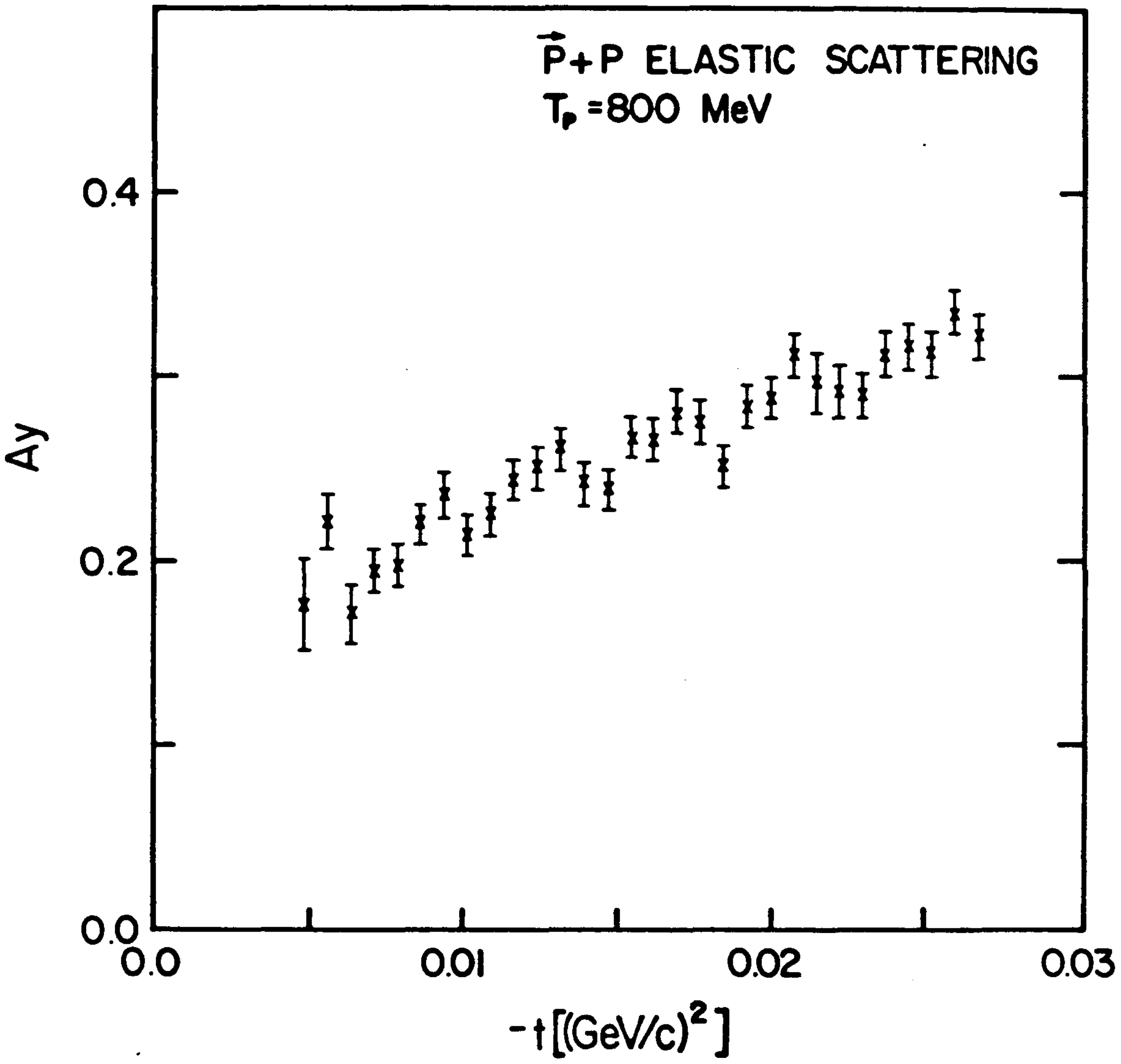

Fig. (5-8): The analyzing power for $\vec{p}$-p elastic scattering at 800 MeV.

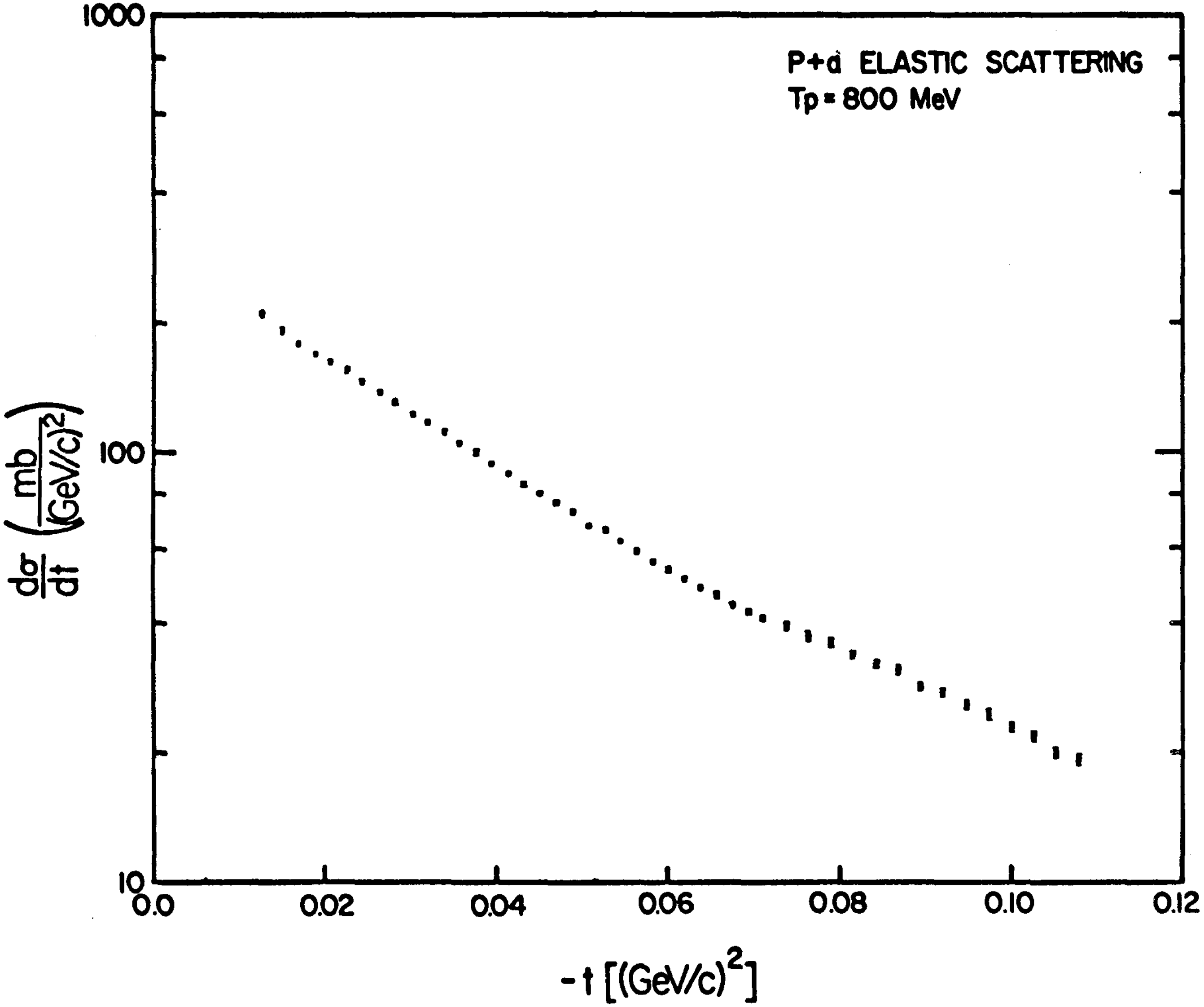

Fig. (5-9): The differential cross section for p-d elastic scattering at 800 MeV.

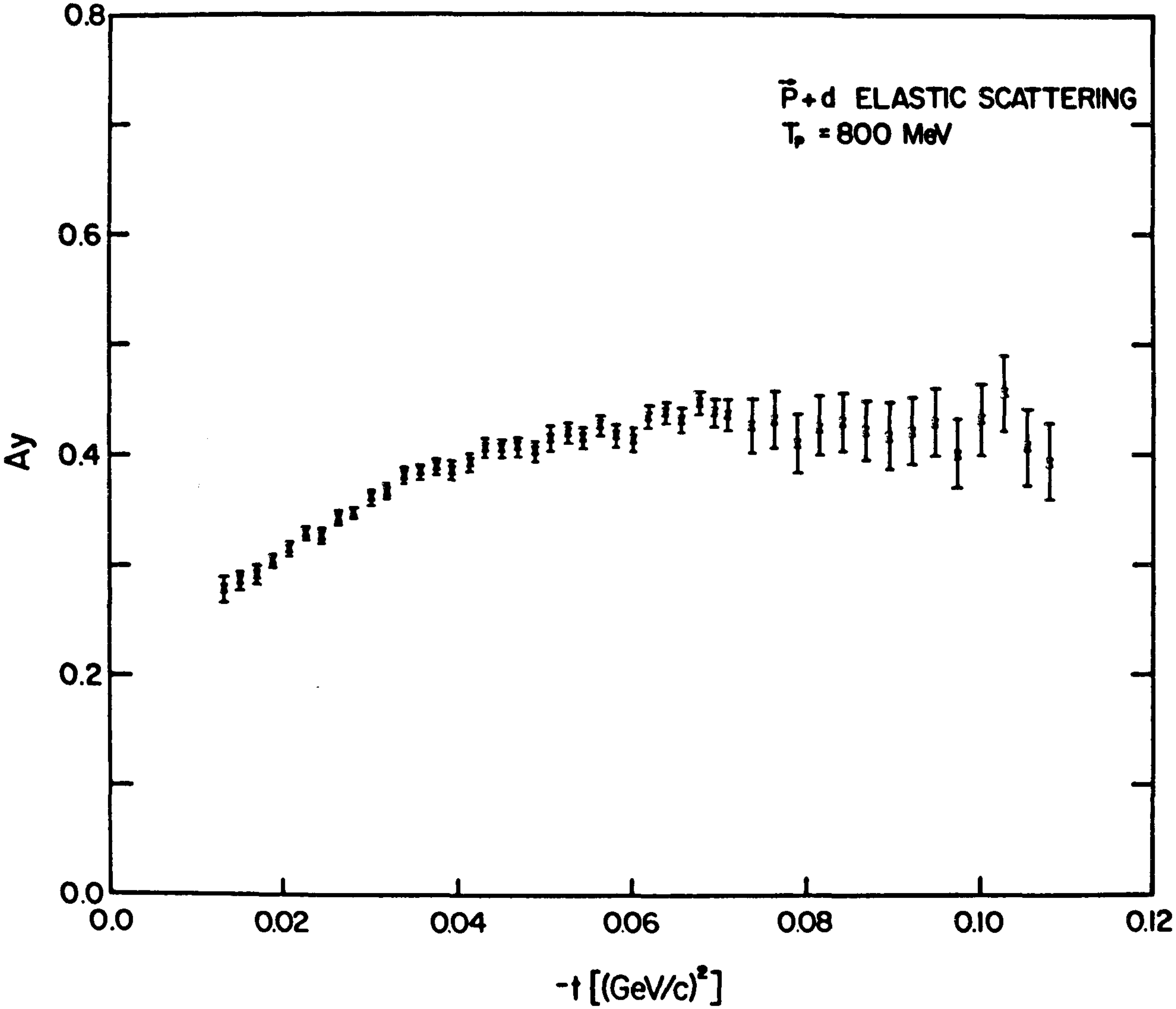

Fig. (5-10): The analyzing power for $\vec{p}$-d elastic scattering at 800 MeV.

CHAPTER VI

THEORETICAL ANALYSES FOR PROTON-PROTON DATA

In this chapter we will describe the theoretical analyses for the data obtained from our proton-proton elastic scattering experiments. We will discuss the fitting procedures used for the proton-proton elastic differential cross section, $d\sigma/dt$, and analyzing power, $A_y(\theta)$, data and compare the results obtained from these fitting procedures with theoretical predictions and other experimental results.

A. Functional Form of Differential Cross Section and Analyzing Power

In Chapter I formulae were developed for the differential cross section and analyzing power data in the frame work of the classical parameterization model. In order to increase sensitivity of the fit, we reduced the number of variable parameters by fixing the total cross section, σ_{ToT}, and slope parameters, b_1 and b_2. We introduced the value of $\sigma_{ToT} = 47.3 \pm 0.6$ Mb, taken from the compilation of proton-proton experimental data (Benary 70), which agrees well with the Arndt prediction (Arndt 80) through the optical theorem. There are many different inconsistent predictions and measurements for the slope parameters. Figure (6-1) shows a comparison of the non-spin-flip nuclear slope parameter, b_1, as a function of momentum in laboratory system from the proton-proton phase shifts analyses of Arndt (Arndt 80), Hoshizaki (Hoshizaki 79) and MacGregor (MacGregor 69) and from experimental measurements of $d\sigma/dt$ outside the Coulomb-nuclear interference region, $t>0.001$ $(GeV/c)^2$ (Benary 70).

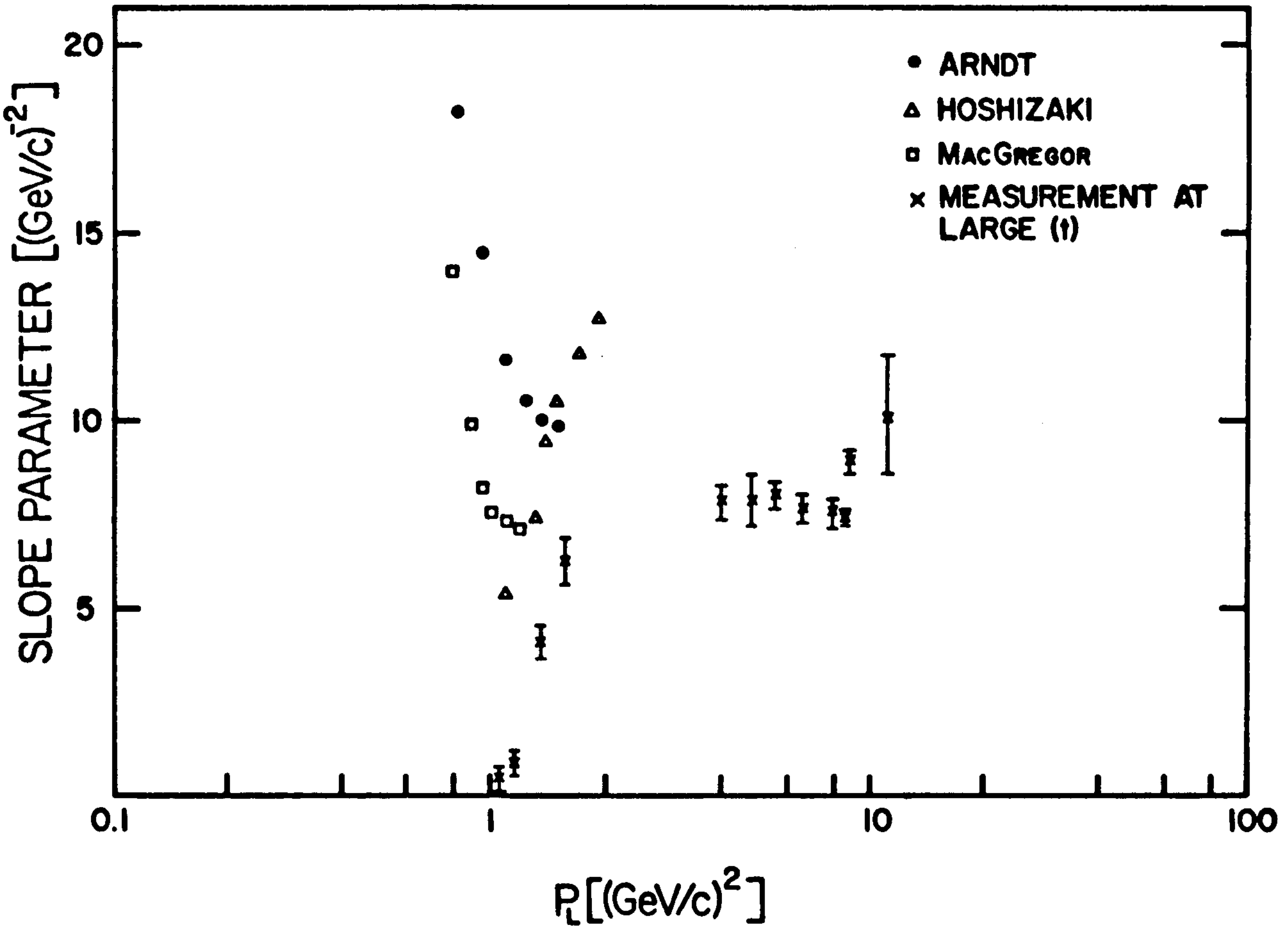

Fig. (6-1): A comparison of the nuclear spin-independent slope parameters as a function of laboratory momentum.

There are also discrepancies between different measurements and predictions for the double-spin-flip slope parameter, b_2. Thus, it has been decided to fit the data with different values of b_1 and b_2. With these observations in mind, we can rewrite Eqs. (1-54) and (1-59) explicitly in terms of the variable parameters ρ, R, γ_1, and γ_2.

$$\frac{d\sigma}{dt}\left(\frac{\text{mb}}{(\text{GeV/c})^2}\right) = \frac{0.0003676}{t^2} G_p^4(t) + 114.3(1 + \rho^2)(e^{b_1 t} + Re^{b_2 t})$$

$$- 0.410 \frac{G_p^2(t)}{|t|} \left(\rho + 0.0173 \text{ Ln } \frac{0.209}{\sqrt{|t|}}\right) e^{b_1 t/2}$$

$$+ 16.741 (\gamma_1^2 + \gamma_2^2)\sin\theta \qquad (6\text{-}1)$$

and

$$I_0 A(\text{fm/sr}) = 2.3375(\gamma_1 \sin\theta)e^{b_1 t/2} + 2.3375(\text{Re}\gamma_E)e^{b_1 t/2}$$

$$+ 0.0041 \frac{G_p^2(t)}{|t|} (\gamma_2 \sin\theta) \qquad (6\text{-}2)$$

where

$$Gp(t) = \frac{1}{(1 + |t|/0.71)^2}$$

and

$$\mathrm{Re}\gamma_E = \frac{\sqrt{0.3759 + 1/4t}}{|t|}\left(0.003520 + 0.01446t + 3.9 \times 10^{-5}t^2\right)G_p^2(t)$$

B. Least Squares Method

A method of least squares was used to fit the data in which the quantity

$$\chi_R^2(x) = \frac{\chi^2(x)}{N - m - 1} \qquad (6\text{-}3)$$

where

$$\chi^2(x) = \sum_i \left(\frac{\Delta_i}{\sigma_i}\right)^2$$

is minimized by varying x i.e. ρ, R, γ_1, and γ_2. Here, Δ_i is the deviation of the calculated from the measured value of the i'th observable, σ_i is experimental error in the measurements of the i'th observable, N is the number of data points used, and m is the number of free parameters. It can be shown from statistical theory (Orear 58) that the minimized value of reduced chi-squared, $\chi_R^2(x)$, should be, for a good fit, equal to 1. In the case of m parameters, $\chi^2(x)$ may be considered a continuous function of the m parameters describing a hypersurface in m-dimensional space as illustrated in Fig. (6-2).

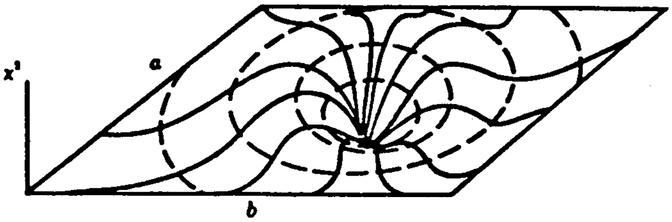

Fig. (6-2): Hypersurface describing variation of χ^2 vs two parameters a and b.

A valley may be found on this surface, and its bottom corresponds to the minimum of $\chi^2(x)$. There might be several such valleys, corresponding to several solutions. If the value of χ_R^2 at the bottom of a valley is very much larger than 1, the solutions may be disregarded as a spurious one. It can be shown (Bevington 69) that the uncertainty in each parameter corresponds to an increase in χ_R^2 of 1. That is, if we change one parameter, x_i, by an amount, Δx_i, and optimize all the other parameters for minimum χ_R^2, then the new value of χ_R^2 will be 1 greater than the old value.

$$\chi_R^2(x_i + \Delta x_i) = \chi_R^2(x_i) + 1 \quad . \tag{6-4}$$

C. Analysis of the Differential Cross Section Data

A product of expression (6-1) and a renormalization parameter, N, was used to fit the cross section data corresponding to the Coulomb-nuclear interference region $|t|<0.01$ • N was usually fixed; and the parameters ρ, R, and $\gamma = \sqrt{\gamma_1^2 + \gamma_2^2}$ were allowed to vary so as to obtain the best fit to the data. The procedure was repeated for different values of b_1 and b_2. We found that fortunately ρ, R, and γ are insensitive to b_2 and fairly insensitive to b_1 for all reasonable values of the slope parameters b_1 and b_2. Table (6-1) shows these results.

b_1	b_2	ρ	R	γ fm	χ_R^2
9.3	6.0	0.005	0.156	0.73	0.90
9.3	9.3	0.007	0.156	0.77	0.85
9.3	2.0	0.004	0.153	0.70	0.85
8.0	6.0	0.000	0.146	0.69	0.85
10.5	6.0	0.005	0.157	0.88	0.85

Table (6-1) - Sensitivity of fit to the cross section to the slope parameters, b_1 and b_2.

As was discussed in Chapter V, we estimate the accuracy of our data normalization to be about ±3%. Comparison of our elastic proton-proton differential cross section data with those predicted by the Arndt (Arndt 80) phase shifts analysis gives a renormalization factor about 0.985. Also, these data are in good agreement with data taken at LAMPF using the High Resolution Spectrometer (HRS) (Wriekat 80) presented in Fig. (6-9). Thus, it is reasonable to repeat the fitting procedure with N fixed at 1 ± 0.03 and let ρ, R, and γ vary. It was observed that ρ, R, and γ are sensitive to the value N. Table (6-2) shows these results.

N	b_1	b_2	ρ	R	γ fm	χ_R^2
0.97	9.3	6.0	-0.010	0.163	0.90	0.84
1.03	9.3	6.0	0.016	0.147	0.66	0.87

Table (6-2) - Variation of ρ, R, and γ with the normalization constant N.

It was mentioned in Chapter V that the energy calibration of the solid state detectors is within ±30 keV, and this uncertainty in measurement of the energy E, is directly reflected in determination of four momentum squared transfer, -t. Therefore the fitting procedure was repeated for a shift in -t corresponding to a ±30 keV energy shift. The values of ρ, R, and γ are sensitive to the shift in -t; and the results are summarized in Table (6-3).

Shift (keV)	b_1	b_2	N	ρ	R	γ fm	χ_R^2
-30	9.3	6.0	1.0	0.048	0.184	0.5	1.0
+30	9.3	6.0	1.0	-0.035	0.133	0.84	0.76

Table (6-3) - Variation of ρ, R, and γ with a shift in the four momentum transfer squared, -t.

Table (6-4) shows the uncertainties in ρ, R, and γ due to the uncertainties in the normalization constant energy calibration, non-spin-flip slope parameter, b_1 and the uncertainty corresponding to a variation of 1 in χ_R^2. All these errors are approximately independent and hence added incoherently.

	ρ	R	γ fm
Error due to normalization	±0.01	±0.01	±0.1
Error due to Shift in energy	±0.04	±0.025	±0.2
Error due to b_1	±0.005	±0.012	±0.15
Error due to $\chi_R^2 + 1$	±0.007	±0.004	±0.07
Error	±0.04	±0.03	±0.28

Table (6-4) - Uncertainties in ρ, R, and γ due to normalization, energy shift, slope parameter, b_1 and $\chi_R^2 + 1$.

To compare our results with other available experimental results Wriekat 80), (Aebischer 76), (Varobyov 72), we have also tried to fit our data using the functional form of (6-1), but neglecting the spin-flip (orbit) contribution; that is, γ was set equal to zero. The results obtained are shown in Table (6-5).

b_1	b_2	N	ρ	R	χ_R^2
9.3	6.0	1.0	0.018	0.18	0.82

Table (6-5) - Results of a fit where the spin-orbit contribution is neglected; that is, γ is set equal to zero.

Table (6-6) presents the values obtained for ρ, R, and γ in this work from the analysis of p-p elastic scattering data at 800 MeV.

ρ	R	γ fm
+0.005	0.16	0.7
±0.04	±0.03	±0.28

Table (6-6) - Results obtained from this work for ρ, R, and γ.

Figure (6-3) shows the fit to the data obtained by fixing $b_1 = 9.3$ $(Gev/c)^{-2}$ (Arndt prediction), $b_2 = 6$ $(GeV/c)^{-2}$, $N = 1.0$, no shift in $|t|$ and using the values of ρ, R, and γ presented in Table (6-6). Figures (6-4) and (6-5) show the Arndt (Arndt 80) and Hoshizaki

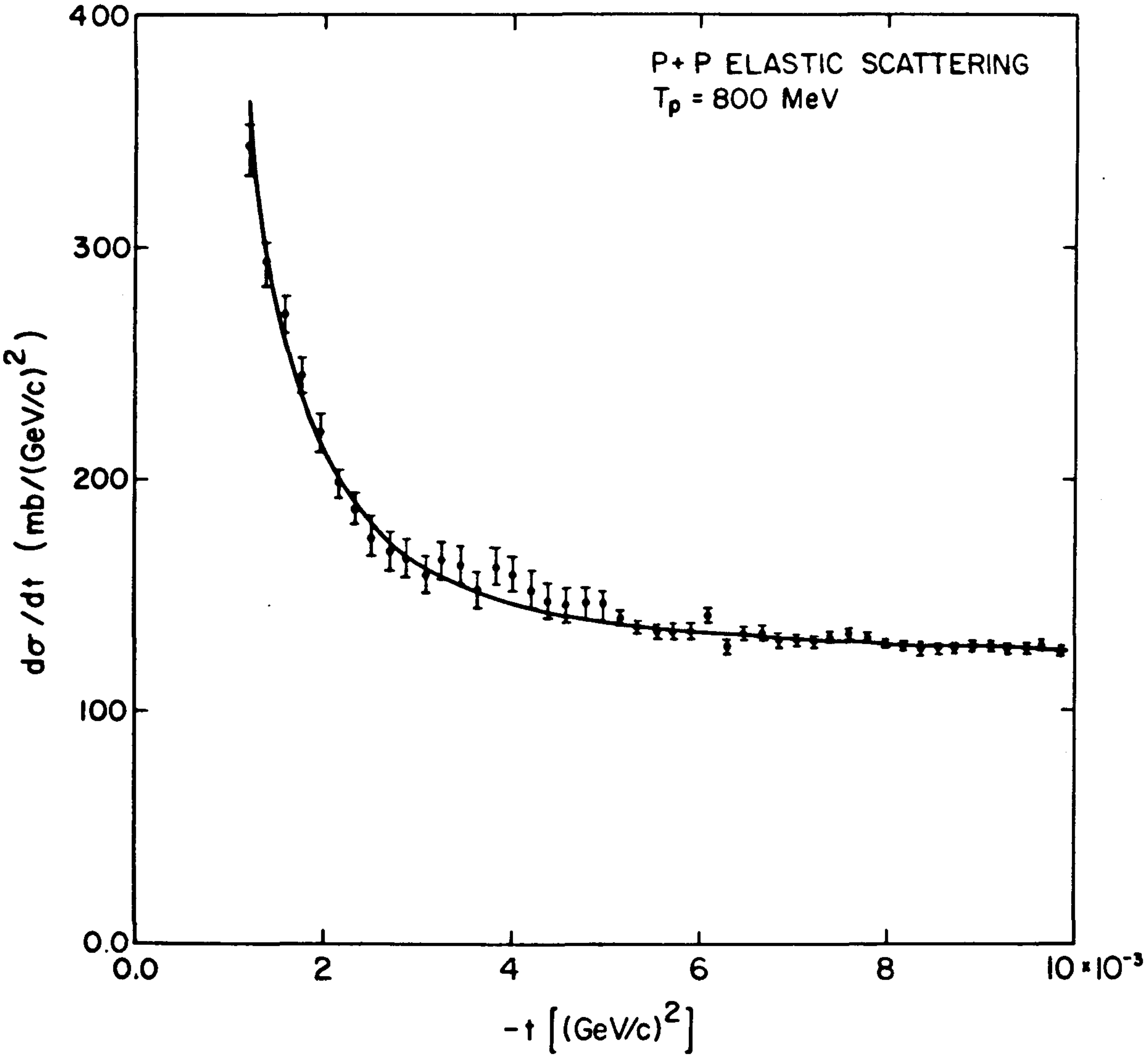

Fig. (6-3): The differential cross section for elastic p-p scattering, dσ/dt, at 800 MeV. The solid line through the data represents our parameterization with $b_1 = 9.3$ $(\mathrm{GeV/c})^{-2}$, $b_2 = 6.0$ $(\mathrm{GeV/c})^{-2}$, $N = 1.0$, $\rho = +0.005$, $R = 0.16$, and $\gamma = 0.7$ fm.

(Hoshizaki 79) phase shifts predictions, forward dispersion calculations (FDR)(Grein 78), and recent experimental values for ρ and R, respectively. The interesting qualititive feature of Fig. (6-4) is the rapid decrease and change of sign for ρ between 1 and 2 GeV/c followed by a more slowly decreasing behavior above 2 GeV/c. In fact Hoshizaki (Hoshizaki 78) suggests that the rapid fall and change of sign of ρ can be explained in terms of a $^1D_2$ resonance at ~1.2 GeV/c and a $^3F_3$ resonance at ~1.5 GeV/c. Figure (6-4) shows, indeed, there is a good agreement between our measurement of ρ, the Arndt phase shifts prediction and the FDR calculation, but our value for ρ is somewhat higher than the value predicted by Hoshizaki. Our value of ρ is consistent with the energy dependence suggested by previous measurements [with the exception of Dutton's data (Dutton 67,68)]. Figure (6-5) presents FDR calculations (Grein 78) and Arndt (Arndt 80) and Hoshizaki (Hoshizaki 78) phase shifts predictions for R along with our determination of R at 1.46 GeV/c and other experimental determination in the range of P_{lab} from 0.9 to 1.7 GeV/c. Our experimental result and the experimental work of Aebischer (Aebischer 76) and Wriekat (Wriekat 80), show quite reasonable agreement with the three theoretical predictions. The values of R and γ indicate that there is a sizable spin-dependent contribution to the forward differential cross section for elastic proton-proton scattering in this energy range.

D. Analysis of the Analyzing Power Data

Expression (6-2) was used to fit the product of the cross section and analyzing power data in the region where they overlap. The value of the slope parameter, b_1, was fixed at the Arndt prediction, $b_1 = 9.3$ $(\mathrm{Gev/c})^{-2}$, σ_{ToT} was fixed at 4.73 $(\mathrm{fm})^2$, which is the Benary value (Benary 70), and γ_1 and γ_2 were allowed to vary to obtain the best fit to the data. The fitting procedure was repeated for different values of b_1 and σ_{ToT}. Also, a renormalization factor, N, of 1 ± 0.03 was considered for the cross section data and the fitting procedure was repeated. It was observed that γ_1 and γ_2 are quite insensitive to the assumed values for b_1, σ_{ToT} and N.

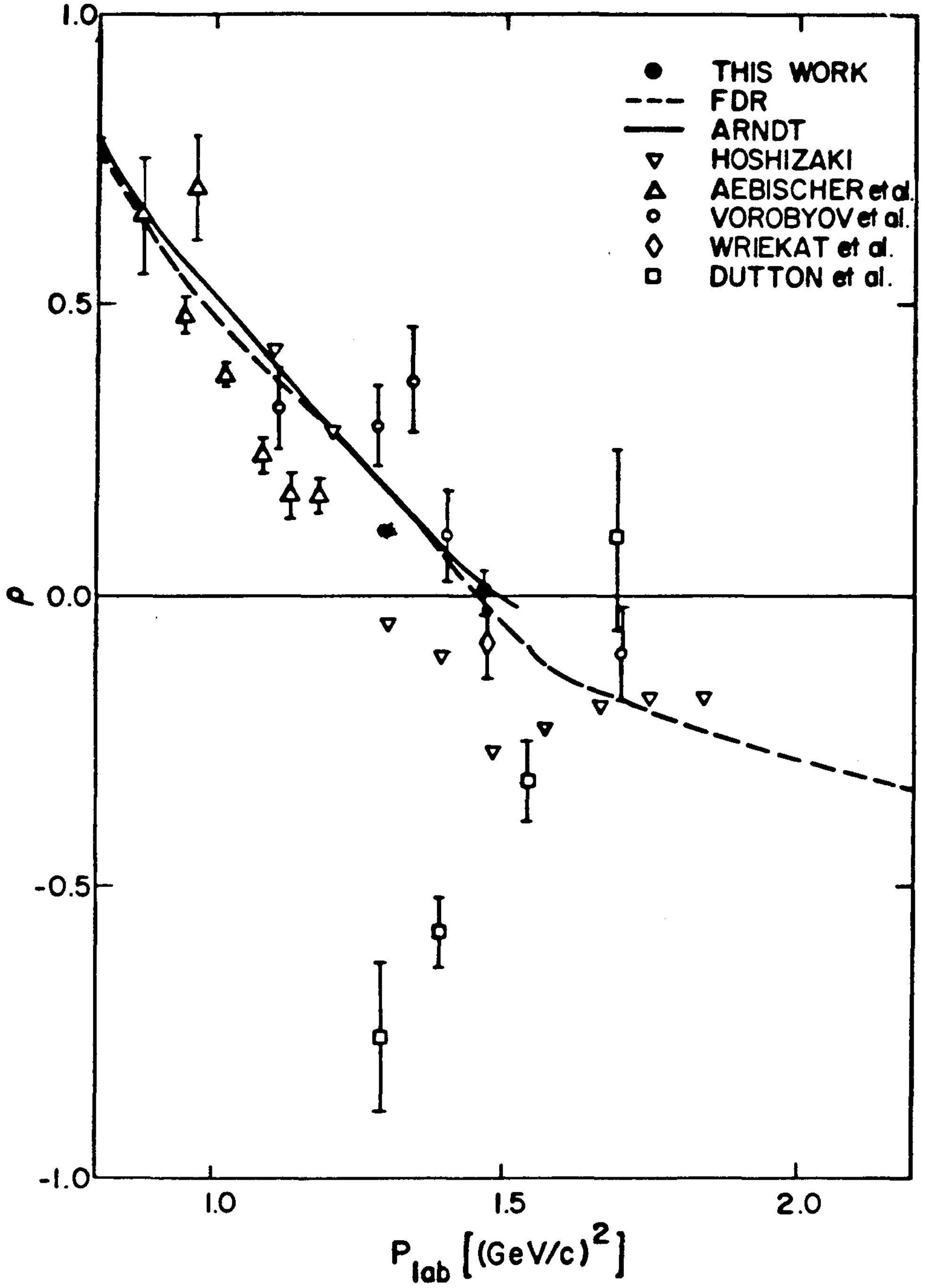

Fig. (6-4): ρ, the ratio of the real and imaginary parts of the forward p-p spin-independent scattering amplitude as a function of laboratory momentum.

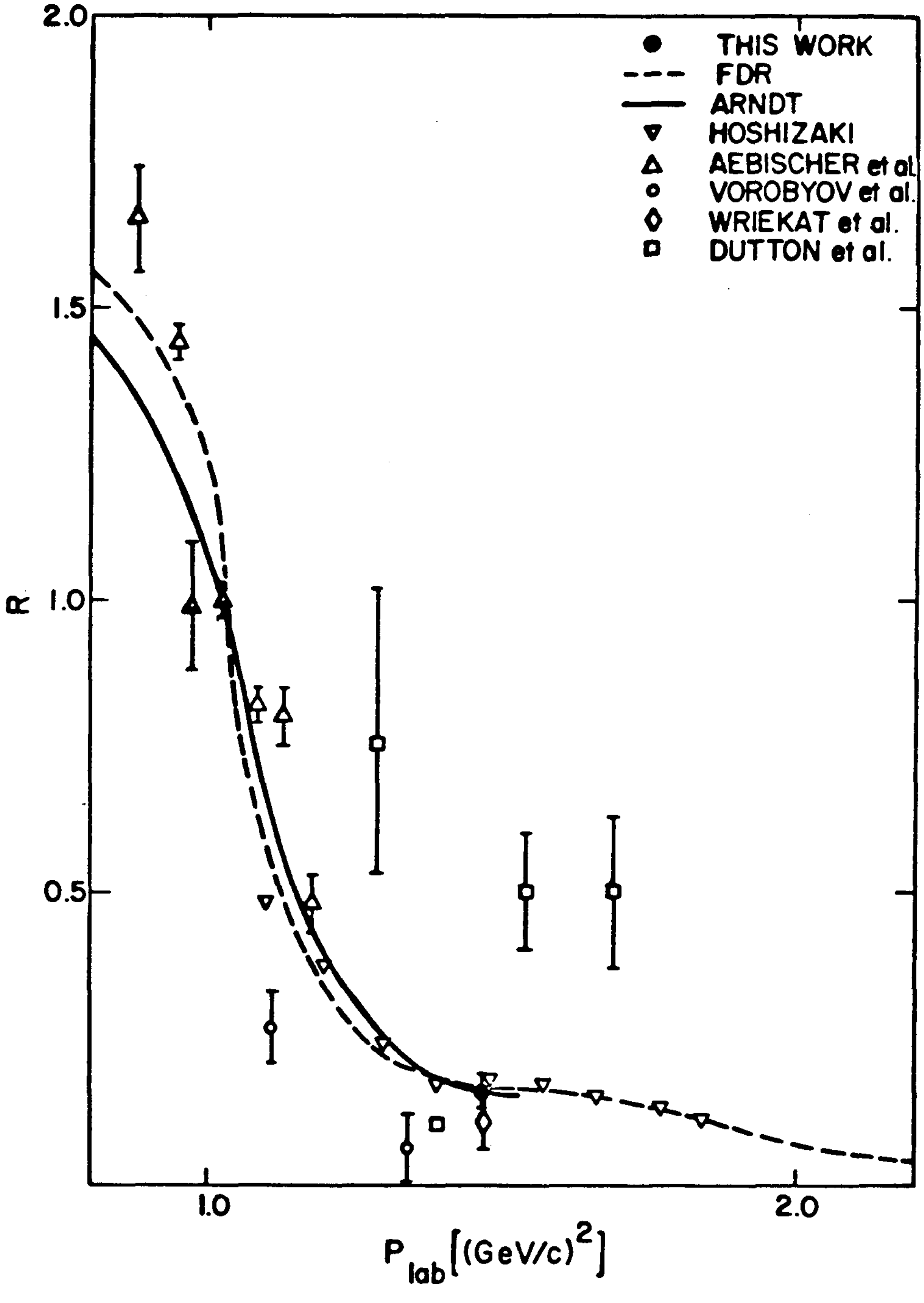

Fig. (6-5): R, the ratio between the summed moduli squared of the p-p double-spin-flip amplitudes at forward direction and the modulus squared of the p-p spin-independent amplitude at forward direction as a function of the laboratory momentum.

Table (6-7) shows these results. The error corresponding to a variation of 1 in χ_R^2 for γ_1 and γ_2 is 0.05 fm and 0.10 fm, respectively.

$b_1 (GeV/c)^2$	σ_{ToT} $(fm)^2$	N	γ_1 fm	γ_2 fm	χ_R^2
9.3	4.73	1.0	0.72	0.18	0.92
9.3	4.67	1.0	0.73	0.20	0.92
9.3	4.8	1.0	0.71	0.17	0.92
8.0	4.73	1.0	0.71	0.24	0.92
10.5	4.73	1.0	0.74	0.16	0.88
9.3	4.73	0.97	0.70	0.16	0.90
9.3	4.73	1.03	0.74	0.23	0.90

Table (6-7) - Sensitivity of the product of the analyzing power times cross section to variation in the slope parameter, b_1, total cross section, σ_{ToT}, and N the normalization factor of the cross section.

Thus by considering the uncertainties in b_1, σ_{ToT}, and N, we estimate the errors in the measurements of γ_1 and γ_2 to be 0.05 fm and 0.11 fm, respectively. Table (6-8) shows the results obtained for γ_1 and γ_2 in this experiment.

γ_1 fm	γ_2 fm
0.79 ± 0.05	0.18 ± 0.11

Table (6-8) - Results obtained from this work for γ_1 and γ_2.

Figure (6-6) shows the fit to the experimental values of I_oA (product of cross section and analyzing power) obtained by fixing $b_1 = 9.3$ $(GeV/c)^{-2}$, $\sigma_{ToT} = 4.73$ $(fm)^2$ and $N = 1$, and using the values for γ_1 and γ_2 presented in Table (6-8); that is, $\gamma_1 = 0.79$ and $\gamma_2 = 0.18$. As we have shown in Table (1-3) the contribution of $Re\alpha_E Im\gamma_N$ to $(I_oA)_I$ in the angular range of our data is quite small, and some authors (Aebischer 77) disregard this in their expression for (I_oA). Thus, in order to compare our result with their value for γ_1, we set the value of γ_2 to be zero, and let γ_1, vary. With this procedure, we obtained $\gamma_1 = 0.75$ fm. Figure (6-7) shows Arndt (Arndt 80) and Hoshizaki (Hoshizaki 79) phase shifts prediction for γ_1. The agreement of our value for γ_1 with Arndt prediction can be considered good if we consider error corridor in his prediction. Also our value of γ_1 is consistent with the energy dependence suggested by previous measurements (Aebischer 77). As was mentioned previously the only term depending on γ_2 in our expression for (I_oA) is $Re\alpha_E Im\gamma_N$ which is considerable only in very small angle measurements. Our data for the p-p elastic scattering analyzing power at 800 MeV do not extend low enough in $|t|$ to be really sensitive to γ_2. Thus our determination of γ_2 has a quite large error. Figure (6-8) shows Arndt (Arndt 80) and Hoshizaki (Hoshizaki 79) phase shifts prediction for γ_2.

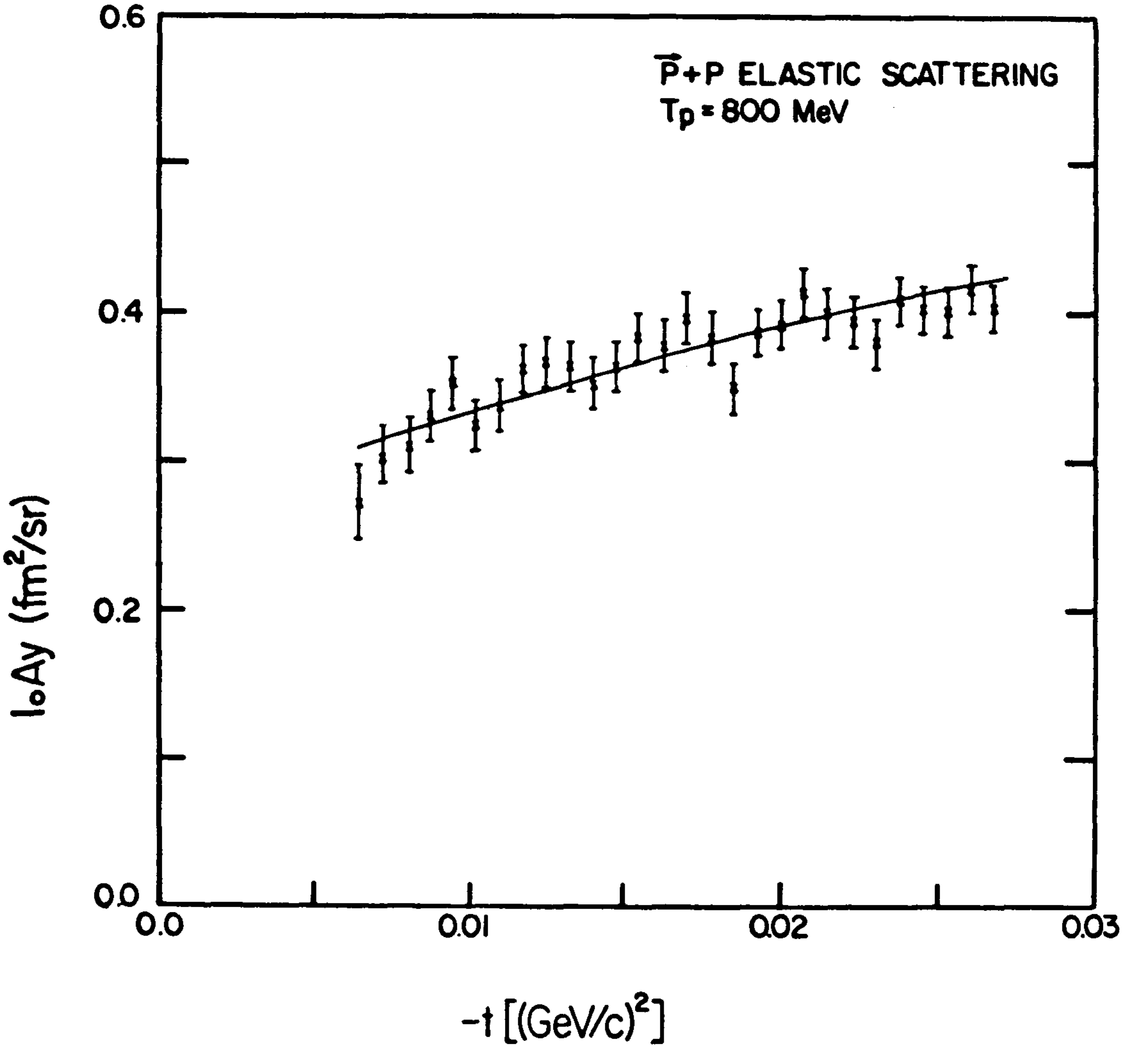

Fig. (6-6): Product of p-p elastic differential cross section, $d\sigma/dt$, and the p-p elastic analyzing power, A_y at 800 MeV. The solid line is the fit to the data with $b_1 = 9.3$ $(\text{GeV}/c)^{-2}$, $\sigma_{ToT} = 4.73\ (\text{fm})^2$, $N = 1$, $\gamma_1 = 0.79$ fm, and $\gamma_2 = 0.18$ fm.

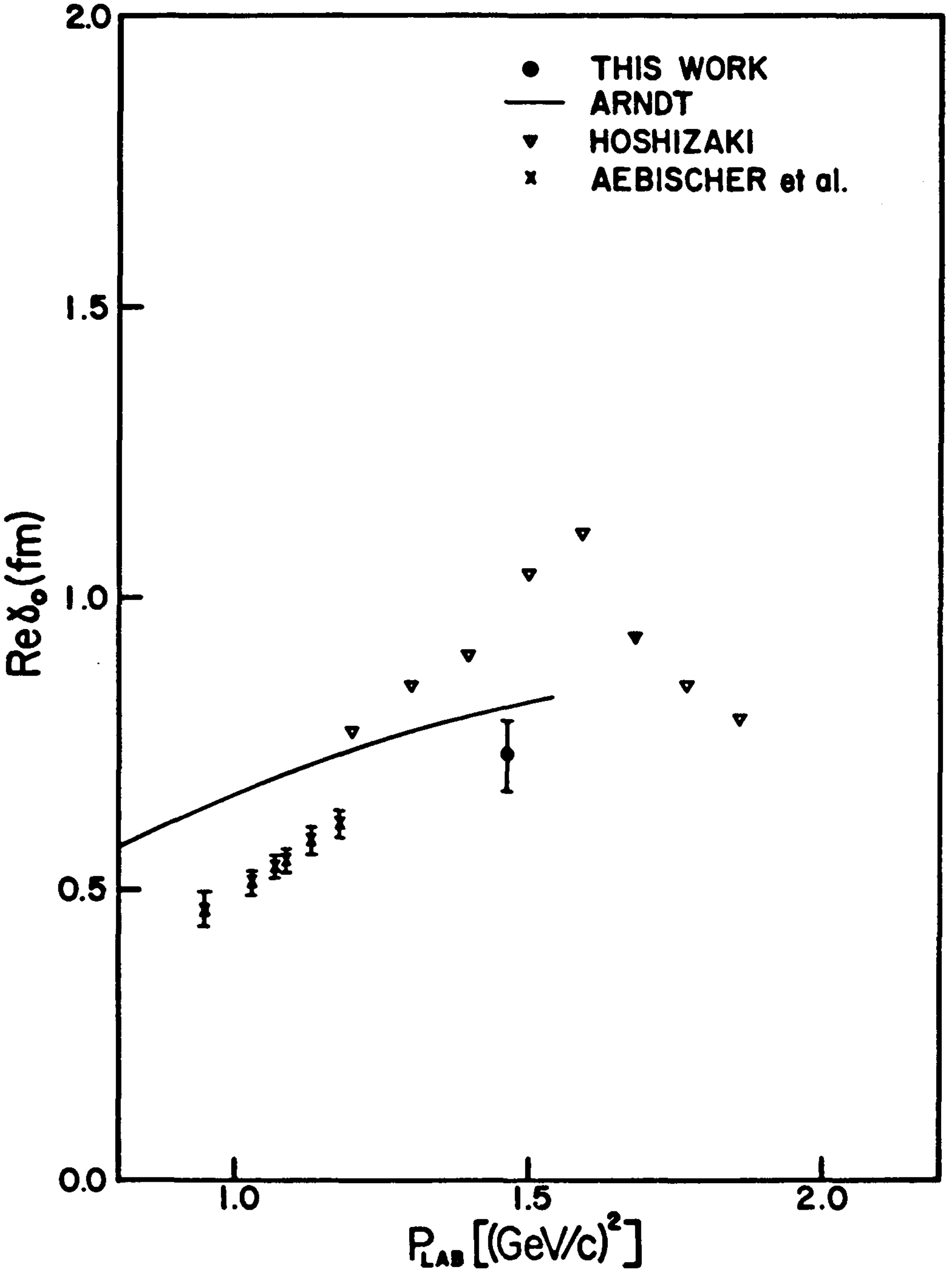

Fig. (6-7): The real part of p-p spin-orbit scattering amplitude divided by sinθ as a function of laboratory momentum.

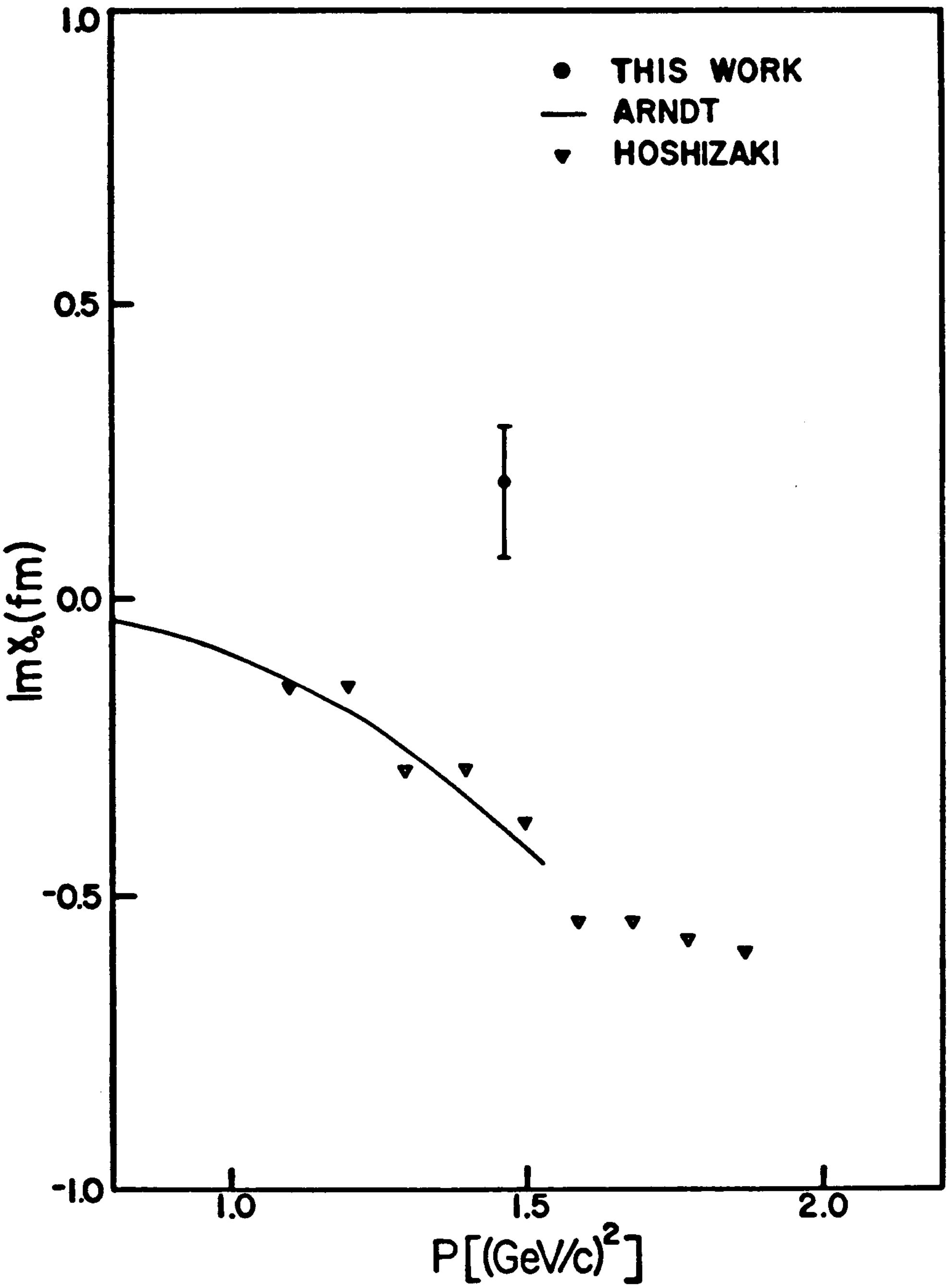

Fig. (6-8): The imaginary part of spin orbit scattering amplitude divided by sinθ as a function of laboratory momentum.

E. Discussion

Absolute differential cross section and analyzing power measurements for elastic proton-proton scattering at 800 MeV with an uncertainty of ±3% have been presented as a part of this dissertation. These measurements have been done in the region of four momentum transfer: $0.0012<|t|<0.027$ $(\mathrm{GeV}/c)^2$ for the cross section data and $0.005 <|t|<0.027$ $(\mathrm{GeV}/c)^2$ for the analyzing power data which correspond to laboratory angles ranging between 1.34° and 6.45°, and between 2.80° and 6.45°, respectively. These data are more accurate and reliable than earlier measurements in this energy region. This is due to four features of the present experiment. First, the advantages of the recoil particle method used in this experiment over the conventional method of detecting scattered particles in the near forward direction. Second, the fact the EPB has a working Faraday Cup with an accuracy of about 1% allowed us to obtain excellent accuracy in our normalization. Third, in our method we measured the four-momentum transfer, t, directly [Eq. (4-41)] with good accuracy. Fourth, the quality of the EPB beam (phase space, arial dimension, small halo) is very good compared with that at other facilities. Figure (6-9) presents our data and Wriekat et al. measurements of elastic proton-proton cross section at 800 MeV in the region they overlap (Wriekat 80). Comparison of our differential cross section data for proton-proton elastic scattering at 800 MeV with those predicted by the Arndt (Arndt 80) phase shift analysis gives a renormalization factor about 0.985.

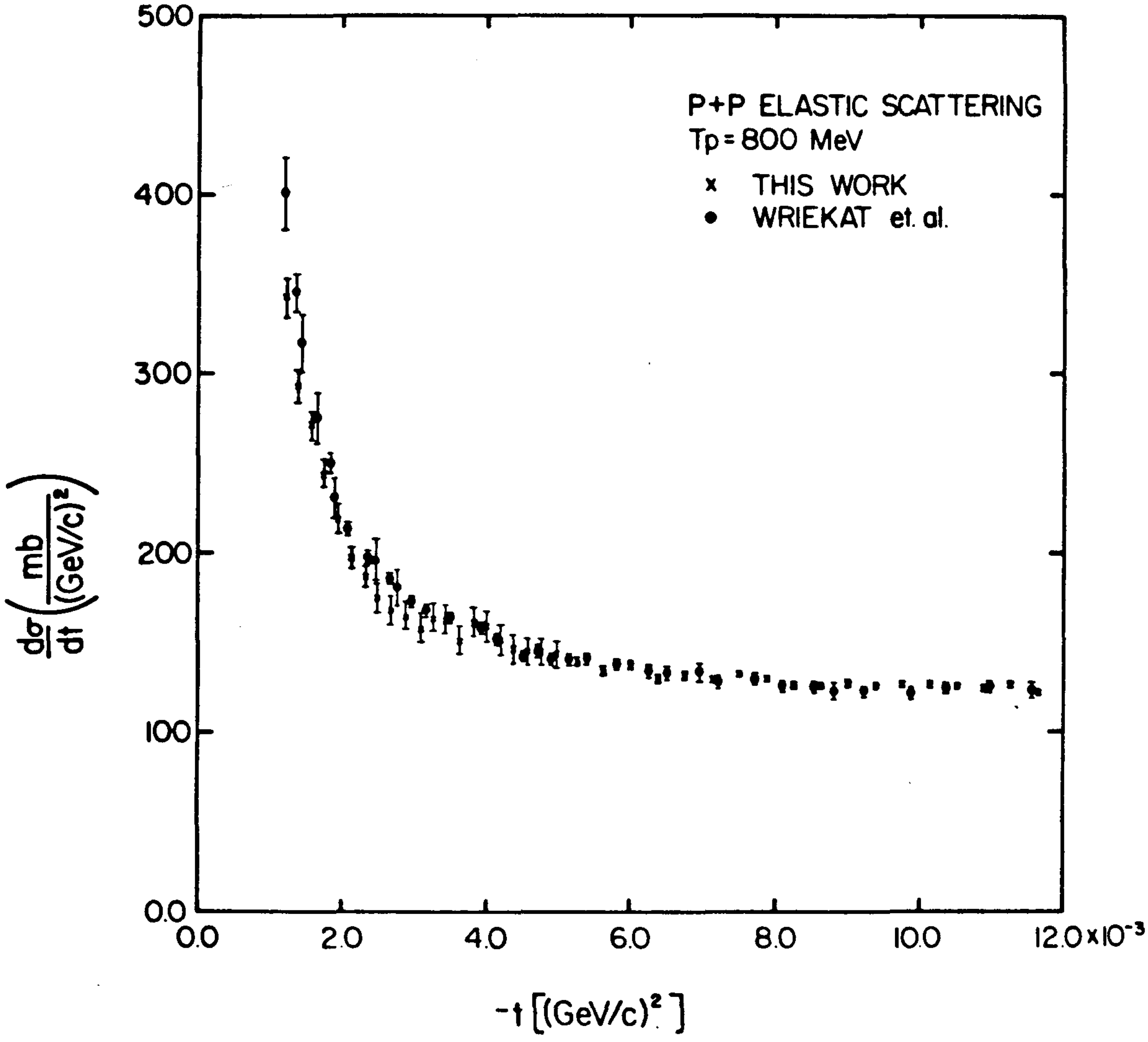

Fig. (6-9): A comparison of our data for the cross section in p-p elastic scattering at 800 MeV with other data obtained at LAMPF using the HRS facility (Wriekat 80).

Figure (6-10) shows a comparison of our data for the analyzing power in proton-proton elastic scattering at 800 MeV with other data obtained in LAMPF using the HRS facility (Pauletta 80) and the Arndt prediction for the analyzing power at 800 MeV. There is a good agreement between the two sets of measurements, although there is a disagreement between the measured analyzing power and the Arndt prediction at 800 MeV.

Fits to the data were made using the classical parameterization model to obtain value for ρ, the ratio between the real and imaginary parts of spin-independent amplitude in the forward direction, for R, the ratio between the summed moduli squared of the double spin-flip amplitudes at zero degrees and the modulus squared of spin-independent amplitude at zero degrees, and for γ_1, which is related to the real part of the spin-orbit amplitude by Eq. (1-44). From a measurement of ρ, one can obtain the real part of nuclear spin-independent amplitude in the forward direction, $\mathrm{Re}\alpha_N(0)$. The total proton-proton cross-section data of Auer _et al_. (Auer 77,77,78) for transversely and longitudinally polarized beams and targets can be used to determine the imaginary parts of the double spin-flip amplitudes in the forward direction:

$$\Delta\sigma_T = \sigma(\uparrow\downarrow) - \sigma(\uparrow\uparrow) = -\frac{4\pi}{P_L}\,\mathrm{Im}\big(2B_N(0)\big)$$

$$\Delta\sigma_L = \sigma\left(\substack{\rightarrow\\ \leftarrow}\right) - \sigma\left(\substack{\rightarrow\\ \rightarrow}\right) = \frac{4\pi}{P_L}\,\mathrm{Im}\big(2\varepsilon_N(0)\big)\ ,$$

and thus one can determine the sum of the squares of the real parts of spin double-flip amplitudes from a measurement of R. Such information on the real and imaginary parts of the double spin-flip amplitudes acquires particular significance in the light of recent speculations concerning the existence of the dibaryon resonances. A recent FDR calculation by Grien (Grien 78), suggests an energy dependence in the real parts of the forward amplitudes which is characteristic of resonance behavior and which is evidence in support of dibaryon resonances. Also Hoshizaki (Hoshizaki 78) has suggested a structure in the real and imaginary parts of $\beta(0)$ and $\varepsilon(0)$, which he explained in terms of $^1D_2$ and $^3F_3$ resonances. Thus, it is clearly important to obtain independent verification of the real parts of all forward amplitudes.

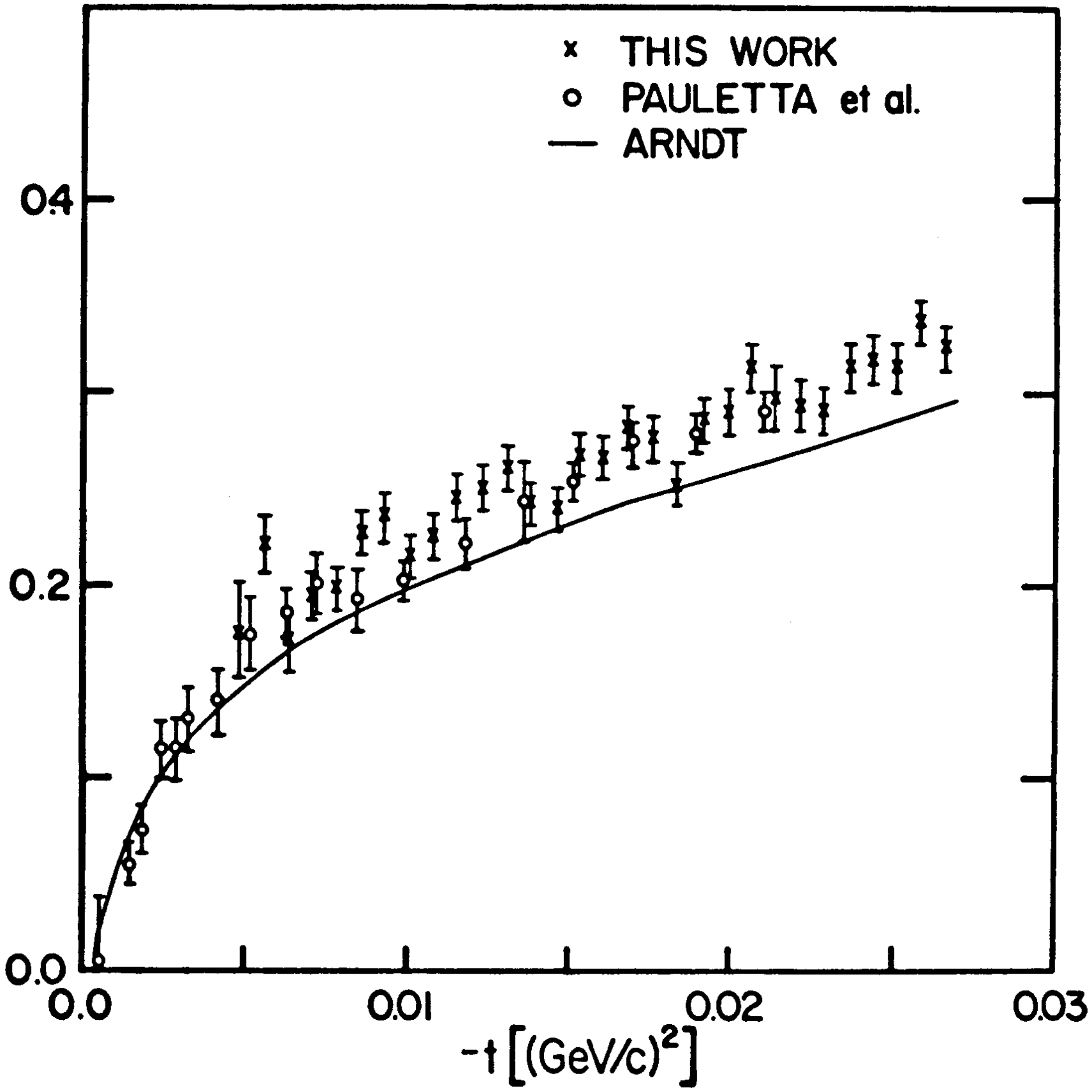

Fig. (6-10): The analyzing power for elastic $\vec{p}$-p scattering at 800 MeV. The crosses are this work. The open circles are data obtained using HRS facility (Pauletta 80). The solid line is the Arndt phase shifts prediction (Arndt 80).

CHAPTER VII

THEORETICAL ANALYSES FOR PROTON-DEUTERON DATA

In this chapter, we will describe the theoretical analyses for the data obtained from our p-d elastic scattering experiment. We will test if available nucleon-nucleon amplitudes are able to predict proton-deuteron scattering in the framework of the theory outlined in Chapter II, at 800 MeV. Also we will discuss the fitting procedure used for the p-d elastic analyzing power, $A_y(\theta)$ data.

A. Analyses of the Analyzing Power and Differential Cross Section

In Chapter II the formulae developed for the analysis of analyzing power data within the theoretical framework for p-d scattering used isospin averaged nucleon-nucleon amplitudes. In order to increase sensitivity of the fit, we reduced the number of variable parameters by fixing σ_p and σ_n (the total cross section for p-p and p-n scattering, respectively), b_p and b_n (the slope parameters), and ρ_{pp} and ρ_{pn} (the ratio between the real and imaginary parts of the spin-independent amplitude at zero degrees for p-p and p-n scattering, respectively). The values of $\sigma_p = 4.73 \pm 0.06\ (\mathrm{fm})^2$ and $\sigma_n = 3.79 \pm 0.07\ (\mathrm{fm})^2$ were taken from the compilation of proton-proton and proton-neutron experimental data (Benary 70). Slope parameters were fixed at the values predicted by the Arndt phase shifts analysis $b_p = 9.3\ (\mathrm{GeV/c})^{-2}$ and $b_n = 10.3\ (\mathrm{GeV/c})^{-2}$. Forward dispersion relation calculations (Grein 78) predicted an upper limit of −0.4 and a lower limit of −0.8 for ρ_{pn} and a value of 0.0 for ρ_{pp}. Also, the Arndt phase shifts predicted $\rho_{pp} = 0.02$ and $\rho_{pn} = -0.3$. From our analyses of p-p data we obtained $\rho_{pp} = 0.005$. Using these quantities, we can rewrite Eq. (2-18) in terms of only two variables, A and B, which were defined in Eq. (2-19)

$$A_y(\theta) = \frac{0.247\left[\sigma_p(A-\rho_{pp}B)e^{b_p t/2} + \sigma_n(A - \rho_{pn}B)e^{b_n t/2}\right]\sin\theta}{I_o} \qquad (7\text{-}1)$$

where

$$I_o = 0.0153\ \left[\left(\sigma_p e^{b_p t/2} + \sigma_n e^{b_n t/2}\right)^2 + \left(\rho_{pp}\sigma_p e^{b_p t/2} + \rho_{pn}\sigma_n e^{b_n t/2}\right)\right]$$

$$+ 2\left(A^2 + B^2\right)\sin^2\theta$$

and

$$A = \frac{1}{2}\left(\gamma_{1p} + \gamma_{1n}\right)$$

$$B = \frac{1}{2}\left(\gamma_{2p} + \gamma_{2n}\right) .$$

This expression was used to fit the analyzing power data. A and B were allowed to vary to obtain the best fit to the data. The fitting procedure was repeated for different values of slope parameters (b_p and b_n) and total cross sections (σ_p and σ_n). It was observed that A and B are fairly sensitive to the assumed values of b_p, b_n, σ_p and σ_n.

Table (7-1) shows sensitivity for the fitted values for A and B when different values of ρ_{pp} and ρ_{pn} are assumed.

A fm	B fm	ρ_{pp}	ρ_{pn}	$b_p(\mathrm{GeV/c})^{-2}$	$b_n(\mathrm{GeV/c})^{-2}$	χ^2_R
0.86	-1.0	0.0	-0.8	9.3	10.5	0.96
0.79	-1.0	0.0	-0.4	9.3	10.5	0.95
0.77	-1.0	0.02	-0.3	9.3	10.5	0.95
0.77	-1.0	0.005	-0.3	9.3	10.5	0.95

Table (7-1) - Sensitivity of A and B to ρ_{pp} and ρ_{pn}.

The error corresponding to a variation of 1 in χ^2_R for A and B is 0.01 fm and 0.03 fm, respectively. Thus by considering the uncertainties in ρ_{pp} and ρ_{pn}, we estimate the errors in the measurements of A and B to be 0.09 fm and 0.03 fm, respectively. Table (7-2) shows the results obtained for A and B in this work using the Arndt's prediction for ρ_{pp} and ρ_{pn}.

A fm	B fm
0.77 ± 0.09	-1.0 ± 0.03

Table (7-2) - Values of A and B obtained from p-d data.

Now, by considering the definition of A and B and using the Arndt prediction at 800 MeV (Arndt 80) for γ_{1p} = 0.82 fm and γ_{2p} = -0.4 fm (γ_{1p} and γ_{2p} are related to the spin-orbit amplitude for p-p by Eq. (2-17), one obtains the following values for γ_{1n} and γ_{2n} [related to the spin-orbit amplitude of p-n by Eq. (2-17)]

$$\gamma_{1n} = 0.72 \pm 0.09 \text{ fm}$$

$$\gamma_{2n} = -1.6 \pm 0.03 \text{ fm} \quad .$$

In comparison with the Arndt prediction for γ_{1n} and γ_{2n} at 800 MeV, our value for γ_{1n},γ_{1n} = 0.72 fm, is in good agreement with his prediction (γ_{1n} = 0.6 fm). However, there is a considerable discrepancy between our value for γ_{2n},γ_{2n} = -1.6 ± 0.03 fm, and the Arndt prediction, γ_{2n} = -0.38 fm at 800 MeV.

Figure (7-1) shows the fit to the analyzing power obtained by fixing b_p = 9.3 $(\text{GeV/c})^{-2}$, b_n = 10.5 $(\text{GeV/c})^{-2}$, σ_p = 4.73 $(\text{fm})^2$, σ_n = 3.79 $(\text{fm})^2$, ρ_p = 0.02, ρ_n = -0.3 and using the values for A and B presented in Table (7-2). We have also compared the data with the prediction of the theory of p-d elastic scattering outlined in Chapter II (Alberi 79) using as an input the Arndt phase shifts (Arndt 80) prediction for the nucleon-nucleon amplitudes at 800 MeV (solid curve). In Fig. (7-2) we show the comparison between our data for the elastic p-d differential cross section at 800 MeV with the prediction of the theory developed by Alberi (Alberi 79) using the Arndt phase

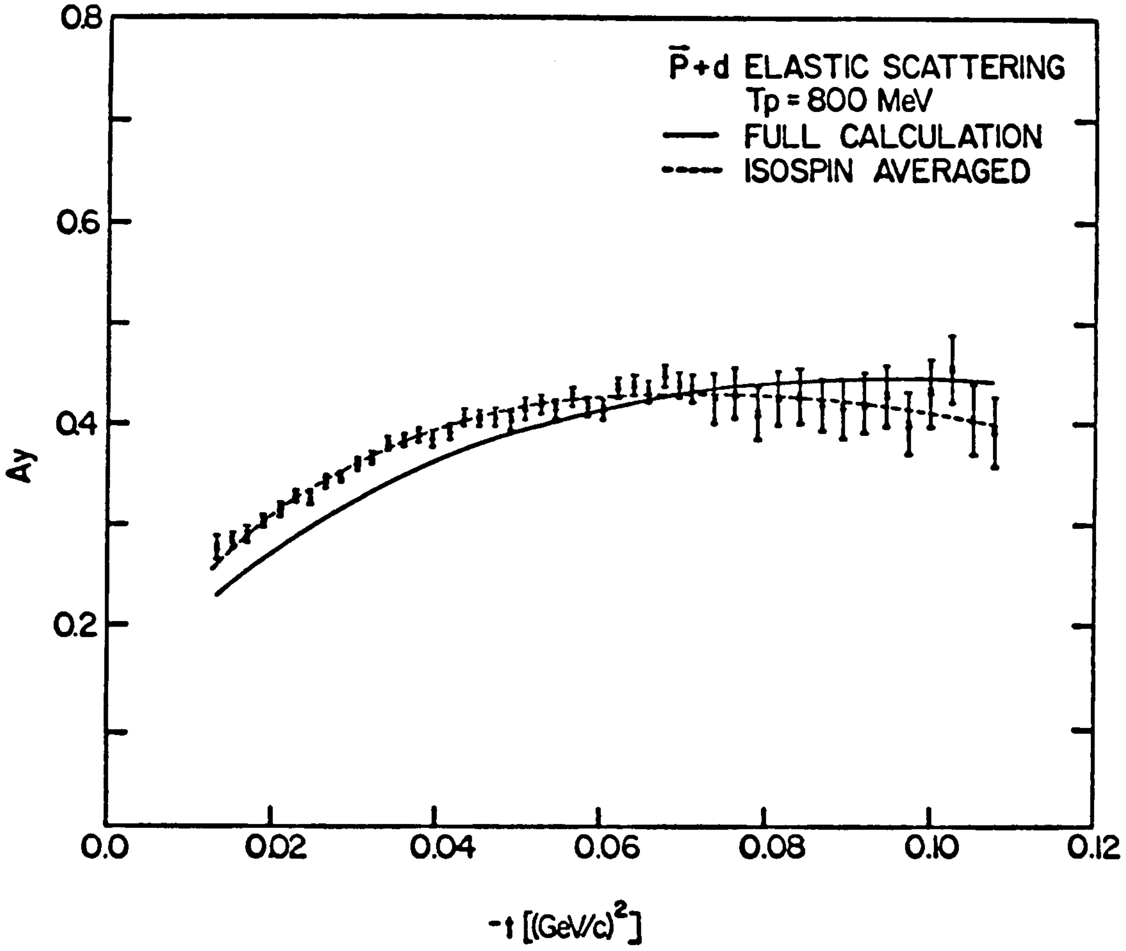

Fig. (7-1): The analyzing power for elastic $\vec{p}$-d scattering at 800 MeV. The dashed line through the data represents the isospin averaged fit to the data by fixing $b_p = 9.3\ (\mathrm{GeV}/c)^{-2}$, $b_n = 10.5\ (\mathrm{GeV}/c)^{-2}$, $\sigma_p = 4.73\ (\mathrm{fm})^2$, $\sigma_n = 3.79\ (\mathrm{fm})^2$, $\rho_{pp} = 0.02$, $\rho_{pn} = -0.3$, $A = 0.77$ fm, and $B = -1.0$ fm. The solid curve is Alberi *et al.* prediction using as an input the Arndt phase shifts prediction for nucleon-nucleon amplitudes at 800 MeV.

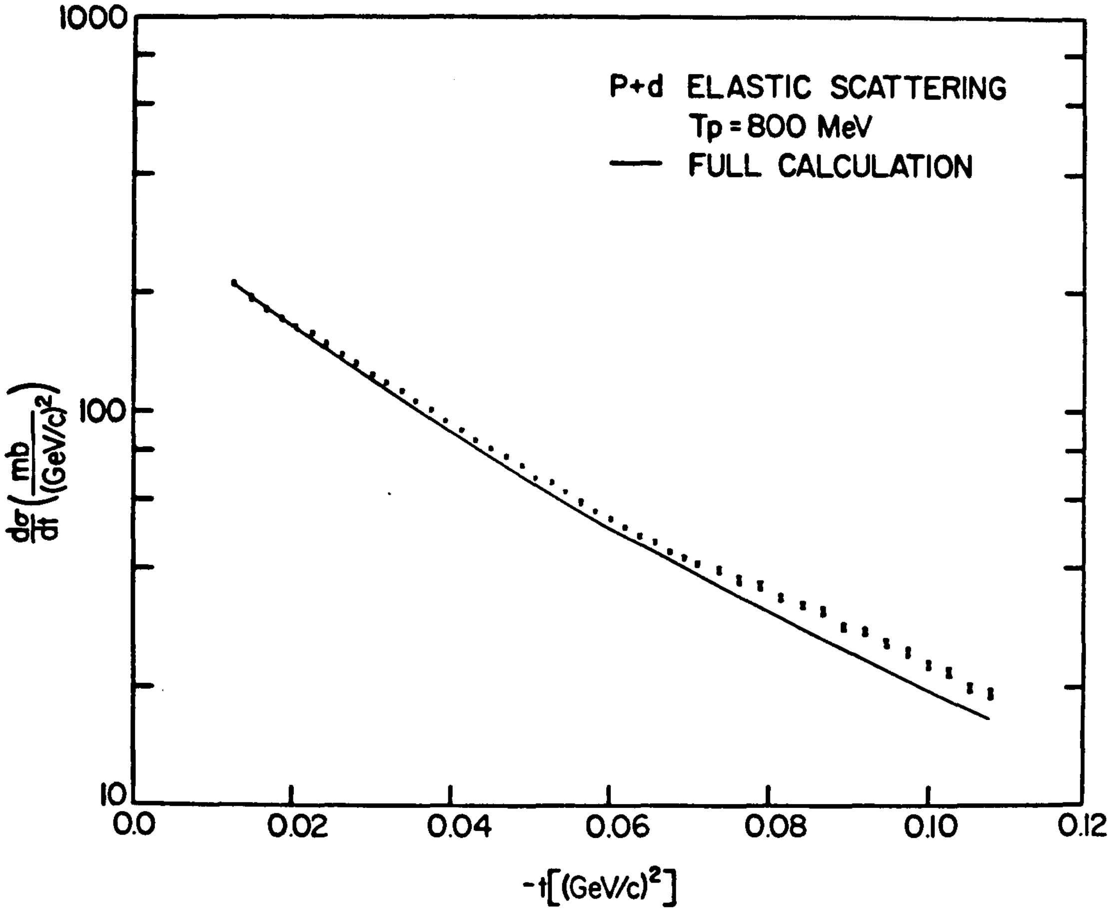

Fig. (7-2): The differential cross section for elastic p-d scattering at 800 MeV. The solid line is Alberi et al. prediction using as input the Arndt phase shifts prediction for nucleon-nucleon amplitudes at 800 MeV.

shifts (Arndt 80) prediction for the nucleon-nucleon amplitudes at 800 MeV.

B. Discussion

Absolute differential cross section and analyzing power measurements for elastic proton-deuteron scattering at 800 MeV with an instrumental uncertainty 3% have been presented as a part of this dissertation. These measurements have been done in the region of four momentum-transfer-squared $0.01<|t|<0.017$ $(GeV/c)^2$ which correspond to laboratory scattering angles ranging between 3.97° and 13.1°, respectively. For the reasons discussed in Chapter IV, we believe data are quite accurate.

Recent work on the theory of hadron-deuteron scattering at intermediate energy (Alberi 79) provide us with a precise tool for studying the dependence of the proton-deuteron scattering observables on the p-n amplitudes. This approach has been applied in the theoretical analysis of the data. In the framework of this theory a fit to the analyzing power was made using isospin averaged nucleon-nucleon amplitudes, in order to extract information on the real and imaginary parts of the proton-neutron spin-orbit amplitude.

Elastic proton-deuteron scattering turns out to be a very good tool for obtaining some information on the values of the p-n amplitudes at small angles. The deuteron is the simplest few body system with a neutron constituent. Good knowledge of the deuteron wave function (at least at large r) and its small binding energy (the scattering process can be described very well in terms of the free nucleon-nucleon amplitudes) allow an accurate extraction of the proton-neutron amplitudes.

APPENDIX A

OPTICAL THEOREM

The optical theorm for spinless particles has the form

$$\mathrm{Im}\, f(0) = \frac{k}{4\pi}\,\sigma_{\mathrm{ToT}} \quad , \tag{A-1}$$

where f(0) is the forward scattering amplitude, k is the relative momentum and σ_{ToT} is the total (transmission) cross section. For particles with spin, f is replaced by matrix M in spin space defined in Eq. (1-2) and the generalization of Eq. (A-1) is

$$\mathrm{Im}\, \mathrm{Tr}\big(\rho M(0)\big) = \frac{k}{4\pi}\,\sigma_{\mathrm{Tot}} \quad , \tag{A-2}$$

where ρ is density matrix. To understand the form of Eq. (A-2), note that Eq. (A-1) applies equally to any single spin channel; that is, one may replace f(0) by the expectation value of M(0) in any pure spin state. For an incoherent mixture of pure spin states the expectation value of M(0) can be replaced by $\mathrm{Tr}\big(\rho M(0)\big)$, and thus the general form of Eq. (A-2) results.

Now, let the quantization axis (z-axis) be along the direction of motion of incident beam The c.m.f unit vectors appearing in M are

$$\hat{n} = (0,1,0),\ \hat{m} = (\cos\theta/2,\ 0,\ -\sin\theta/2),\ \hat{\ell} = (-\sin\theta/2,\ 0,\ \cos\theta/2) \quad .$$

The matrix M at the forward direction has the form

$$M(0) = \alpha(0) + \beta(0)\sigma_{1y}\sigma_{2y} + \delta(0)\sigma_{1x}\sigma_{2x} + \varepsilon(0)\sigma_{1z}\sigma_{2z} \quad . \qquad \text{(A-3)}$$

Suppose nucleons 1 and 2 initially have independent polarizations $\vec{P}_1$ and $\vec{P}_2$. Thus

$$\rho = (1 + \vec{P}_1 \cdot \vec{\sigma}_1)(1 + \vec{P}_2 \cdot \vec{\sigma}_2) \quad .$$

After substitution for M(0) and ρ in Eq. (A-2), for the case $\vec{P}_1$ and $\vec{P}_2$ parallel, transverse to the beem, one obtains

$$\mathrm{Im}[\alpha(0) + \beta(0)P_1P_2] = \frac{k}{4\pi}\sigma_{ToT} \qquad [\text{Remember } \beta(0) = \delta(0)] \ ,$$

and, for the case of $\vec{P}_1$ and $\vec{P}_2$ parallel, along the beam (z-axis)

$$\mathrm{Im}[\alpha(0) + \varepsilon(0)P_1P_2] = \frac{k}{4\pi}\sigma_{ToT} \quad .$$

In the case of unpolarized beam or target ($\vec{P}_1$ or $\vec{P}_2 = 0$), generalized optical theorem has the simple form of:

$$\mathrm{Im}\alpha(0) = \frac{k}{4\pi}\sigma_{ToT}$$

APPENDIX B

PROTON-PROTON SCATTERING MATRIX ELEMENTS IN TERMS OF PHASE SHIFTS

Let the quantization axis (z-axis) be along the direction of motion of incident beam. The c.m.f unit vectors appearing in M are

$$\hat{n} = (0,1,0),\ \hat{m} = (\cos\theta/2,\ 0,\ -\sin\theta/2),\ \hat{\ell} = (\sin\theta/2,\ 0,\ \cos\theta/2)\ . \quad \text{(B-1)}$$

By operating M given by Eq. (1-2) on the spin state of two nucleons, we have

$$M\chi_s = (\alpha - \beta - \varepsilon - \delta)\chi_s\ ,$$

$$M\chi_1 = (\alpha + \delta\sin^2\theta/2 + \varepsilon\cos^2\theta/2)\chi_1 + \sqrt{2}\,(-\gamma + \frac{1}{2}\varepsilon\sin\theta - \frac{1}{2}\delta\sin\theta)\chi_o$$

$$+ \frac{1}{2}(-\beta + \delta\cos^2\theta/2 + \varepsilon\sin^2\theta/2)\chi_{-1}\ ,$$

$$M\chi_o = \sqrt{2}\,(\gamma + \frac{1}{2}\varepsilon\sin\theta - \frac{1}{2}\delta\sin\theta)\chi_1 + (\alpha + \beta - \varepsilon\cos\theta + \delta\cos\theta)\chi_o$$

$$+ \sqrt{2}\,(-\gamma - \frac{1}{2}\varepsilon\sin\theta + \frac{1}{2}\delta\sin\theta)\chi_{-1}\ ,$$

$$M\chi_{-1} = (-\beta + \delta \cos^2\theta/2 + \varepsilon \sin^2\theta/2)\chi_1 + \sqrt{2}\,(\gamma - \frac{1}{2}\,\varepsilon \sin\theta + \frac{1}{2}\,\delta \sin\theta)\chi_0$$

$$+ (\alpha + \varepsilon \cos^2\theta/2 + \delta \sin^2\theta/2)\chi_{-1} \quad , \qquad \text{(B-2)}$$

where

$$\chi_s = \left(\frac{1}{2}\right)^{-3/2} \left\{ \begin{pmatrix} 1 \\ 0 \end{pmatrix}_1 \begin{pmatrix} 0 \\ 1 \end{pmatrix}_2 - \begin{pmatrix} 0 \\ 1 \end{pmatrix}_1 \begin{pmatrix} 1 \\ 0 \end{pmatrix}_2 \right\}$$

represents the singlet-spin state, and

$$\chi_1 = \begin{pmatrix} 1 \\ 0 \end{pmatrix}_1 \begin{pmatrix} 1 \\ 0 \end{pmatrix}_2 \quad ,$$

$$\chi_0 = \left(\frac{1}{2}\right)^{-3/2} \left\{ \begin{pmatrix} 1 \\ 0 \end{pmatrix}_1 \begin{pmatrix} 0 \\ 1 \end{pmatrix}_2 + \begin{pmatrix} 0 \\ 1 \end{pmatrix}_1 \begin{pmatrix} 1 \\ 0 \end{pmatrix}_2 \right\} \quad ,$$

$$\chi_{-1} = \begin{pmatrix} 0 \\ 1 \end{pmatrix}_1 \begin{pmatrix} 0 \\ 1 \end{pmatrix}_2$$

are the spin wave functions for the triplet-spin state. The subscripts 1 and 2 refer to the two nucleons 1 and 2. Eqs. (B-2) imply

$$M_{ss} = \alpha - \beta - \varepsilon - \delta \; ,$$

$$M_{11} = M_{-1-1} = \alpha + \delta \sin^2\theta/2 + \varepsilon \cos^2\theta/2 \; ,$$

$$M_{10} = -M_{-10} = \sqrt{2}\,\gamma - \frac{1}{\sqrt{2}}\,\delta\,\sin\theta + \frac{1}{\sqrt{2}}\,\varepsilon\,\sin\theta\ ,$$

$$M_{1-1} = M_{-11} = -\beta + \delta\,\cos^2\theta/2 + \varepsilon\,\sin^2\theta/2\ ,$$

$$M_{01} = -M_{0-1} = -\sqrt{2}\,\gamma - \frac{\delta}{\sqrt{2}}\,\sin\theta + \frac{\varepsilon}{\sqrt{2}}\,\sin\theta\ ,$$

$$M_{oo} = \alpha + \beta + \delta\cos\theta - \varepsilon\cos\theta\ . \qquad \text{(B-3)}$$

The inverse relations of Eqs. (B-3) are

$$\alpha = \frac{1}{2}\left(2M_{11} + M_{00} + M_{ss}\right)\ ,$$

$$\beta = \frac{1}{4}\left(-2M_{1-1} + M_{00} - M_{ss}\right)\ ,$$

$$\gamma = \frac{\sqrt{2}}{4}\left(M_{10} - M_{01}\right)\ ,$$

$$\delta = \frac{1}{4}\left[\left(M_{11} + M_{1-1} - M_{ss}\right) - \frac{1}{\cos\theta}\left(M_{11} - M_{1-1} - M_{00}\right)\right]\ ,$$

$$\varepsilon = \frac{1}{4}\left[\left(M_{11} + M_{1-1} - M_{ss}\right) + \frac{1}{\cos\theta}\left(M_{11} - M_{1-1} - M_{oo}\right)\right]\ . \qquad \text{(B-4)}$$

Stapp et al. (Stapp 57) have calculated the matrix elements M_{ij} for proton-proton scattering in terms of phase shifts. They have shown that; for example

$$M_{10} = \frac{2}{iK} \sum_{\text{odd } \ell} P_\ell^1(\theta) \Big\{ \frac{\sqrt{2}}{4} a_{\ell,\ell+1} - \frac{\sqrt{2}}{4} a_{\ell,\ell-1}$$

$$+ \frac{\sqrt{2}}{4} \left(\frac{\ell+2}{\ell+1}\right)^{1/2} a^{\ell+1} - \frac{\sqrt{2}}{4} \left(\frac{\ell-1}{\ell}\right)^{1/2} a^{\ell-1} \Big\} \quad ,$$

$$M_{01} = \frac{2}{ik} \sum_{\text{odd } \ell} P_\ell^1(\theta) \Big\{ - \frac{\sqrt{2}}{4} \left(\frac{\ell + 2}{\ell + 1}\right) a_{\ell,\ell+1} + \frac{\sqrt{2}}{4} \left(\frac{2\ell + 1}{\ell(\ell + 1)}\right) a_{\ell,\ell}$$

$$+ \frac{\sqrt{2}}{4} \left(\frac{\ell - 1}{\ell}\right) a_{\ell,\ell-1} + \frac{\sqrt{2}}{4} \left(\frac{\ell + 2}{\ell + 1}\right)^{1/2} a^{\ell+1} - \frac{\sqrt{2}}{4} \left(\frac{\ell - 1}{\ell}\right)^{1/2} a^{\ell-1} \Big\} \quad ,$$

$$M_{1-1} = \frac{2}{ik} \sum_{\text{odd } \ell} P_\ell^2(\theta) \Big\{ \left(\frac{1}{4(\ell + 1)}\right) a_{\ell,\ell+1} - \left(\frac{2\ell + 1}{4\ell(\ell + 1)}\right) a_{\ell,\ell} + \left(\frac{1}{4\ell}\right) a_{\ell,\ell-1}$$

$$- \frac{1}{4} \left[(\ell + 1)(\ell + 2)\right]^{-1/2} a^{\ell+1} - \frac{1}{4} \left[(\ell - 1)\ell\right]^{-1/2} a^{\ell-1} \Big\} \quad .\text{(B-5)}$$

where $P_\ell^m(\theta)$ is the associated Legendre polynomial $a_{\ell j}$ and a^ℓ are the scattering amplitude and expressed in terms of the bar phase shifts of Stapp et al. (Stapp 57).

From Eqs. (B-4) at $\theta = 0$ we may write

$$\beta(0) = \frac{1}{4}\left(-2M_{1-1} + M_{00} - M_{ss}\right) \quad ,$$

$$\delta(0) = \frac{1}{4}\left(2M_{1-1} + M_{00} - M_{ss}\right) \quad .$$

However, from the definition of the associated Legendre polynomial

$$P_\ell^m(1) = 0 \quad .$$

Therefore at $\theta = 0$ we have

$$M_{1-1} = 0$$

which implies

$$\beta(0) = \delta(0) \quad .$$

Now, after substututing for M_{10} and M_{01} in the expression given for γ in Eqs. (B-3), one obtains

$$\gamma = \frac{1}{4ik} \sum_{\text{odd } \ell} P_\ell^1(\theta) \left\{\frac{2\ell + 3}{\ell + 1} a_{\ell,\ell + 1} - \frac{2\ell \quad 1}{\ell} a_{\ell,\ell-1} + \frac{2\ell + 1}{\ell(\ell + 1)} a_{\ell\ell}\right\}$$

or

$$\gamma = \sum_{\ell \text{ odd}} \gamma_\ell P_\ell^1(\theta) \quad . \qquad \text{(B-6)}$$

Here, γ_ℓ is a coefficient which depends on the energy. Near forward direction we may write:

$$P_\ell^1(\theta) = \frac{1}{2}\,\ell(\ell + 1)\sin\theta\,\left[1 - \frac{1}{8}\,(\ell + 2)(\ell - 1)\theta^2 + \text{----}\right] \quad .$$

After substitution of $P_\ell^1(\theta)$ in Eq. (B-6) one gets a simple expression for the hadronic spin-orbit amplitude at small angles.

$$\gamma = \gamma_0 \sin\theta \quad .$$

APPENDIX C

ENERRGY LOSS CORRECTIONS

In this section we will discuss in more detail the method used to calculate the energy of a recoil particle at the center of the interaction region from the energy deposited in the active region of the detectors. Let E be the energy of the particle at the center of the interaction region. It will lose energy in passing through the gas target; and it will reach the detector telescope with energy E_i. The gas thickness which the recoil particle passed through is equal to the difference in the ranges for particles with respective energies E and E_i in the target gas. The range of a charged particle in matter is given by the following integral:

$$R = \int_{o}^{E} \left(\frac{dE}{d\xi}\right)^{-1} dE \qquad \text{(C-1)}$$

where $dE/d\xi$ is the stopping power ($\mathrm{MeV/g/cm^2}$). Thus the thickness, Δ, of the target gas is:

$$\Delta = \int_{E_i}^{E} \left(\frac{dE}{d\xi}\right)^{-1} dE \quad .$$

Over the energy range of interest we have to a good approximation:

$$\left|\frac{dE}{d\xi}(E)\right| = AE^{-B} \qquad \text{(C-2)}$$

where A,B are determined for the recoil particle of interest in the target gas.

Therefore:

$$\Delta = \int_{E_i}^{E} \frac{1}{A} E^B \, dE$$

$$= \frac{1}{A(B + 1)} \left[E^{B+1} - E_i^{B+1}\right]$$

and solving for E gives:

$$E = \left[E_i^{B+1} + \Delta A(B + 1)\right]^{1/B+1} \quad . \qquad \text{(C-3)}$$

Now, Δ is equal to the density of the gas, ρ, in g/cm^3 multiplied by the path length, L, of the recoil particle from the interaction region to the detector telescope:

$$L = \frac{H}{\sin\theta} \qquad \text{(C-4)}$$

where H is defined in Fig. (3-2) and θ is the laboratory scattering angle of the recoil particle. Now θ is a function of the recoil particles energy [Eq. (4-9)]. Since E is approximately equal to E_i, $\sin\theta$ is given to a good approximation by:

$$\sin\theta \approx \left[1 - \frac{(M + E_o)^2 E_i}{2MP_o^2 \, (1 + E_i/2M)}\right]^{1/2} \qquad \text{(C-5)}$$

where M, E_o, P_o are defined in Chapter IV. Substituting Eqs. (C-5) and (C-4) into Eq. (C-3) gives:

$$E = \left\{E_i^{B+1} + \rho HA(B + 1)/\left[1- \frac{(M + E_o)^2 E_i}{2MP_o^2(1 + E_i/2M)}\right]^{1/2}\right\}^{1/(B+1)} \quad . \qquad \text{(C-6)}$$

In the next step we will calculate the energy incident on the detector telescope, E_i, from the energy deposited in the active volume of the detectors for the ΔE - E setup. When the particle reaches the detector telescope it will pass through a dead layer of thickness D_1 on the front of the ΔE detector; and it then enters the active region of the ΔE detector with an energy E'_i. In passing through the active volume of thickness t_a the energy of particle will be reduced and when it reaches the dead layer on the back of the ΔE detector it will have an energy E''_i. The particle will then pass through the dead layers D_2 and D_3 and have an energy E'''_i when it reaches the active volume of the E detector. [See Fig. (C-1)]. The energy E'''_i will completely absorbed in the E detector. The total energy, E_d, deposited in the active volumes will be given by:

$$E_d = (E'_i - E''_i) + E'''_i \quad . \qquad \text{(C-7)}$$

The energy incident on the telescope extrapolated back from the energy deposited in the detector telescope is given by:

$$E_i = E_d + \left|\frac{dE}{d\xi}(E_i)\right|D_1 + \left|\frac{dE}{d\xi}(E''_i)\right|(D_2 + D_3) \quad . \qquad \text{(C-8)}$$

With good accuracy the second term can be approximated as:

$$\left|\frac{dE}{d\xi}(E_i)\right|D_1 \approx \left|\frac{dE}{d\xi}(E_d)\right|D_1 = D_1 A' E_d^{-B'} \qquad \text{(C-9)}$$

where A' and B' are determined for the recoil particle of interest on dead layer material. To calculate the last term in (C-8) we need a relation between E''_i and E_d. The thickness of the ΔE detector, t_a, is equal to the difference between the range of recoil particles at energies E'_i and E''_i in silicon:

$$t_a = \int_{E''_i}^{E'} \frac{1}{dE/d\xi}\, dE$$

$$t_a = \int_{E''_i}^{E'} \frac{1}{A'} E^{B'}\, dE$$

or

$$t_a = \frac{1}{A'(B'+1)} \left[E_i'^{B'+1} - E_i''^{B'+1}\right]$$

to good accuracy we may use the approximation $E'_i \approx E_d$; and thus we may write:

$$E''_i = \left[E_d^{B'+1} - t_a A'(B'+1)\right]^{1/B'+1}$$

which then gives:

$$\frac{dE}{d\xi}(E''_i) = A'\left[E_d^{B'+1} - t_a A'(B'+1)\right]^{-B'/B'+1} \qquad \text{(C-10)}$$

substitution of Eqs. (C-9) and (C-10) into Eq. (C-8) gives the incident energy, E_i, in terms of the energy, E_d, deposited in the detector telescope:

$$E_i = E_d + D_1 A' E_d^{-B'} + A'(D_2 + D_3)\left[E_d^{(B'+1)} - t_a A'(B'+1)\right]^{-B'/B'+1} \quad .\text{(C-11)}$$

By substitution of Eq. (C-11) into Eq. (C-6) we can relate the energy of the recoil particle at the center of interaction, E, to the experimentally measured energy, E_d, deposited in the active volume of the detector telescope.

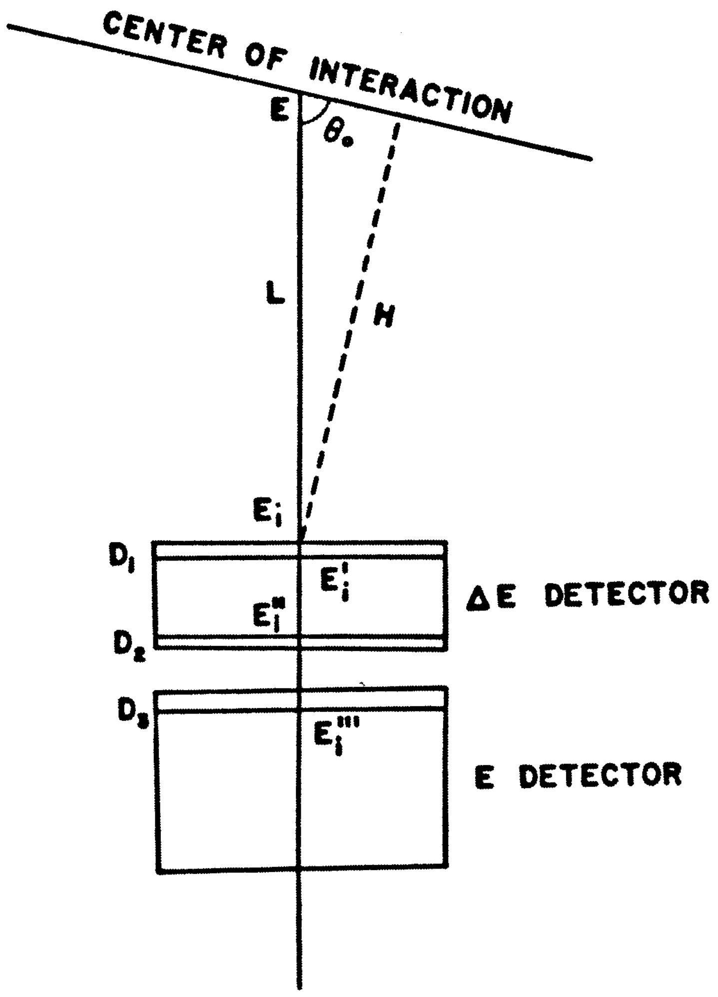

Fig. (C-1): Energy Loss Consideration Schemes.

Energy Deposited in Detector Telescope (MeV)	Energy Incident on Detector Telescope (MeV)	Energy at Center of Interaction (MeV)
3.0	3.008	3.31
4.0	4.006	4.25
5.0	5.004	5.21
6.0	6.004	6.18
7.0	7.003	7.16
8.0	8.003	8.14
9.0	9.003	9.13
10.0	10.003	10.12
11.0	11.002	11.11
12.0	12.002	12.10
13.0	13.002	13.10
14.0	14.002	14.09
15.0	15.002	15.08

Table (C-1) - Energy scale for 500 mm Hg of hydrogen in $\Delta E,E$ setup.

Energy Deposited in Detector Telescope (MeV)	Energy Incident on Detector Telescope (MeV)	Energy at Center of Interaction (MeV)
0.8	0.803	0.86
1.0	1.002	1.05
1.2	1.202	1.24
1.4	1.402	1.44
1.6	1.602	1.64
1.8	1.802	1.83
2.0	2.002	2.03
2.2	2.202	2.23
2.4	2.402	2.43
2.6	2.601	2.63
2.8	2.801	2.82
3.0	3.001	3.02
3.2	3.201	3.22

Table (C-2) - Energy scale for 40 mm Hg of hydrogen in time of flight setup.

Energy Deposited in Detector Telescope (MeV)	Energy Incident on Detector Telescope (MeV)	Energy at Center of Interaction (MeV)
5.0	5.010	5.22
6.0	6.007	6.19
7.0	7.006	7.16
8.0	8.005	8.15
9.0	9.005	9.14
10.0	10.004	10.13
11.0	11.004	11.12
12.0	12.004	12.11
13.0	13.003	13.10
14.0	14.003	14.10
15.0	15.003	15.09
16.0	16.003	16.09
17.0	17.003	17.08
18.0	18.003	18.08
19.0	19.003	19.07
20.0	20.002	20.07

Table (C-3) - Energy scale for 300 mm Hg of deuterium in $\Delta E,E$ setup.

ACKNOWLEDGMENTS

I would like to extend my sincerest appreciation to my research advisors, Professors George Igo and Charles A. Whitten, Jr., for their guidance, encouragement and support throughout all phases of this work. I benefited immensely from the friendship and help of Dr. John McClelland during this work. Special thanks are due to my friends Drs. Gianni Pauletta and Magdy Gazzaly for many helpful discussions. I would like to acknowledge Dr. Mark Bleszynski for his work on the theoretical codes used to interpret p-d data. Also, I would like to thank Dr. Nobi Tanaka for his help and concern during my stay at LAMPF. My appreciation and gratitude to Mrs. Bea Blonsky and Ms. Barbara Yamadera for their kind assistance during my graduate studies at UCLA. Thanks also go to Mrs. Lilly Cordova for preparing the final manuscript. Finally, I wish to thank the staffs of both UCLA, Physics Department, and LAMPF for providing assistance to me over the years.

REFERENCES

Aebischer 76	D. Aebischer et al., Phys. Rev. D13 2478 (1976).
Aebischer 77	D. Aebischer et al., Nucl. Phys. A276 445 (1977).
Alberi 79	G. Alberi et al., Phys. Rev. D20 2437 (1979).
Alberi 80	G. Alberi et al., to be published.
Arndt 74	R. A. Arndt et al., Phys. Rev. C9 555 (1974).
Arndt 80	R. A. Arndt et al., private communication, 1980.
Auer 77	I. P. Auer et al., Phys. Lett. 67B 113 (1977); I. P. Auer et al., Phys. Lett. 70B 475 (1977).
Auer 78	I. P. Auer et al., Phys. Lett 41 354 (1978).
Barrett 75	R. J. Barrett et al., Nucl. Inst. 129 441 (1975).
Benary 70	O. Benary et al., Lawrence Radiation Laboratory Report No. UCRL-2000NN, 1970 (unpublished).
Bethe 58	H. Bethe, Ann. Phys. (N.Y.) 3 190 (1958).
Bevington 69	P. R. Bevington, Data Reduction and Error Analysis for the Physical Sciences, McGraw-Hill, Inc. 1969.
Bleszynski 80	M. Bleszynski, private communication 1980.
Bourrely 74	C. Bourrely et al., Nucl. Phys. B77 386 (1974).
Bystricky 75	J. Bystricky et al., Fourth Int. Symp. on Polarization Phenomena in Nuclear reactions, August, 1975, Zürich, Switzerland.
Clark 79	D. A. Clark, IEEE Trans. NS26 3291 (1979).
Coward 68	D. H. Coward, Phys. Rev. Lett. 20 292 (1968).
Dutton 67	L.M.C. Dutton et al., Phys. Lett. 25B 245 (1967).
Dutton 68	L.M.C. Dutton et al., Phys. Lett. 26B 679 (1968).

Eisenbud 41	L. Eisenbud *et al.*, Proc. Nat. Acad. Sci. *27* 281 (1941).
Gasiorowicz 66	S. Gasiorowicz, *Elementary Particle Physics*, John Wiley & Sons, N.Y., (1966).
Goldberger 64	M. L. Goldberger and K. M. Watson, *Collision Theory*, John Wiley & Sons, N.Y., (1964).
Grein 78	W. Grein and P. Kroll, Nucl. Phys. *B132* 173 (1978).
Hagedorn 73	R. Hagedorn, *Relativistic Kinematics* W. A. Benjamin, Reading, 1973.
Hoshizaki 68	N. Hoshizaki, Progr. Theor. Phys. Suppl. *42* 107 (1968).
Hoshizaki 78	N. Hoshizaki, Progr. Theor, Phys. *60* 1796 (1978).
Hoshizaki 79	N. Hoshizaki, private communication (1979).
Janni 66	J. F. Janni, *Calculation of Energy Loss, Range, Path Lengths, Straggling, Multiple Scattering and Probability of Inelastic Nuclear Collisions for 0.1 to 1000 MeV Protons*, Air Force Weapons Laboratory Report No. AFWL-TR-65-150, 1966 (unpublished).
Locher 67	M. P. Locher *et al.*, Nucl. Phys. *B2* 626 (1967).
MacGregor 60	M. H. MacGregor *et al.*, Ann. Rev. Nucl. Sci. *10* 291 (1960).
MacGregor 69	M. H. MacGregor *et al.*, Phys. Rev. *182* 1714 (1969).
McNaughton 80	M. W. McNaughton, *LAMPF Beam Line Polarimeters*, Los Scientific Laboratory Report No. LA-8307-MS (1980).
Pauletta 80	G. Pauletta *et al.*, Fifth Int. Symp. on Polarization Phenomena in Nuclear Reactions, August 1980, Santa Fe, NM (U.S.A.).
Ohlsen 73	G. G. Ohlsen and P. W. Keaton, Nucl. Inst. *109* 41 (1973).
Orear 58	J. Orear, *Notes on Statistics for Physicists*, Lawrence Radiation Laboratory Report No. UCRL-8417 (1958).

Stapp 57	H. . Stapp *et al*., Phys. Rev. **105** 302 (1957).
Skyrme 67	D. J. Skyrme, Nucl. Inst. and Meth. **57** 61 (1967).
Varobyov 72	A. A. Varobyov *et al*., Phys. Lett. **41B** 639 (1972).
Whitten 75	C. A. Whitten, Jr., Nucl. Inst. and Meth. **128** 93 (1975).
Williamson 66	C. F. Williamson *et al*., *Commissariat de L'Energie Atomique* (France) Report No. CEA-R-3042, 1966 (unpublished).
Wolfenstein 52	L. Wolfenstein and J. Ashkin, Phys. Rev. **85** 947 (1952).
Wriekat 80	A. Wriekat *et al*., accepted for publication in Phys. Lett. (1980).

☆U.S. GOVERNMENT PRINTING OFFICE: 1981-0-777-022/8